

UNCLASSIFIED

AD 407 036

DEFENSE DOCUMENTATION CENTER

FOR

SCIENTIFIC AND TECHNICAL INFORMATION

CAMERON STATION, ALEXANDRIA, VIRGINIA



UNCLASSIFIED

NOTICE: When government or other drawings, specifications or other data are used for any purpose other than in connection with a definitely related government procurement operation, the U. S. Government thereby incurs no responsibility, nor any obligation whatsoever; and the fact that the Government may have formulated, furnished, or in any way supplied the said drawings, specifications, or other data is not to be regarded by implication or otherwise as in any manner licensing the holder or any other person or corporation, or conveying any rights or permission to manufacture, use or sell any patented invention that may in any way be related thereto.

63-41

NRL Report 5897

CATALOGED BY DDC 407036

AS AD No.

407036

# AN INVESTIGATION OF THE PHENOMENOLOGICAL CHARACTERISTICS OF $(p, \gamma)$ RESONANCES

R. O. Bondelid and J. W. Butler

Van de Graaff Branch  
Nucleonics Division

May 7, 1963

DDC  
RECEIVED  
JUN 21 1963  
ALSO V 50  
TISIA B



U. S. NAVAL RESEARCH LABORATORY  
Washington, D.C.

## CONTENTS

|   |     |
|---|-----|
| Abstract  | iii |
| Problem Status  | iii |
| Authorization   | iii |
| <br>  |     |
| INTRODUCTION  | 1   |
| <br>  |     |
| EXPERIMENTAL APPARATUS  | 2   |
| <br>  |     |
| TARGETS   | 3   |
| <br>  |     |
| RESULTS WITH THE $H_1^+$ BEAM   | 5   |
| Yield Curves  | 5   |
| Anomalies   | 6   |
| Resonance-Width Measurements with Old Targets   | 9   |
| <br>  |     |
| INTERPRETATION OF ANOMALIES WITH THE $H_1^+$ BEAM   | 10  |
| The Formal Yield Equation   | 10  |
| Determination of the Function $w$   | 11  |
| Qualitative Explanation of the Anomalies  | 14  |
| Integration of the Formal Yield Equation  | 17  |
| Comparison of the Integrated Yield Equation with<br>the E-Series Targets at the 992-keV Resonance | 19  |
| Comparison of the Integrated Yield Equation with Other Data                                       | 23  |
| Further Considerations  | 28  |
| <br>  |     |
| APPLICATION TO RESONANCE-ENERGY DETERMINATION<br>WITH THE $H_1^+$ BEAM                            | 29  |
| <br>  |     |
| RESULTS WITH THE $H_2^+$ BEAM   | 30  |
| Displacement  | 30  |
| Thin Targets  | 33  |
| Other Anomalies   | 34  |
| Inert Coatings  | 35  |
| $H_1^+$ and $H_1^0$ Beams from the $H_2^+$ Beam   | 38  |
| <br>  |     |
| INTERPRETATION OF ANOMALIES WITH THE $H_2^+$ BEAM   | 41  |
| Nature of the $H_2^+$ Molecule  | 41  |
| The Effect of Separation Velocity on the Energy Distribution                                      | 43  |
| Interpretation of the Gas-Cell Results  | 44  |
| Interpretation of the Yield Curves from the E-Series Targets                                      | 45  |
| Qualitative Explanation of the Anomalies  | 49  |

|  |    |
|--|----|
| APPLICATION TO RESONANCE-ENERGY DETERMINATION<br>WITH THE H <sub>2</sub> <sup>+</sup> BEAM | 50 |
| Thin Targets   | 51 |
| Thick Targets  | 51 |
| DISCUSSION   | 52 |
| Recapitulation   | 52 |
| Related Work   | 52 |
| Suggested Future Work  | 54 |
| ACKNOWLEDGMENTS  | 57 |
| REFERENCES   | 58 |

## ABSTRACT

The observation of some "anomalies" in the behavior of gamma-ray resonances induced by hydrogen molecular ion beams has led to an exhaustive investigation of these and other new anomalies, including some involving proton beams. Most of the observations have been made with respect to the 992-keV resonance in the  $\text{Al}^{27}(\text{p}, \gamma)\text{Si}^{28}$  reaction, but the following have also been used: the 1317-keV resonance in the same reaction, the 1747-keV resonance in the  $\text{C}^{13}(\text{p}, \gamma)\text{N}^{14}$  reaction, the 1424-keV resonance in the  $\text{Ni}^{58}(\text{p}, \gamma)\text{Cu}^{59}$  reaction, and the 1843-keV resonance in the same reaction. A list of those anomalies observed with  $\text{H}_1^+$  beams includes (a) the failure of the peaks of thin-target resonance yield curves to be shifted from resonance energy by as much as half the target thickness in energy loss units, (b) the displacement of the midpoint of the rise of thick-target yield curves to bombarding energies below the resonance energy, (c) the "overshoot" of the yield curve for thick targets forming a hump above the thick-target plateau, (d) the obtaining of apparently different intrinsic resonance widths for the same resonance and from the same thick target at different times separated by a few weeks, and (e) the obtaining of significantly different thick-target yield-curve shapes from the same target in two different orientations with respect to the beam. A list of those anomalies observed with  $\text{H}_2^+$  beams includes (1) a rather pronounced asymmetry in the shape of the thick-target yield curve, (2) the apparent displacement of the midpoint of the rise of the thick-target yield curve to an energy value 0.05 percent below the resonance energy, (3) the overshoot of the yield for thick-target yield curves, causing a hump, (4) the failure of a plateau to appear for normally thick targets (10-20 keV), but instead a slow rise in the yield curve following the dip after the hump, (5) the failure of thin-target yield curves to have their peaks displaced from resonance energy by an energy value amounting to as much as half the target thickness, (6) the elimination of (1) and (2) by a thin coating of copper over the aluminum target, (7) the apparently different thicknesses of the same copper coating to  $\text{H}_1^+$  and  $\text{H}_2^+$  beams, (8) the extra "straggling" of  $\text{H}_2^+$  beams in the copper coatings as compared with  $\text{H}_1^+$  beams, (9) the rather large beam-energy broadening, or straggling effect, of a minute amount of gas used as a stripper of the  $\text{H}_2^+$  molecules, (10) the extra broadening of the  $\text{H}_1^+$  stripped component compared with the  $\text{H}_1^+$  stripped component, and (11) the broadening in both directions with respect to the energy (i.e., including energy gains as well as losses), the broadening for thick targets being just the right amount more in one direction to place the midpoint of the rise of the yield curve just at the resonance energy and to make the yield curve symmetric. The lists for the two different beams appear to have several anomalies in common, but actually the apparently similar anomalies are basically different because they arise for basically different reasons. The anomalies for  $\text{H}_1^+$  beams are all satisfactorily explained on the basis of fluctuations in energy loss of the bombarding protons as they penetrate the target. Detailed numerical integrations of the formal yield equation have been made, and in most cases very good fits have been made with the experimental data. The energy-loss theory used to compute the energy-loss fluctuations has been mainly the theory developed by Symon. For the anomalies observed with the use of  $\text{H}_2^+$  beams, the theory is more complicated because of the larger number of parameters involved: (a) the initial distribution of vibrational levels of the  $\text{H}_2^+$  molecules, (b) the initial distribution of internuclear separation distances (and hence internal

velocities), (c) the initial distribution of molecular axis orientation with respect to the bombarding-beam direction, and (d) the variety of modes of excitation and disintegration available for the  $H_2^+$  molecule as it enters the target. In addition to these parameters the  $H_2^+$  beams have all those available for  $H_1^+$  beams. In general, the  $H_2^+$  beam anomalies are satisfactorily explained by calculations of the change in energy of the two components resulting from the breakup of the  $H_2^+$  molecule. One component, be it  $H_1^+$  or  $H_1^0$ , gains energy in the laboratory system of coordinates if its disintegration velocity has a component parallel to the beam direction. The other component loses a corresponding amount of energy. Detailed numerical integrations have been performed taking the different experiments in a certain indicated order so that the information gained from the first ones taken was used to delimit the variables for those taken subsequently. In this way, reasonable agreement was obtained between the computed curves and the experimental data. The information gained from this investigation is applied to energy calibrations using both  $H_1^+$  and  $H_2^+$  beams. Precise best values are given for the following narrow  $(p, \gamma)$  resonances:  $Al^{27}(p, \gamma)Si^{28}$  reaction,  $991.91 \pm 0.30$  and  $1317.19 \pm 0.40$  keV;  $C^{13}(p, \gamma)N^{14}$  reaction,  $1747.06 \pm 0.53$  keV;  $Ni^{58}(p, \gamma)Cu^{59}$  reaction,  $1423.64 \pm 0.43$  and  $1843.45 \pm 0.56$  keV. The displacement of the midpoint of the rise of a thick-target  $H_1^+$  yield curve from the resonance energy  $E_r$  as a function of the resonance width  $\Gamma$  is discussed, and a typical curve of this relationship is shown. The overshoot or hump height for thick targets with  $H_1^+$  beams as a function of  $\Gamma$  is also discussed, and a curve is shown. Methods for making extremely uniform and clean thin targets have been developed and are discussed. A number of new questions were suggested by the results of these experiments, and experiments to answer these new questions are proposed to the reader for his consideration.

#### PROBLEM STATUS

This is a final report on one phase of the problem.

#### AUTHORIZATION

NRL Problem H01-04  
Project RR 002-06-41-5001

Manuscript received December 7, 1962.

## AN INVESTIGATION OF THE PHENOMENOLOGICAL CHARACTERISTICS OF $(p,\gamma)$ RESONANCES

### INTRODUCTION

Over the years there have evolved a number of rules governing the interpretation of experimental measurements of nuclear resonances in which gamma rays are emitted. Some of these rules concern the interrelationships among the resonance energy, resonance width, and shape of the gamma-ray yield curve. These rules have appeared eminently reasonable and have been verified experimentally within certain degrees of precision and for a range of values of bombarding beam-energy resolutions and resonance widths. However, during the past few years observations at the Naval Research Laboratory have cast some doubt upon the validity of some of these generally accepted concepts. Therefore an extensive program of testing these rules of interpretation was undertaken. The results of this program are the subject of this paper.

The rules which have come under question are the following. (1) The position of the experimentally observed peak of a resonance is shifted from resonance energy by half the target thickness, in terms of energy loss. (2) The resonance energy is located at the midpoint of the rise in the thick-target yield curve. (3) The thick-target yield curve has essentially the shape of the integral of the Breit-Wigner dispersion relation and the incident beam-energy distribution, and is therefore symmetric about the midpoint of the rise. These concepts have been considered to be valid for resonances narrow enough for the stopping power of the target material and the Coulomb penetrability of protons to be considered constant over the effective energy range of the resonance.

Fowler et al. (1), in 1948, presented an excellent comprehensive summary of the state of the art at that time. A more recent summary has been written by Gove (2) who discusses some deviations from the above rules.

These rules of interpretation concerning proton beams have been extended by many nuclear-reaction physicists to include hydrogen molecular ion beams with only one significant conceptual difference. The internal motion of the two protons with respect to the center-of-mass of the  $H_2^+$  molecule has been assumed to give a "Doppler" broadening in the effective energy inhomogeneity of the bombarding beam. It is not known by the authors who first gave this explanation for the broadening of the  $H_2^+$  beam  $(p,\gamma)$  resonances, but the idea has been common knowledge for at least 15 years. Within the knowledge of the authors, the only publication on the subject that appeared in the literature prior to 1957 (the year the abstract (3) of part of the present work was published) was an abstract in 1955 by Herring et al. (4) who called attention to this already widely accepted concept.

The generally held opinion concerning the hydrogen molecular ion (or  $H_2^+$ ) beam has been that one could use this beam in much the same way that one uses the proton (or  $H_1^+$ ) beam, the required energy for the hydrogen molecular ion being twice that necessary for the proton plus the energy carried by the electron.

One practical application of the hydrogen molecular ion beam is its use for energy calibration purposes. For electrostatic analyzers the same resonance whose energy is

---

Note: The present address of J. W. Butler is: Department of Physics and Astronomy, Michigan State University, East Lansing, Michigan.

precisely known can be observed by both the  $H_1^+$  and  $H_2^+$  beams, and the calibration point for the  $H_2^+$  beam is a factor of 2 higher (on the same energy scale) than that for the  $H_1^+$  beam (except for the energy carried by the electron and the correction due to the stray magnetic field). For magnetic analyzers, the  $H_2^+$  beam gives a calibration point a factor of 4 higher (on the energy scale) than the  $H_1^+$  beam. The Doppler broadening of the rise in the thick-target step does not appear to affect the accuracy to a large extent because the midpoint of the rise can still be determined quite precisely. Such measurements also have been used to test the energy linearity of electrostatic analyzers and the momentum linearity of magnetic analyzers.

Historically, the present series of investigations was initiated by the observation of an apparent nonlinearity in the NRL 2-meter-radius electrostatic beam-energy analyzer. The apparent energy of the 992-keV resonance in the  $Al^{27}(p,\gamma)$  reaction, determined from the midpoint of the rise in the thick-target yield curve with the hydrogen molecular ion beam, was lower than anticipated from the measurements with the proton beam, the amount of the "discrepancy" being about 0.05 percent. All of the usual corrections, the relativistic effect, internal and external magnetic fields, and energy carried by the electron, were made to the raw experimental data before the situation was labeled a discrepancy. Since this discrepancy was greater than the expected relative uncertainty, considerable effort was expended in an attempt to find its source.

As sometimes happens when an intensive effort is made to discover the nature of one "discrepancy," or "anomaly," other "anomalies" are found. The next anomaly noted as a result of very careful work was that the thick-target  $H_2^+$  beam yield curve is not symmetric about the midpoint of the rise. The bombarding energy interval required for the curve to rise to the midpoint is much greater than the interval required for the curve to rise from the midpoint to the apparent beginning of the thick-target plateau. More precise shape determinations revealed still another anomaly, the presence of a hump at the top of the rise.

When thin targets were used to make an independent check of the beam-energy analyzer calibration parameters in an effort to determine with certainty whether the original energy discrepancy with  $H_2^+$  beams on thick targets was due to some unconsidered factor affecting analyzer linearity, yet another anomaly was observed: the experimental peaks in the yield curves of the thin targets did not shift with target thickness according to rule (1).

Further work indicated the existence of all these anomalies with proton beams as well as hydrogen molecular ion beams. Thus as a result of the entire series of experiments, these and several other deviations from expected behavior were observed.

The present report consists of the experimental results and theoretical interpretation of the anomalies observed (a) with  $H_1^+$  beams and (b) with  $H_2^+$  beams. The discussion near the end of the report includes suggestions to the reader for future related experiments.

## EXPERIMENTAL APPARATUS

The positive-ion-beam acceleration was performed by the NRL 5-MV Van de Graaff Accelerator; the beam analysis was accomplished (in most of the measurements) by a high-resolution 2-meter-radius electrostatic beam-energy analyzer; and the proton-capture gamma rays were detected (in most of the measurements) by a 3-in.-diam x 3 in. NaI(Tl) scintillation crystal with associated electronic equipment.

The bombarding beam, after emerging from the accelerator, passed through a magnetic beam-momentum analyzer ( $40^\circ$  deflection) for preliminary energy selection and mass-component separation. Then the ion beam passed through the precision electrostatic

analyzer (90° deflection), whose input slit-defining jaws, or gnathos,\* were common with the output gnathos of the magnetic analyzer. The fine-energy stabilization of the accelerator was achieved by the use of electrical signals from these gnathos controlling the amount of corona current to the high-voltage terminal through the insulating gas of the accelerator. The entire system is described in detail in previous communications (5,6).

The NaI(Tl) crystal was placed at various orientations with respect to the target and bombarding beam during the various phases of the series of experiments, a typical position being at 90° with respect to the bombarding beam and in the horizontal plane containing the beam. A type-6363 multiplier phototube was optically coupled to the crystal, and its pulses were amplified and analyzed by a conventional linear amplifier and single-channel pulse-height analyzer. The analyzer window width was varied from time to time, but typical lower and upper settings were about 7 and 13 MeV.

The target holder formed a natural Faraday-type cup for beam-current collection, the current being integrated by a conventional Higinbotham and Rankowitz circuit (7). In some of the measurements, special techniques were employed; e.g., for the neutral bombarding beam ( $H_1^0$ ), secondary electrons were encouraged to leave the target surface by an attractive voltage on one of the elements near the target in the vacuum system.

During the course of the experiments, various specialized pieces of apparatus were used, and these will be described in connection with their use. A list of these devices includes a gas cell for stripping the  $H_2^+$  beam into its atomic components ( $H_1^+$  and  $H_1^0$ ), an associated permanent magnet mass-component and charge-component separator, and a phototube circuit for measuring the relative amounts of the  $H_1^0$  beam by means of the fluorescence properties of a quartz beam stopper.

## TARGETS

During the early phases of the program of experiments, the aluminum targets were generally evaporated onto metallic backings such as silver or tantalum. The asymmetries in the thin-target yield curves from these metallic-backed targets indicated non-uniformities in target thickness, and these asymmetries made it difficult to observe and interpret other effects. To diminish effects due to target nonuniformities, a target improvement program was undertaken with the following procedure being evolved.

The basic backing material was chosen to be microscope-slide glass (1 mm thick) cut into disks of diameter 15/32 inch. Care was taken to avoid scratching one of the sides of each glass disk during the cutting process. After cutting, the disks were thoroughly cleaned by being boiled in nitric acid for about 10 minutes and then in a combination of nitric and perchloric acids for about 30 minutes. The disks were then rinsed in more than ten different baths of distilled water (the first two rinsings involved boiling), each rinse involving a soaking period of several minutes. The disks were dried by being rinsed in ether.

The clean glass disks were inserted into holes in a multiple target-blank holder which was a simple copper plate with the holes drilled through it such that a narrow flange

\*The authors have observed that some physicists typically use the word "slit" to refer to both the space between two jaws and the jaws themselves. Clearly this usage is misleading and confusing, and furthermore it is incorrect. Therefore, the authors propose that the word "gnathos" (pronounced nãth'õs), the Greek word for "jaw" be used to refer to the slit-defining jaws. It is suggested that the word "gnathos" be used both for the singular and the plural. "Gnatho-" appears as the prefix to a number of words in unabridged dictionaries. The word "gnathos" also appears in "Composition of Scientific Words" by R. W. Brown, published by the author, 1954.

remained to prevent the disks from falling through the bottom. A layer of copper approximately thick enough to stop a 1-MeV proton was then deposited by evaporation in vacuo ( $\sim 10^{-6}$  torr).

The copper (spectroscopically pure) and the tungsten ribbon on which it rested were purged of impurities by being heated to the melting point of copper before the glass disks were placed in the vacuum system. A glow discharge in the evaporator provided final cleaning. A movable shield protected the clean blanks until a short time following the second melting of the copper. A final precaution was to admit a small amount of helium, following the evaporation, to speed cooling of the targets before air (and therefore oxygen) was admitted.

The purpose of the copper plating over the glass was threefold: to conduct heat away from the bombarded area of the aluminum target and thus prevent target damage due to high temperatures during positive-ion-beam bombardment, to conduct away electric charge and thus prevent the buildup of electric potential on the target, and to reduce the  $(p, \gamma)$  yield from the backing material. With the thinnest aluminum targets made without the copper coating, the electrical resistance measured from the center of the target to the edge increased from the order of ohms before bombardment to the order of megohms after a period of proton bombardment. There are several possible reasons for this effect, but it is not clear which reason is the most important; however, the targets with the copper-coated backings did not show the effect. In this series of experiments, it was vitally important that the target electric potential not become significantly different from ground because of the precision of the measurements and their interpretation. With respect to the third reason for the copper coating, the yield of gamma rays from 1-MeV protons impinging on glass is quite prolific, but for glass coated with at least 500 keV equivalent thickness of copper, the yield is almost negligible compared with that from a typical thin aluminum target.

The aluminum target material was usually deposited onto seven target blanks (with copper coatings) simultaneously. The blanks were held in position with the plane of each disk perpendicular to the line to the source of evaporating aluminum, the distance of each disk from the aluminum being a factor of  $\sqrt{2}$  different from that of its adjacent neighbors. The result of this arrangement was to give a series of seven targets, each varying in thickness from its neighbors by about a factor of 2, covering a total thickness range of 64. The most important series of aluminum targets had a thickness range from 17.8 keV to 0.31 keV for 1-MeV protons. These targets were labeled E-1 through E-7 in descending order of thickness.

Both the copper and the aluminum deposits were examined with a microscope using a 500-power magnification, but no evidence of irregularities in the surface smoothness was observed. However, after prolonged bombardment there were elevated circular "mesas" on the bombarded surface. These were apparently caused by the pressure of the imbedded hydrogen gas resulting from the bombardment. Since the area of the flat tops of the mesas was large compared to the area of the sloping sides, it is believed that this effect did not introduce significant target thickness nonuniformities.

The copper coatings were exposed to air between the copper depositing operation and the aluminum depositing operation; and the aluminum deposits were exposed to air before being inserted into the target holder. It appears certain therefore that a monolayer (or perhaps more) of copper oxide was formed on the copper coating prior to the deposit of the aluminum. It is therefore reasonable to assume that diffusion of the two metals across the interface boundary was insignificant.

Since the thinnest targets employed had an average thickness of about 40 atomic layers, the question naturally arises concerning target thickness nonuniformities due to statistical deviations in the number of atoms deposited. A number of arguments can be

advanced to demonstrate why actual deviations encountered would be small compared to what is expected based on statistically independent "columns" of deposited atoms. Two of these arguments are that ordering forces (crystal lattice forces) exist which cause the numbers of atoms in the different columns not to be statistically independent, and that even without such ordering forces, any significant peaks that were not many atoms wide would be subject to diffusion.

One attempt to understand the nature of some of the anomalies involved the coating of the aluminum targets with a thin film of evaporated copper. This thin final coating was accomplished in vacuo in a similar manner to the original copper coatings on the glass disks.

The entire series of experiments included observations of resonances in the  $\text{Ni}^{58}(\text{p},\gamma)$  reaction and a resonance in the  $\text{C}^{13}(\text{p},\gamma)$  reaction as well as resonances in the  $\text{Al}^{27}(\text{p},\gamma)$  reaction. Targets of  $\text{Ni}^{58}$  were prepared by electrodeposition onto silver backings. Thick targets of  $\text{C}^{13}$  were prepared by heating a molybdenum strip in an atmosphere of  $\text{CH}_3\text{I}$ , enriched to 40 percent  $\text{C}^{13}$ . Disks of the proper size were then obtained from the strips. Since the targets of  $\text{Ni}^{58}$  and  $\text{C}^{13}$  were thicker than a few keV, the effect of minor thickness nonuniformities was of little consequence.

The target holder is similar to one previously described (8), including a tube kept at liquid-nitrogen temperature enclosing the target. This tube is a trap for contaminating material and is of critical importance to the present series of experiments for the following reasons: (a) the possible displacement of the energy of a resonance by the presence of a film of inert or contaminating material on the target face, (b) the background which such a film of contaminating material might contribute to the total counting rate, especially for the thinnest targets, and (c) the straggling effect on the bombarding beam of such a film. This last effect is much more serious than we had previously supposed, especially in connection with thick-target width measurements of very narrow resonances.

## RESULTS WITH THE $\text{H}_1^+$ BEAM

Although the anomalies with the  $\text{H}_2^+$  beam were observed chronologically before those with the  $\text{H}_1^+$  beam, the results obtained with the  $\text{H}_1^+$  beam and the discussion of these results will be presented first for purposes of clarity.

During the course of the experiments several different values were used for the input and output slit widths of the electrostatic analyzer, resulting in several different beam-energy spreads. For most of the targets discussed below, the analyzer resolution was set to give a total beam-energy inhomogeneity of 0.04 percent, corresponding to a triangular distribution with a width of 0.02 percent at the half-height position of the energy distribution. For some targets, the beam-energy inhomogeneity was increased a factor of 2.5, and for others it was decreased a factor of 2.

### Yield Curves

The  $\text{H}_1^+$  beam yield curves for the 992-keV resonance and the family of targets E-1 through E-7 are shown in Fig. 1. The abscissa is in terms of the difference between the bombarding energy  $E_b$  and the resonance energy  $E_r$ . For purposes of comparison with theoretical yield curves, the ordinates have been normalized such that the integrals of the yield curves are numerically equal to the target thicknesses in units of  $10^{-5}$  cm. In the plotting and presentation of the data, the following procedures have been used. (1) The raw data were corrected for background, which was determined from the counting rate in the region about 10 keV below resonance. (2) The normalized statistical uncertainties are shown on each plotted normalized difference count point. (3) The curves tend

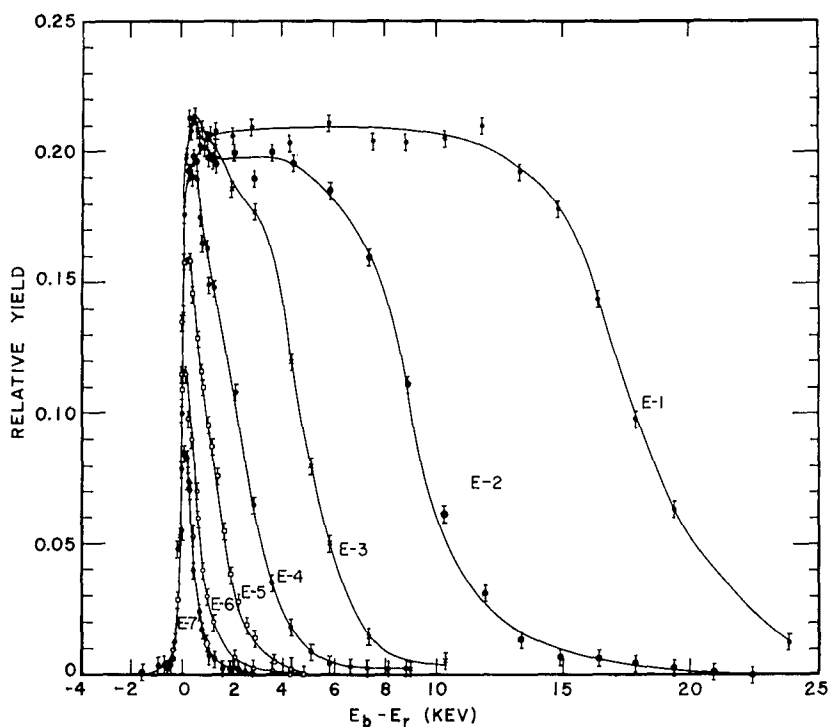


Fig. 1 - The experimental yield curves of the E-series aluminum targets near the resonance energy of 992 keV ( $H_1^+$  beam). The targets vary in thickness from 0.31 keV for E-7 to 17.8 keV for E-1, each different from its neighbor by about a factor of 2. Note the failure of the peaks to shift as much as half the target thickness, and note also the tendency for the yield to "over-shoot" for the thick targets.

to merge together at points on the low-energy side of the peak, and therefore not all the datum points near resonance are shown. (4) The areas of each yield curve were measured by application of the trapezoidal rule of integration.

#### Anomalies

Several characteristics of narrow ( $p, \gamma$ ) resonance yield curves may be seen from the family of curves in Fig. 1. The most striking characteristic perhaps is the failure of the experimental peaks to shift with target thickness according to rule (1) (see page 1). Close scrutiny will reveal that there is a slight shift from target to target, the shift being to slightly higher energies for thicker targets, but not by as much as half the target thickness. Even for the thick targets, the "peak" shifts only slightly! Thus this behavior violates rules (2) and (3): that the resonance energy for a thick-target curve corresponds to the midpoint of the rise, and that the yield curve for a thick target is symmetric about the midpoint. The peaks, or humps, appearing on the thicker target curves, while not so obvious in the curves of Fig. 1, are nonetheless real effects, and are more pronounced in subsequent figures. Cognizance of this hump was first taken by del Callar (9) who made a series of measurements on the 1317-keV resonance in the  $Al^{27}(p, \gamma)$  reaction. Figure 2, reproduced from del Callar's thesis, shows the hump as observed for the 1317-keV resonance. Initially, it was not clear that this hump was not due to some experimental anomaly;

hence we devoted an entire experimental program to efforts to determine the source or nature of the hump (or to eliminate the hump) under the assumptions that the previously accepted rules were correct and that some facet of the experimental procedure or equipment was introducing aberrations or discrepancies.

A great deal of thought was devoted to possible sources of target imperfections, and efforts were made to eliminate every possible source that was conceived. The results of this program only enhanced the hump. That is, the targets which were considered to be the best showed the highest hump.

The procedures devoted to seeking the cause of the hump, including other effects as well as target effects, were as follows.

1. The possibility that protons, back-scattered from the target or backing material, repassed through the target to cause the hump was considered and eliminated by calculation.
2. Effects due to nuclear Coulomb scattering of the protons were investigated. A calculation indicated that fewer than 0.4 percent of the incident protons are scattered through an angle greater than  $2^\circ$  in penetrating a 1-keV target. A  $2^\circ$  nuclear scattering in aluminum corresponds to an energy loss of about 50 eV.
3. The energy limits of the window of the single-channel analyzer were varied.
4. The angle of observation was changed to include both  $0^\circ$  and  $90^\circ$  (at different times) with respect to the proton beam.
5. Possible malfunctions of the gamma-ray detector electronic equipment were investigated by the interchanging of each of the individual boxed components seriatim.
6. A voltage was applied to the cold tube in front of the target and varied with respect to the target in an effort to determine whether secondary-electron currents could be influencing the beam-current integrator measurements.
7. A voltage was also applied to a beam-defining diaphragm in front of the cold trap (about one meter from the target) and likewise varied.
8. Other possible current-integrator malfunctions were investigated, such as a leakage current due to ionization of air by the gamma rays from the target.
9. The target holder was thoroughly recleaned.
10. The target evaporator system was thoroughly recleaned.

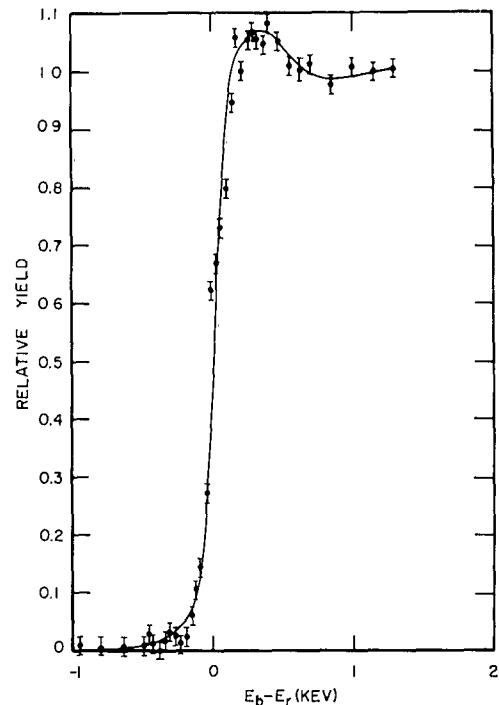


Fig. 2 - An experimental thick-target yield curve near the 1317-keV Al (p,  $\gamma$ ) resonance. Note the definite "overshoot" of the yield just above resonance energy.

11. A different source of aluminum was used for the target evaporations. (It was thought at the time that possibly a target contaminant in the source of aluminum was responsible for the hump.)

12. Different backing materials were tried—tantalum, silver, copper sheet, and evaporated copper on glass—in an effort to determine whether a backing-material contaminant or the backing material was leading to the hump.

13. Tantalum blanks and evaporated copper coatings on glass were bombarded in an effort to determine whether thin "targets" of aluminum existed on the walls of the target holder or elsewhere in the Van de Graaff vacuum system. If such targets did exist, they would give rise to a thin-target resonance curve superimposed on the thick-target step, thus leading to the hump on the thick-target yield.

14. Possible target nonuniformities were considered. That is, if a portion (area) of the target were very thin compared to the rest of the target, it might give rise to a thin-target yield superimposed on the yield from the rest of the target.

15. Another layer of aluminum was evaporated onto a thick target which showed the hump, and a new excitation curve was determined. The effort here was an attempt to determine whether the hump was due to some surface contaminant film or some other surface phenomenon such as oxidation. There were three possible results: two humps, one for each of the old and new surfaces; one hump displaced in energy, corresponding to the old surface; or one hump as if the entire target had been made in one operation. The result obtained was the last mentioned, thus eliminating any surface contaminant as the cause of the hump.

16. Another resonance in the  $\text{Al}^{27}(\text{p}, \gamma)$  reaction was used, 1317 keV.

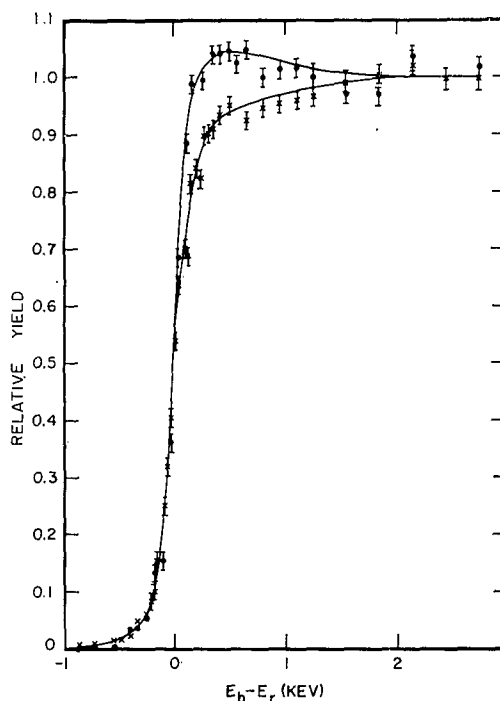
17. Other reactions were studied—the  $\text{C}^{13}(\text{p}, \gamma)$  reaction at 1747 keV and the  $\text{Ni}^{58}(\text{p}, \gamma)$  reaction at 1424 keV and 1843 keV.

None of the aforementioned efforts succeeded in eliminating the hump. On the contrary, the more carefully we made the targets and the measurements, the more pronounced was the hump. We therefore concluded that the hump is a real effect in nature, and is in some way due to the nature of the mechanics of resonance reactions.

There were three ways that we could cause the hump to decrease significantly or disappear completely. (1) The use of a solid commercial sheet of aluminum as the target did not lead to the hump. (2) The use of old targets (more than about one month old) did not lead to the hump. (3) A target which showed the hump was rotated from its normal position ( $90^\circ$  with respect to the bombarding beam) to  $20^\circ$ . This rotation had the effect of increasing the effective thickness (by a factor of 3) of all layers to the bombarding beam—any contaminant film on the surface, the oxidation layer, and the aluminum target itself. Thus the effect of these surface films would be increased. At  $20^\circ$  the target showed essentially no hump, as shown in Fig. 3.

One further experimental condition which was varied was the beam-energy resolution by means of the analyzer-slit variations. The beam-energy width (at half maximum of the distribution) was varied from 0.01 percent to 0.05 percent with the result that the hump was clearly visible for all settings. There was a tendency for the hump to be more pronounced for the more homogeneous beams. This observation is consistent with another one—that the narrower resonances lead to more pronounced humps. Thus the conditions which lead to the hump may be summarized: pure, clean, and uniform targets; narrow resonances; and homogeneous bombarding beams.

Fig. 3 - Experimental yield curves near  $E_r = 992$  keV for an aluminum target (not one of the best) at two different orientations with respect to the bombarding proton beam. The data represented by the solid circles were obtained with the plane of the target perpendicular to the proton beam. The crosses represent the data obtained with the plane of the target making an angle of  $20^\circ$  with the proton beam. Note the lack of "overshoot" in the latter case, where the effective thickness of any contaminating film was increased by a factor of 3 over the former case.



#### Resonance-Width Measurements with Old Targets

One more anomaly which was observed does not directly violate any of the three previously listed rules governing the behavior of nuclear resonance phenomena, but it was unexpected and surprising nonetheless. The discovery of this anomaly arose from the efforts to make measurements of the widths of some very narrow resonances with thick targets. The resonances measured are the 992-keV resonance in the  $\text{Al}^{27}(p, \gamma)$  reaction and the 1747-keV resonance in the  $\text{C}^{13}(p, \gamma)$  reaction. It was observed that the "width" of any particular resonance was different for new and old targets! For example, the interquartile interval\* of the 992-keV resonance in the  $\text{Al}^{27}(p, \gamma)$  reaction, as measured with a beam whose full width at half maximum was 0.01 percent, was typically about 180 eV for a fresh target and about 210 eV for an old target.

The most reasonable explanation for such broadening would appear to be the formation of a film of inert material on the face of the target during a prolonged period of storage. However, such a film would be expected, on the basis of previous concepts, to displace the energy of the resonance. In the instances mentioned here, the energy of the resonance was not appreciably displaced by any such film, if one existed. However, an extremely thin layer of inert material might not displace the resonance energy for much

\*The interquartile interval is the energy interval between the 1/4 and 3/4 points on the thick-target step. The physical significance of this interval depends on the relative values of  $\Gamma$  and the beam-energy spread. The full width at half maximum  $\Gamma$  of a resonance can be determined from the interquartile interval if the effective beam-energy spread is negligible by comparison with  $\Gamma$ . But the corresponding quantity for the beam-energy spread cannot be determined in quite the same way if  $\Gamma$  is negligible since the normal beam-energy distribution does not have the Breit-Wigner shape. A more appropriate shape for the beam-energy distribution is a triangle. The full width at half-height for a triangle corresponds to the interval between the 1/8 and 7/8 points on the integral curve.



Let us now consider in detail the nature of each of the functions  $\sigma$ ,  $g$ , and  $w$ . For narrow resonances, the variations of the de Broglie wavelength and Coulomb penetrability of the protons over the energy range of the resonance, target thickness, and initial beam-energy distribution are negligible. The Breit-Wigner dispersion relation  $\sigma(E)$  then becomes a simple analytic function of the difference between the resonance energy and the proton energy as it makes a nuclear pass.

In principle, the proton beam-energy distribution out of the electrostatic analyzer is triangular in shape if the ratio of the output slit width and the input slit width is set equal to the magnification of the analyzer and if the input distribution is uniform. However, there is some degree of smearing of this shape by the ripple in the voltage applied to the deflector plates. There is a further smearing of the effective beam-energy distribution by the thermal motion of the target nuclei in the target lattice structure (Doppler effect). For most of the data presented herein, the Doppler-effect contribution to the total effective beam width was comparable with that from the analyzer. Therefore we have assumed that the effective incoming beam-energy distribution  $g(E_b, E_i)$  can be represented to a sufficiently accurate approximation by a Gaussian shape with a standard deviation derived (6) from the triangular distribution, the ripple of the applied voltage, and the thermal motion of the target nuclei.

The resonance shape  $\sigma(E)$  can be represented by an exact analytic form, and the incident effective beam-energy distribution  $g(E_b, E_i)$  can be approximated satisfactorily. But the energy-loss distribution  $w(E, E_i, x)$  is the result of a complicated statistical process which presents formidable mathematical difficulties. As will be seen later, the function  $w(E, E_i, x)$  is the key to our explanation of the anomalies, and therefore its proper evaluation and appreciation are of the utmost importance.

#### Determination of the Function $w$

For some purposes it is reasonable to assume that the spread in energy of the beam remains constant as the beam traverses the target. This assumption implies that all particles in the beam lose energy at the same rate. The shape of the function  $w(E, E_i, x)$  is then independent of the depth of penetration  $x$ , becoming simply  $w = \delta[E - (E_i - kx)]$ , where  $k$  is a constant depending on the stopping power of the target material. Actually, it has been known for a long time that such is not the case because of statistical fluctuations in energy loss, but the simplified treatment has appeared justified for the treatment of ( $p, \gamma$ ) resonance phenomena involving thick targets for the following reasons.

Even though it has been known that the energy inhomogeneity of a bombarding beam increases as a function of depth in the target, it has been believed that these fluctuations in energy loss have no significant effect on either the shape or midpoint energy of the step of a thick-target yield curve because every particle that enters a target above the resonance energy ultimately passes through the resonance energy some place in the target, fluctuations in energy loss notwithstanding. Furthermore, it has been believed that these fluctuations in energy loss, while affecting the shape of a thin-target yield curve, do not significantly affect the energy at the peak because of the expected symmetry of the fluctuations in energy loss (Gaussian distribution). Therefore rules (1), (2), and (3) on page 1 have appeared to be valid. The fact that these rules have now been shown experimentally not to be valid leads one to abandon the ideas presented above in this paragraph and to seek a new approach. The following brief sketch of mathematical treatments of the problem of fluctuations in energy loss presents the framework in which the observed anomalies are to be explained.

As early as 1913 Bohr (10) realized that the problem of energy loss of charged particles in penetrating matter was statistical in nature, and he attacked the problem using classical theory and the Rutherford-Bohr model of the atom. (Some of his results were

derived later by Rossi and Greisen (11) using a quantal treatment.) For alpha particles, Bohr showed that the energy-loss distribution has an almost Gaussian shape. This result depends on (a) the fact that the fractional energy loss in any one collision between the alpha particle and an electron is very small and (b) the condition that there be many such collisions (i.e., that the material thickness not be too small). It is reasonable a priori that these conditions lead to an approximate Gaussian distribution.

For the present application (involving protons), requirement (a) above is reasonably satisfied since the maximum energy that a 992-keV proton can transfer to a free electron in one collision is about 2.16 keV (about 0.2 percent of the proton kinetic energy). However, condition (b) is not satisfied for thin targets (few keV) since a proton can sometimes be expected to penetrate a thin target with only a few energy-loss interactions. And for extremely thin targets (<0.5 keV) perhaps there will sometimes be no interaction at all! Thus the Bohr treatment of fluctuations in energy loss is fairly satisfactory for thicker targets (many interactions) but is inadequate for thin targets (condition (b) not being satisfied).

Williams (12), beginning in 1929, extended and improved the results of Bohr, especially for those cases in which the maximum energy that can be transferred in a single collision is an appreciable fraction of the total kinetic energy of the incoming particle. In Williams' results, the most probable energy loss is less than the mean energy loss resulting in an asymmetric and non-Gaussian distribution. Therefore the energy shift of the peak of a distribution of incoming particle energies is less than the average energy loss suffered by the beam. Williams' results are of particular importance for incoming electrons and for thin foils (and to a significant extent also for low-energy protons and thin targets); and he showed that there was good agreement between his theoretical predictions of the shape of the distribution and the experimental results for electrons in the energy range 150-260 keV in traversing thin foils.

Bethe (13), in a series of papers beginning in 1930, took into account the binding of the electrons in the atoms and quantal effects; that is, he included the different probabilities for transitions of the electrons leading to various discrete excited states as well as ionization of the atoms. He made use of the quantity  $I(Z)$ , representing the average ionization potential of an atom of atomic number  $Z$ , in deriving an expression for the average energy loss of a beam of charged particles in traversing a foil or target. His treatment of the problem of fluctuations of energy loss resulted in a Gaussian distribution as did the treatment of Bohr. It was the Bethe-Bohr treatment of the energy-loss process that led to the concepts of  $(p, \gamma)$  reaction phenomena and rules (1), (2), and (3) discussed in the Introduction.

Bethe's result for the average energy loss  $\Delta T_a$  (including both close and distant collisions) of a proton whose velocity is  $\beta c$  and whose energy is small compared with  $10^6$  MeV in passing through a foil of density  $D$  g/cm<sup>3</sup> and thickness  $x$  cm may be written (14)

$$\Delta T_a = \frac{2Cm_e c^2 Dx}{\beta^2} \left[ \ln \frac{4m_e^2 c^4 \beta^4}{(1-\beta^2)^2 I^2(Z)} - 2\beta^2 \right], \quad (2)$$

where  $C$  is the silhouette area of the electrons contained in 1 g of target material based on the classical radius of the electron,  $e^2/m_e c^2$ .

Landau (15), in 1944, made a significant improvement in the theory of the energy-loss process when he attacked the problem from a point of view somewhat like that of Williams. By limiting his consideration to moderately thin foils or targets and bombarding energies not too low, Landau was able to obtain a rigorous mathematical solution to the problem of the distribution of energy losses. His procedure involved the assumption that the probability that the maximum single-collision energy loss will occur is negligibly

small; he could therefore, in his mathematical treatment, allow the maximum single-collision loss to be infinite even though the total energy loss suffered by a particle in traversing the thin foil must be small compared to its total kinetic energy. Thus in the Landau treatment, the possible single-collision energy losses range from zero to infinity with a certain value being the most probable (the peak in the probability distribution). Therefore the probability distribution for a single energy loss (and also for a few energy losses) is asymmetric (the value of the mean energy loss not being equal to the value of the most probable energy loss); consequently the energy distribution of a homogeneous beam of charged particles after traversing a thin foil is asymmetric.

For thicker targets the Gaussian distribution is known to be valid; i.e., it is valid if the width of the distribution is large compared to the maximum energy transferable in a single collision (here we mean the maximum based on kinematics, not the infinite value in the Landau treatment) but small compared with both the bombarding energy and the average energy loss. The asymmetry of Landau's energy-loss distribution is independent of target thickness and therefore does not agree with the symmetric Gaussian distribution, which is valid for thicker targets. Thus there is an intermediate-thickness region in which neither the Gaussian distribution (thick foils) nor the Landau distribution (moderately thin foils) is applicable. Symon (16) in 1948, bridged this gap by solving the problem without neglecting the probability of single-collision maximum-energy transfer and by considering the variation in the single-collision probability function with decreasing kinetic energy of the incoming particle.

Symon points out in his thesis that the distribution curves he has calculated are applicable to incident proton energies above 10 MeV and below 1000 MeV. Both Landau and Symon assumed that the velocity of the incoming particle is large compared to the velocity of the electrons with which the collisions occur. This condition is not completely satisfied for 992-keV protons impinging on aluminum because the K-shell electrons in aluminum have a velocity about 70 percent greater than that of 992-keV protons. However, the assumptions in the theory should hold reasonably well for the other electron shells. Another limitation of both solutions (Landau and Symon) is that neither applies to extremely thin targets because they both neglect fluctuations due to distant collisions (in which the atomic electrons cannot be treated as free). Even though the applicability of Symon's theory to the present case is somewhat questionable, the attitude taken in the present work is that this is the best theory available, and its usefulness is measured by how well it can satisfy the data.

Symon gives for the most probable energy loss  $\Delta T_p$  the expression

$$\Delta T_p = \frac{2Cm_e c^2 Dx}{\beta^2} \left[ \ln \frac{4Cm_e^2 c^4 Dx}{(1-\beta^2) I^2(Z)} - \beta^2 + j \right], \quad (3)$$

which may be compared with Bethe's result, Eq. (2), for the average energy loss.

The dimensionless parameter  $j$  is a mathematical device which enables Eq. (3) to give the proper value for the most probable energy loss for any target thickness. In addition to the parameter  $j$ , Symon introduced two other dimensionless parameters  $b$  and  $\lambda$ . The parameter  $b$  is used primarily for convenience since its employment allows the multiple use of each set of tables. If we represent the coefficient of the bracketed term of Eq. (3) by the symbol  $\xi$ , then the quantity  $b\xi$  has dimensions of energy and is related to the width of the distribution of energy losses. The parameter  $\lambda$  is related to the asymmetry of the distribution, the range of its values being from 1.477 (corresponding to the Landau distribution) to zero (corresponding to Bethe's Gaussian distribution).

Another significant quantity related to the characteristics of the energy-loss distribution is the dimensionless ratio  $G = \xi/E'_m$ , where  $E'_m$  is the maximum energy transferable

to a stationary free electron in a single collision. For the bombarding energies in which we are interested,  $E_m' = 2m_e c^2 \beta^2 / (1 - \beta^2)$ . Symon gives values of the parameters  $j$ ,  $b$ , and  $\lambda$  as functions of  $G$  primarily and  $\beta$  secondarily. For any particular experimental situation, the values of  $G$  and  $\beta$  can be computed immediately. All factors, except  $x$ , involved in the energy-loss distribution for any particular  $(p, \gamma)$  resonance are fixed, and  $G$  is simply proportional to the depth  $x$  in the target. So we may think of the parameters  $j$ ,  $b$ , and  $\lambda$  as functions of  $x$ .

Symon has calculated a family of curves  $\varphi_\lambda(\Delta_w)$ , which give the energy-loss distribution in terms of a dimensionless quantity  $\Delta_w$  (which is the difference between the actual energy loss and the most probable energy loss, expressed in units of  $b\xi$ ). In symbols  $\Delta_w = (\Delta T - \Delta T_p) / b\xi$ .

Since the parameters  $j$ ,  $b$ , and  $\lambda$  are given as functions of the quantity  $G$ , the value of  $G$  serves as a useful criterion for the validity of the special-case solutions to the energy-loss problem. Landau's solution may be used if  $G \ll 1$ , and Bethe's solution may be used if  $G \gg 1$ . In the region of  $G$  values between about 0.1 and 10, neither of these two solutions is valid, and one must use Symon's solution, which is valid for all values of  $G$ .

Finally, the function  $w(E, E_i, x)$ , the probability that a proton whose incident energy is  $E_i$  will lose an energy of amount  $\Delta T = E_i - E$  in going a distance  $x$  through the target, is  $w(E, E_i, x) = \varphi_\lambda(\Delta_w) / b\xi$ .

#### Qualitative Explanation of the Anomalies

It is clear from the foregoing discussion that the formal yield equation cannot be integrated analytically because of the nature of the function  $w(E, E_i, x)$ . Therefore the above treatment of the energy-loss process will now be illustrated in a qualitative, or perhaps semiquantitative, manner before the discussion of the precise numerical integration. The following graphical integration of the formal yield equation aids in developing an intuitive concept of the physical processes involved and also aids in acquiring an understanding of the reasons for the anomalies discovered experimentally.

The order of integration, chosen for purposes of illustration, is  $E_i$ ,  $E$ , and  $x$ . For purposes of simplification the integration over  $E$  is made trivial by the assumption that the resonance shape  $\sigma(E)$  is a rectangle of width 10 eV. This assumption is justified for many  $(p, \gamma)$  resonances because they have resonance widths in this range; and if the resonance width is small compared with the widths of  $g(E_b, E_i)$  and  $w(E, E_i, x)$ , the value of the integral is not sensitive to the precise shape of  $\sigma(E)$ .

Now, consider Fig. 5. A target ( $t = 400$  eV, average energy loss) is bombarded by a proton beam having an initial triangular distribution (whose full width at half height is 200 eV corresponding to a resolution of 0.02 percent, typical for the present series of experiments), curve I. For convenience the interval  $dx$  is chosen to be the thickness of a layer of aluminum corresponding to an average energy loss of 100 eV, leading to four equal layers in the target. The integration of the product  $g(E_b, E_i) w(E, E_i, x)$  over  $E_i$  gives a new function which may be represented by  $[gw](E_b, E, x)$ . Curves of this function for values of  $x$  corresponding to the boundaries between the different layers of the target are shown in Fig. 5 and are labeled II, III, and IV. These curves correspond to the actual beam-energy distributions entering layers B, C, and D, respectively. The integration of the product  $g(E_b, E_i) w(E, E_i, x)$  was performed in a few hours with the use of a desk calculator and Symon's tables (or Landau's tables for targets this thin). It should be noted that even though the initial triangular distribution is idealized, this calculation of the function  $w(E, E_i, x)$  and this integration of the product  $g(E_b, E_i) w(E, E_i, x)$  were performed with sufficient accuracy for many experimental applications.

When the beam has penetrated to the boundary between layers A and B, its average energy  $E_a$  has decreased from the value of the bombarding energy  $E_b$  to the value  $E_b - 100$  eV, and its energy distribution is represented by curve II. Note that curve II is plotted so that point  $E_a$  is located 100 eV below  $E_b$ , the average energy of the beam as it enters layer A. Curve II thus represents the energy distribution of the beam entering layer B on the same energy scale as that of the incident beam (curve I). It is noticed immediately, however, that the peak of curve II (i.e., the most probable energy of protons in the beam entering layer B) has been displaced much less than 100 eV. This situation illustrates the idea stressed in the preceding section: that for thin targets Symon's theory (and also Landau's) results in the calculated most probable energy loss being significantly smaller than the average energy loss.

Curves III and IV are similarly plotted on the same energy scale with their average energies being 200 eV and 300 eV, respectively, below  $E_b$ . One final simplifying assumption is that the incident distribution I is effective throughout layer A, and that distributions II, III, and IV are effective throughout layers B, C, and D, respectively.

The integration over  $x$  can now be performed graphically by figuratively placing a mask overlay representing the assumed intrinsic resonance shape over the beam-energy distributions at the desired relative position of  $E_r$  with respect to  $E_b$ . The relative yield  $y(E_b, t)$  is obtained by essentially adding the ordinates of the four beam-energy distribution curves at  $E_r$ .

The integration process may be visualized as follows. One chooses a value of  $E_b$  relative to  $E_r$ . Suppose this value is  $E_r - 100$  eV. This means that we place  $E_r$  100 eV to the right of  $E_b$  on the graph of Fig. 5. The yield from each layer of the target is proportional to the amount of beam at the resonance energy  $E_r$  in that particular layer. The amount of beam at resonance energy in each particular layer is proportional to the ordinate of the curve representing that layer at  $E_r$ . The yield from the entire target is the sum of

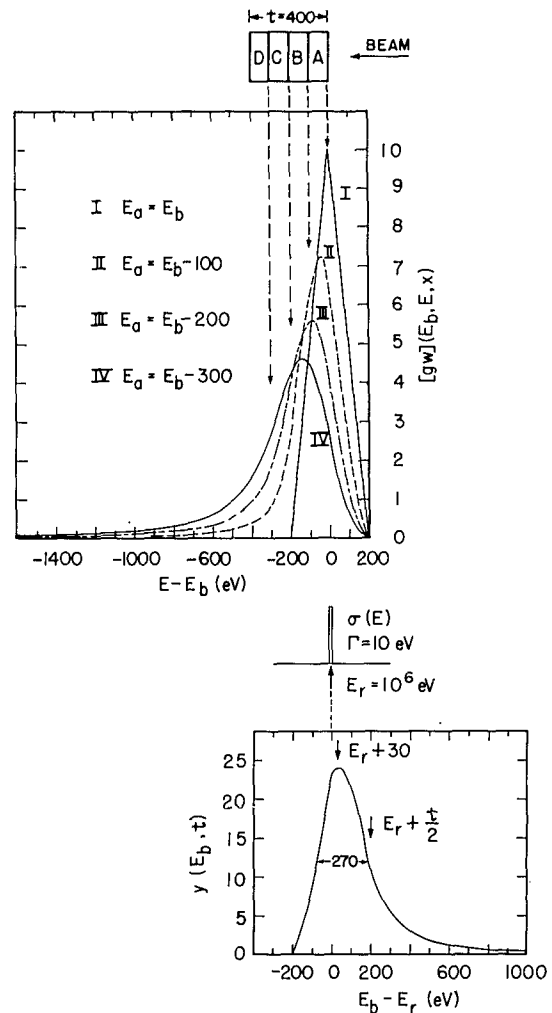


Fig. 5 - The processes leading to a computed yield curve. Curves I-IV show the beam-energy distributions entering layers A-D, respectively, of the target. The average energies  $E_a$  for each distribution are 100 eV lower for each successive distribution. The "integration of the yield equation" is accomplished by sweeping  $\sigma(E)$  across these distributions from right to left adding the respective ordinates, and plotting these points in the lower graph from left to right. Note that the width of the resulting yield curve is narrower than indicated by the usual combination of the target thickness and beamwidth, and that the peak is displaced only slightly from  $E_r$ , and is not at all near  $E_r + t/2$ .

the yields from the four layers. Thus the yield from the entire target for  $E_b = E_r - 100$  eV is proportional to the sum of the ordinates at  $E_r$ . This sum can be easily obtained from Fig. 5. Next let us choose  $E_b$  to be equal to  $E_r$ . The yield for this new value of  $E_b$  is proportional to the sum of the ordinates at the new position of  $E_r$ . This sum can also be easily visualized from Fig. 5. Thus the yield from the entire target as a function of  $E_b$  is proportional to the sum of the ordinates of all the distribution curves as one places  $E_r$  at various positions with respect to  $E_b$ . (Experimentally,  $E_r$  is fixed, and one chooses  $E_b$  with respect to  $E_r$ , but it appears easier to perform the integration by moving  $E_r$  across the family of distribution curves rather than moving the family of distribution curves across  $E_r$ . Increasing  $E_b$  with respect to  $E_r$  is equivalent to moving  $E_r$  across the family of curves from right to left.)

Values of  $y(E_b, t)$  have been computed from Fig. 5 for values of  $E_b$  from  $E_r - 400$  eV to  $E_r + 1000$  eV in steps of 100 eV, except for the interval from  $E_b = E_r$  to  $E_b = E_r + 100$  eV, where 10-eV steps were used. The resulting yield curve is shown also in Fig. 5. Note that the peak occurs at an energy only slightly higher than  $E_r$  and not at all near  $E_r + t/2$ !

The essential qualitative features that lead to these results are the asymmetric shape resulting from the fluctuations in energy loss and the fact that the most probable energy loss is significantly less than the average energy loss. At a bombarding energy  $E_b = E_r + t/2$  ( $E_r$  is at -200 eV on the upper graph of Fig. 5), a large fraction of the protons in the beam (i.e., the area under curve IV to the right of  $E_r$ ) penetrate the entire target without losing enough energy to pass through resonance! With this knowledge, one is therefore hardly surprised that the experimental peak does not occur at  $E_b = E_r + t/2$ .

Figure 5 treats a thin target and the anomaly of the failure of such thin-target yield peaks to shift in energy by half the target thickness. The hump on the thick-target yield curve can be visualized in a similar manner since it is only a slightly different manifestation of the same phenomenon. For a thick target there would be a large number of distribution curves following the pattern of those of Fig. 5 — one curve corresponding to each layer of the thick target, each successive curve being less peaked and broader than the preceding one and shifted toward lower energies. The yield curve can be visualized as before for the four-layer target by mentally imagining the sum of the ordinates of this large number of distribution curves as  $E_r$  moves from right to left. It is seen that the midpoint of the rise of the yield curve is reached when  $E_r$  is somewhat to the right of  $E_b$ , corresponding to the bombarding energy being somewhat below the resonance energy. It is also seen that the sum curve or yield curve reaches a maximum when  $E_r$  is slightly to the left of  $E_b$  because the first few distributions have the highest and sharpest peaks. This maximum is the hump.

The difference in interquartile interval for  $H_1^+$  beams on old and new thick targets can be understood also in terms of Fig. 5. If an inert layer 100 eV or less in thickness coats the target during the aging period, the displacement is hardly noticeable; but instead of the yield starting with beam-energy distribution I, it begins with II. Thus for the same output beam-energy distribution from the electrostatic beam-energy analyzer on both the old and new targets, the effective distribution that strikes the new target is equivalent to I, and the effective distribution that strikes the old target equivalent to II. The respective widths of the two distributions at half height are 200 eV and 250 eV. Therefore it is clear that the old target, if it is coated with a contaminant layer 50 to 100 eV thick, will show a wider interquartile interval.

The "rotated-target" experiment can also be visualized with the aid of Fig. 5. Since all layers are about three times thicker when at an angle of  $20^\circ$  to the beam than at  $90^\circ$ , an aluminum oxide layer of, for example, 30 eV would appear at  $20^\circ$  to be about 100 eV thick. Since the target in  $Al_2O_3$  is diluted by a factor of about two compared with pure aluminum, the distribution curves of Fig. 5 corresponding to the  $Al_2O_3$  layer (assumed

above to be about 100 eV at 20°) should be multiplied by about 1/2 before integrating. Thus the contribution of distribution I toward the hump is effectively nullified, and the hump will disappear since distribution I was its main contributor. In addition any layer of inert coating material would also be increased in thickness at 20°, so layers as thin as 20 to 30 eV at 90° would become significant at 20°.

#### Integration of the Formal Yield Equation

The above graphical treatment has presented qualitative reasons for the unexpected shapes of the experimental yield curves. For precise quantitative comparisons between theory and experiment an evaluation of Eq. (1) with the mathematical shapes of  $g(E_b, E_i)$  and  $\sigma(E)$  was necessary. No part of the yield equation can be integrated analytically. The normally integrable Breit-Wigner dispersion relation cannot be integrated here because its independent variable  $E$  is also contained in a nonexplicit way in the function  $w(E, E_i, x)$ . Thus in order to calculate the yield for a given value of bombarding energy, a numerical integration by a high-speed digital computer was required. (An approximate numerical evaluation of the yield equation for a particular set of parameters has been made by Kennedy and Jones (17).)

It appears that the most logical order of performing the integration is to integrate first over  $x$ , since  $x$  is contained only in the function  $w(E, E_i, x)$ . If one does this, he obtains a function  $w(E, E_i, t)$  giving the energy-loss distribution applicable to the target as a whole. The remaining integration is then a twofold integration over the variables  $E_i$  and  $E$ . Unfortunately this procedure did not occur to us until after the integrations had been performed in the order  $E$ ,  $E_i$ , and  $x$ . This order required a threefold integration, and it is this latter integration which is described in the following sections.

General Considerations - The evaluation of the yield equation involves the assignment of numerical values to various parameters contained in the functions making up the yield equation. Some of these parameters can be assigned uniquely from the experimental configuration: (a) the resolution of the electrostatic analyzer and (b) the target atomic number, atomic weight, density, Debye temperature, and thermodynamic temperature. Values of other quantities cannot be assigned a priori but instead must be assigned on the basis of comparison with the experimental data. These quantities are the thickness of the target  $t$ , the natural width of the resonance  $\Gamma$ , and the chemical structure of the target (e.g., surface contamination and target purity).

It might appear at first thought that the target thickness  $t$  could be determined in advance, and, in principle, such is the case; the target may be weighed and its area measured. But a more customary way of determining target thicknesses in those cases not involving absolute cross-section measurements is the determination of the full width, in energy units, at the half-height position of a narrow-resonance yield curve. That was the original plan for the present series of experiments. But one of the results of the present work is that this procedure for determining target thicknesses is not always correct. This fact may be thought of as another anomaly. (We were thus caught in our own web!) Therefore absolute thickness measurements of the targets are not available. So the upper limit  $t$  necessary for the integration of the theoretical yield equation can be determined only after the definite integral has been evaluated. Thus we must use a bootstrap type of calculation.

If the thickest target of the E series, E-1, were thick enough to produce a Gaussian distribution of proton energies, the full width at half maximum of the experimental yield curve would be very nearly the target thickness in energy-loss units. A criterion of validity for the Gaussian distribution is that the parameter  $G$  be large compared with unity. For target E-1, the value of  $G$  is only about 1.7. Therefore the full width at half height of the experimental yield curve is not strictly the target thickness; however, it so

happens that, for the present purposes, the thickness  $t$  for target E-1 obtained from the experimental yield curve is sufficiently accurate a posteriori.

The natural widths  $\Gamma$  of the particular resonances used in the present series of measurements are not accurately known, but approximate values are available from previous measurements, and the validity of the numbers used for the widths can be judged to some extent by the comparison of the calculated yield curves with the data.

Aluminum is very active chemically and therefore oxidizes very rapidly in air. Normally, a piece of solid aluminum has a tough coating or skin consisting of an extremely thin layer of aluminum oxide. Since our targets were exposed to air between evaporation and bombardment, we are sure that such an extremely thin layer of aluminum oxide (at least a monomolecular layer) exists. We are also sure that some degree of oxidation exists throughout the entire volume of the targets because no vacuum is perfect, and some oxidation always occurs during the evaporation process. But we do not know a priori the degree of these oxidations.

For thick targets the degree of volume oxidation can be determined in a reasonably direct manner, but such is not the case for the thinner targets. Because we do not know in advance the thickness of any existing inert surface contamination or the degree of oxidation of the aluminum in the thin targets, these are regarded as independent parameters whose values may be chosen (within limits) to provide adjustment between the calculated curves and the experimental data.

Detailed Considerations - The range of integration over the target thickness (whose independent variable is  $x$ ) is from 0 to  $t$ , where  $t$  is the experimentally determined thickness of the target in units of  $10^{-5}$  cm. The integration of the yield equation over all three variables ( $E, E_i, x$ ) gives the yield for a particular value of  $E_b$  and  $t$ . The fact that the integral of the yield over  $E_b$  is equal to  $t$  is the reason for the normalization of the experimental yield curves of Fig. 1 in terms of target-thickness units of  $10^{-5}$  cm. A variable interval over  $x$  was used since the evaluation is most sensitive near  $x = 0$  and least sensitive at large values of  $x$ . Various values of  $dx$  were tested, and the largest values of  $dx$  leading to an error not greater than 0.2 percent were accepted.

For practical numerical integration, the limits of integration must be finite. Therefore it was necessary to choose reasonable upper limits for integration over the functions  $\sigma(E)$  and  $g(E_b, E_i)$ . Similarly, it was not useful or practical to extend the lower limits down as far as the theoretical value zero. For the dispersion relation  $\sigma(E)$ , the upper and lower limits were chosen to be  $\pm 100 \Gamma$ . Only about 0.8 percent of the area under this curve lies outside these limits. For the function  $g(E_b, E_i)$ , the upper and lower limits were chosen to be  $\pm \sqrt{14} \Delta_t$ , where the quantity  $\Delta_t$  is the standard deviation of the Gaussian expression representing  $g(E_b, E_i)$ . These limits were chosen because they include 99.9 percent of the total area under the Gaussian curve.

The integration interval for the function  $g(E_b, E_i)$  was chosen to be constant and of a magnitude such that a maximum error of 0.1 percent was introduced into the calculation. The integration interval for the dispersion relation was chosen to be variable with large steps taken on the nearly flat portion in the tail and small steps taken in the main body of the curve (near  $E = E_r$ ). The intervals were chosen so that an error of not more than 0.1 percent was introduced into the calculation by the choice of interval.

The functions  $g(E_b, E_i)$  and  $w(E, E_i, x)$  were normalized such that their integral was unity. The integral of the Breit-Wigner relation was normalized by the factor  $\Gamma/2\pi$ .

At  $x = 0$  the function  $w(E, E_i, x)$  becomes a delta function. Therefore the yield expression for this special case was evaluated first.

For a given value of  $x$  the quantity  $G$  was determined, and from a stored table the quantities  $j$ ,  $b$ , and  $\lambda$  were found. The quantity  $\lambda$  was used to determine the proper energy-loss distribution curve in the following manner. Various distribution curves for values of  $\lambda$  are given by Symon. (We recomputed these curves with a smaller interval in  $\Delta_w$  and for several additional values of  $\lambda$ . The Landau curve, corresponding to  $\lambda = 1.477$ , was recently re-evaluated by Börsch-Supan (18).\*) These distribution curves were stored in the computer in the form of tables with arguments  $\lambda$  and  $\Delta_w$ . When a given value of  $\lambda$  was found from the given value of  $x$ , a new distribution curve was constructed by interpolation between the two curves whose associated values of  $\lambda$  bracketed the calculated  $\lambda$ . For the Landau curve,  $\lambda = 1.477$ , values up to  $\Delta_w = 65$  were placed into the table. For values of  $\Delta_w$  greater than 65 (corresponding to relatively large energy losses) the single-collision cross section was used. This quantity is  $(1/b\Delta_w)^2$ . It is of interest to note that for values of  $\Delta_w$  larger than 4 the Landau curve very closely approximates the single-collision cross section. As recommended by Symon, values of  $\Delta_w$  which corresponded to an energy loss greater than the maximum which can be transferred to an electron in a single collision were not permitted in the calculation. Consequently for a more nearly perfect normalization of the Landau curve, the probability for a given energy loss was multiplied by  $e^G$ . By interpolation of quantities found from a stored table, the probability for a given energy loss  $\Delta T$  corresponding to a particular value of  $\Delta_w$  was found.

Differences in target material as a function of  $x$  were accommodated by the program for only one change of material. That is, from  $x = 0$  to  $x = x_1$ , one kind of material could be assumed; and from  $x = x_1$  to  $x = t$  another kind of material could be assumed. A "reactivity" factor,  $F$ , was introduced. For example, in the case of pure aluminum  $F$  was defined as unity, and in the case of aluminum oxide  $F$  was found from the product of the fraction of aluminum by weight in  $Al_2O_3$  and the ratio of the densities of  $Al_2O_3$  and  $Al$ . If the material was assumed to be completely inert relative to the particular resonance, the factor  $F$  was assigned the value zero.

In all cases in this calculation the weighted parameters as defined by Symon were used. Justification for this was based on the least restrictive condition, in which the total energy loss is very much less than the incident energy (see Ref. 16, page 140).

For small values of  $x$  the spread in a given energy-loss distribution curve was less than the spread in either the Gaussian distribution or the dispersion curve. For these cases the integration interval was chosen in relationship to the energy-loss distribution curves. A variable interval was used over the distribution curves and was chosen so as to introduce an error not greater than 0.1 percent in the calculation.

Simpson's one-third rule was used for all integrations. The total error due to the numerical processes in the evaluation of the yield equation was not greater than 2 percent. No estimate of the error introduced through limitations of the theory has been made.

#### Comparison of the Integrated Yield Equation with the E-Series Targets at the 992-keV Resonance

In order to determine a starting point for the degree of volume oxidation to be assumed for the thick aluminum targets, we measured the thick-target resonance step for

\*The peak of the Landau curve occurs at a slightly negative value of  $\Delta_w$ . This value of  $\Delta_w$  can be used to find the value for  $j$  used for computing  $\Delta T_p$  in the limiting case of thin foils where the Landau expression is valid. Landau (15) gives the value  $j = 0.37$ . From the re-evaluation by Börsch-Supan the value found for  $j$  is 0.203. This is precisely the value which is computed from the equations given by Symon for  $j$  in the limiting case of thin foils, and is the value used for the calculations herein.

the 992-keV resonance using two different targets under the same detector geometry and other conditions. The first target was known to be essentially 100 percent  $\text{Al}_2\text{O}_3$  (an anodized aluminum sheet), and the second target was target E-1 (thickest of the E series). The ratio of heights of the thick-target resonance steps for the  $\text{Al}_2\text{O}_3$  target and target E-1 indicated that target E-1 was more than 90 percent aluminum. In order to simplify the starting point for the bootstrap calculation, we assumed target E-1 to be 100 percent aluminum. As will be seen later it was necessary to modify this assumption; however, sufficient accuracy was obtained without introducing an iterative procedure.

The target thickness  $t$ , obtained experimentally in energy units, was converted to units of  $10^{-5}$  cm by the use of standard energy-loss theory, including K and L shell corrections, and the handbook value of the density of aluminum,  $2.7 \text{ g/cm}^3$ . (The actual density of the evaporated aluminum may be different from this handbook value, but no error can result from the use of this value because the density cancels in the calculation. The density is used only for purposes of convenience.) The quantity  $I(Z)$  was taken to be 165 eV (19).<sup>\*</sup> Under the assumptions that the integrated experimental yield is proportional to the number of aluminum atoms per unit area and that the targets consist of pure aluminum, the thicknesses in units of  $10^{-5}$  cm of the remaining targets were found by comparisons of the values of the numerical integrations of their respective experimental yield curves with that of target E-1. The ratios of thicknesses for successively numbered targets (i.e., adjacent targets in the evaporator) thus determined were within a few percent of a factor of 2, which is in good agreement with the factor expected from the target evaporator geometry as described.

To compare the experimental data with the calculated curves, we normalized the experimentally obtained yields by equating the areas under the experimental and calculated curves. This procedure normalized the ordinate values. Then to determine the resonance energy  $E_r$ , the abscissa values were aligned visually.

The intrinsic resonance width  $\Gamma$  of the 992-keV resonance was taken to be 100 eV (6).

There is a resonance (20) of relative intensity 4 percent about 8 keV above the 992-keV resonance. The existence of this resonance was ignored in all the calculations.

As stated previously, different analyzer resolutions were used at different times. (This situation was not deliberately planned this way. We had originally intended to repeat the measurements with constant resolution, but the increased scope of the experiments as a function of time precluded our indulging in the luxury of further repetition.) For targets E-2 through E-6, an analyzer resolution of 0.02 percent was used, and for targets E-1 and E-7, an analyzer resolution of 0.05 percent was used. It has been our experience that a theoretical analyzer resolution of 0.05 percent does not in fact occur, because when the slit is this wide the effective distribution of particle energies at the input to the electrostatic analyzer is not uniform (6). Thus the true beam-energy resolution for targets E-1 and E-7 is not known a priori. However, for a resolution of 0.02 percent the experimental conditions are quite well known; therefore the comparison of the experimental data with the calculated yield curves was started with target E-6.

Target E-6 - The results of the calculation and the normalized datum points are shown in Fig. 6. Curve I results when the target is assumed to be pure aluminum. Curves II and III result when the target is assumed to be fully oxidized, the difference being in the value assigned to  $I(Z)$ , 125 eV for curve II and 105 eV for curve III. The value  $I(Z) = 125 \text{ eV}$  is obtained from the geometric average of the ionization potentials of aluminum (165 eV) and oxygen (108 eV). The value  $I(Z) = 105 \text{ eV}$  is found when one

<sup>\*</sup>Reference 19 gives for aluminum  $I(Z) = 163 \text{ eV}$ . Our value of 165 eV is an arbitrary round-off.

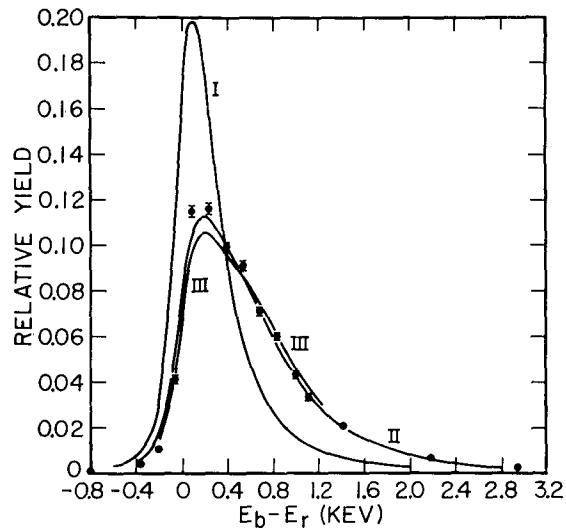


Fig. 6 - Theoretical yield curves and datum points for target E-6,  $H_1^+$  beam-energy spread 0:02 percent, and 992-keV resonance. Curve I, the target consists of pure aluminum. Curve II, the target consists of pure  $Al_2O_3$ ,  $I(Z) = 125$  eV. Curve III, the target consists of pure  $Al_2O_3$ ,  $I(Z) = 105$  eV. The enhanced asymmetry of curves II and III is due to the oxidized targets being thicker, resulting in greater fluctuations in energy loss.

assumes the ionization potential of aluminum to be 150 eV and the ionization potential of oxygen to be 80 eV. These assumed values are not inconsistent with numbers appearing in the literature (21). The second set of numbers, 150 eV and 80 eV, were used in order to justify forcing a low value of  $I(Z)$  for  $Al_2O_3$ . This low value was used to test the sensitivity of the shape of the yield curve to the value of  $I(Z)$ . The agreement between curve II and the datum points of Fig. 6 implies that a consistent, but not necessarily unique, set of conditions is that target E-6 is essentially fully oxidized and the value  $I(Z)$  for  $Al_2O_3$  is about 125 eV.

Target E-7 - Figure 7 illustrates the results pertaining to target E-7. As before, curve I is for a pure aluminum target and an analyzer resolution assumed to be 0.02 percent. Curves II and III are for a completely oxidized target and for assumed resolutions of 0.03 and 0.05 percent, respectively. The somewhat better agreement of the data with curve II indicates that the effective analyzer resolution at a setting of 0.05 percent is substantially better than 0.05 percent, as expected from previous experience (6).

Target E-5 - The results for target E-5 are shown in Fig. 8. The conditions for the different curves are as follows: Curve I, no target oxidation; curve II, the front 20 percent of the aluminum is fully oxidized, but no other oxidation exists; curve III, the target is 67 percent oxidized throughout its entire volume. Although the agreement between the experimental points and the calculated curves in the vicinity just above resonance energy is not quite so good as for Figs. 6 and 7, the agreement for curve III at higher energies is as good. Although all three curves represent targets with the same amount of aluminum, the targets they represent are not the same thicknesses in energy-loss units. That

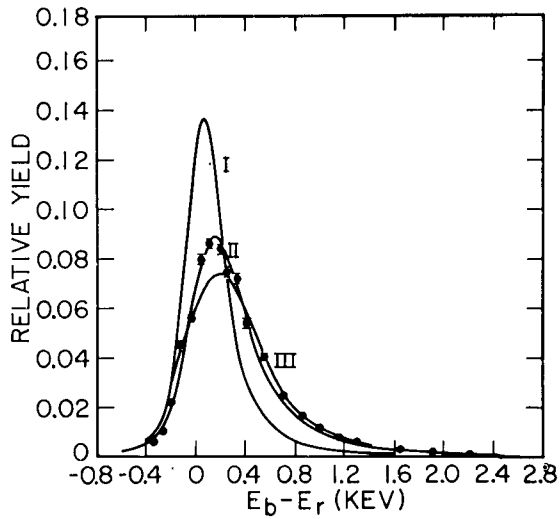
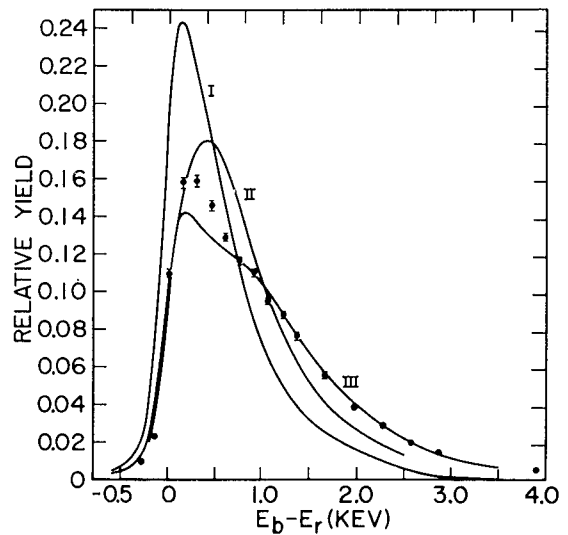


Fig. 7 - Theoretical yield curves and datum points for target E-7,  $H_1^+$  beam-energy spread nominally 0.05 percent, and 992-keV resonance. Curve I, the target consists of pure aluminum. Curve II, the target consists of pure  $Al_2O_3$ ,  $I(Z) = 125$  eV, and the effective  $H_1^+$  beam-energy spread is 0.03 percent. Curve III, the same as II except that the effective  $H_1^+$  beam-energy spread is 0.05 percent.

Fig. 8 - Theoretical yield curves and datum points for target E-5,  $H_1^+$  beam-energy spread 0.02 percent, and 992-keV resonance. Curve I, the target consists of pure aluminum. Curve II, the front 20 percent of the aluminum is completely oxidized, but the rest of the target is pure aluminum. Curve III, the target is 67 percent oxidized throughout its entire volume. Curve III represents a thicker target than the others, and shows the beginning of the "intermediate thickness" target characteristics.



is, if target E-5 had experienced no oxidation, it would have been 1.2 keV thick. Curve III corresponds to a target of thickness 2.0 keV. The three curves illustrate the effects of the different thicknesses. The irregularity of curve III about 1 keV above resonance energy shows the beginning of the characteristics of the "intermediate thickness" uniform composition target.

The three curves of Fig. 8 represent three different oxidation conditions for target E-5. It appears likely that some other oxidation condition, perhaps intermediate between II and III, would give significantly better agreement in the vicinity just above resonance energy. No other curve has been computed for such an intermediate oxidation condition because II and III illustrate adequately the basic effect of target composition on yield curve shape.

Targets E-4 and E-3 - Figures 9 and 10 show the data and calculated curves for targets E-4 and E-3, respectively. Both of these targets exhibit intermediate thickness characteristics; that is, they show neither the reasonably symmetric shape of really thin targets nor the plateau shape of really thick targets. For the various curves of Figs. 9 and 10, different percentages of aluminum are assumed to be oxidized. The oxidized aluminum is assumed to be that part near the front face of the target, and in this layer, oxidation is assumed to be complete. The percentages of aluminum assumed to be oxidized are as follows: 9-I, 0%; 9-II, 5%; 9-III, 10%; 10-I, 0%; 10-II, 2.5%; 10-III, 3.7%. It appears from the shapes of the various theoretical curves and the experimental curve in Fig. 9 that better agreement would have been obtained if the assumed oxidation had been tapered from 100 percent near the target face to lower values for the deeper layers. Curve 10-III was not computed beyond about 2 keV above  $E_r$  because it would not have been significantly different from 10-II. Observe that the peaks of the calculated curves do not shift by an amount equal to half the target thickness, thus agreeing with the experimental data which first demonstrated this anomaly and thereby causing it to be not an anomaly at all!

Targets E-2 and E-1 - Figures 11 and 12 show the data and the calculated curves for targets E-2 and E-1, respectively. These targets may be considered to be thick since these curves do exhibit a plateau shape typical of thick targets. The percentages of oxidation assumed (on the same basis as given above for targets E-4 and E-3) are as follows: 11-I, 1.3%; 11-II, 2.6%; 12-I, 0.7%; 12-II, 1.3%.

In some respects the hump may be considered to begin to become apparent with the intermediate thickness targets E-4 and E-3; but those targets are sufficiently thin that the hump appears to be simply the peak of the curve not displaced much from resonance energy. For targets E-2 and E-1 the calculated curve shows a definite hump. It so happens that the data of target E-2 do not show much of a hump because this target apparently had a significant amount of oxidation on its face. The data for target E-1 do show the hump although not in a pronounced way, and other targets show it better. On the abscissa scale used for Figs. 11 and 12, the different curves tend to merge in all energy regions except the vicinity of the hump. Therefore only one curve is shown in the higher energy region.

The dip and rise following the hump may or may not be a real effect. The amount of this dip is about 2.5 percent of the plateau height, and therefore is rather small. It is possible that the numerical procedures in the integration led to this dip. The size of the hump, in contrast to the size of the dip, is about 25 percent for a pure target.

#### Comparison of the Integrated Yield Equation with Other Data

Rotated Target - The thick target used for the rotated-target experiment was not one of the E series. The experimental details are described in a previous section,

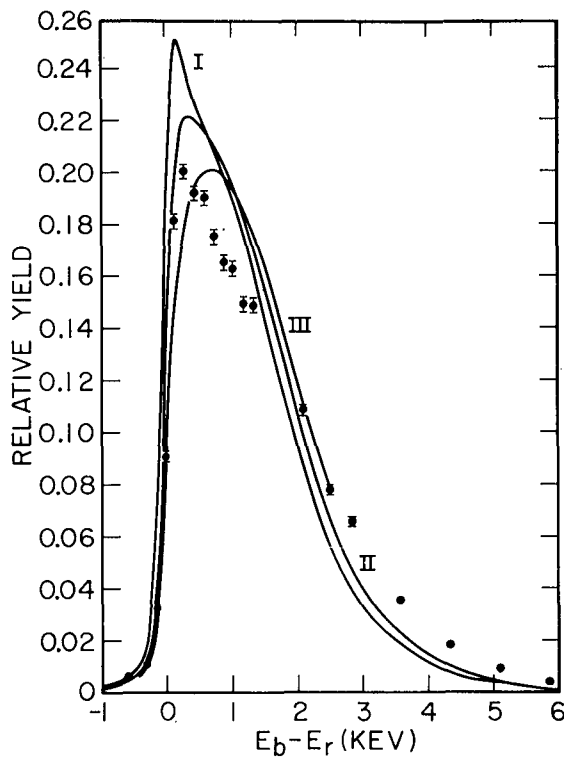


Fig. 9 - Theoretical yield curves and datum points for target E-4,  $H_1^+$  beam-energy spread 0.02 percent, and 992-keV resonance. The different curves represent different percentages of oxidation confined to the front of the target: I, 0%; II, 5%; III, 10%. Note that the peak for a pure aluminum target (I) is hardly shifted at all from resonance energy. Note also the extra point of inflection of I, characteristic of "intermediate-thickness" targets.

Fig. 10. - Theoretical yield curves and datum points for target E-3,  $H_1^+$  beam-energy spread 0.02 percent, and 992-keV resonance. The different curves represent different percentages of oxidation confined to the front of the target: I, 0%; II, 2.5%; III, 3.7%. These targets are on the verge of being "thick," but note that the peaks of the curves are still only slightly shifted from resonance energy.

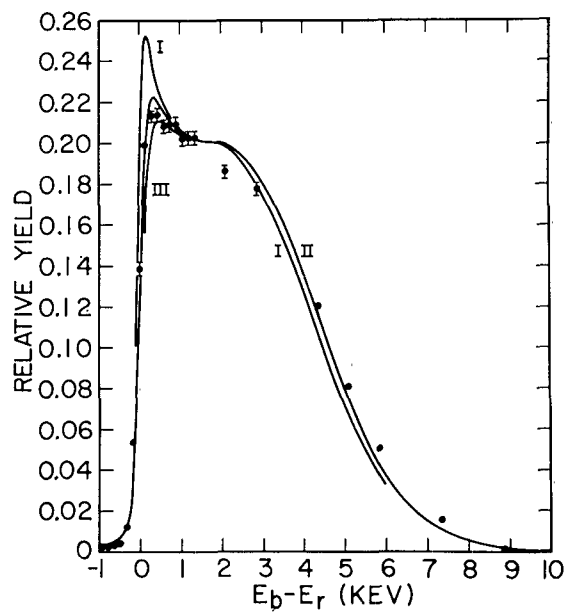


Fig. 11 - Theoretical yield curves and datum points for target E-2,  $H_1^+$  beam-energy spread 0.02 percent, and 992-keV resonance. The different curves represent different percentages of oxidation confined to the front of the target: I, 1.3%; II, 2.6%. Target E-2 is the thinnest target to show a "thick-target plateau." But as with somewhat thinner targets, the peak is shifted only slightly from resonance energy.

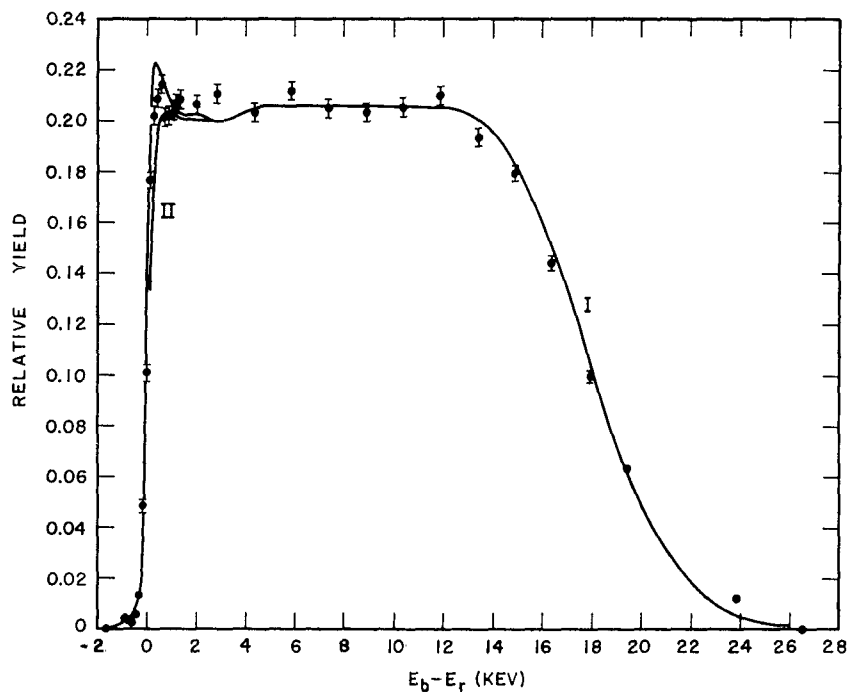
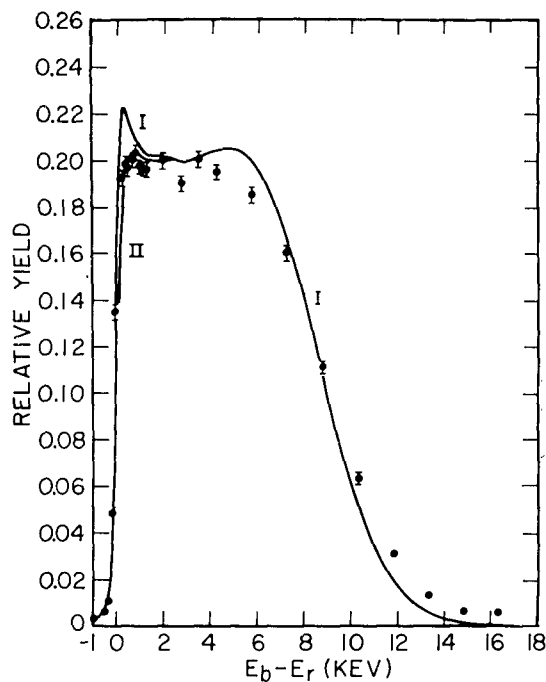


Fig. 12 - Theoretical yield curves and datum points for target E-1,  $H_1^+$  beam nominal energy spread 0.05 percent, and 992-keV resonance. The different curves represent different percentages of oxidation confined to the face of the target: I, 0.7%; II, 1.3%. The wiggles in I to the right of the peak might exist in nature or might be the result of approximations in the computation.

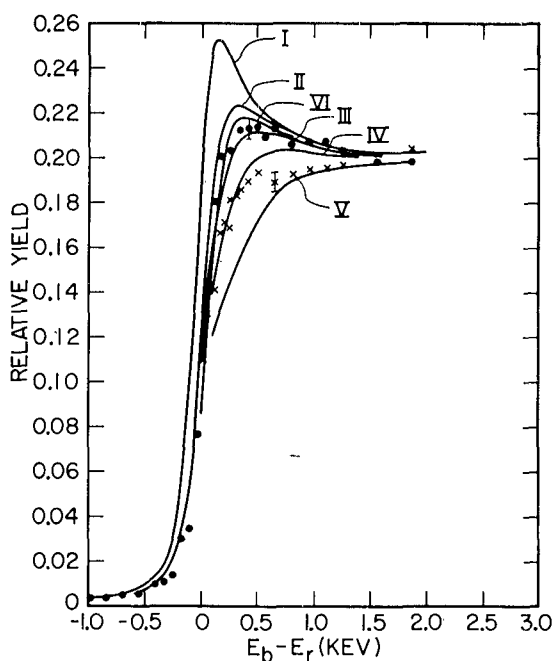


Fig. 13 - Theoretical yield curves and datum points for "rotated-target" experiment. The target was thick, the  $H_1^+$  beam-energy spread was 0.02 percent, and the resonance was at 992 keV. The solid circles correspond to the target being  $90^\circ$  to the beam; the crosses,  $20^\circ$ . The different curves I-V represent different thicknesses of surface oxidation: I, 0 eV; II, 260 eV; III, 390 eV; IV, 520 eV; V, 780 eV of  $Al_2O_3$ . Curve VI represents a pure aluminum target coated with a layer of  $C^{12}$ , 100 eV thick.

get, while the displacement is near zero for the coated and partially oxidized targets, and is in the opposite direction for the thicker layers. Thus for a target that is slightly dirty, there may be no displacement!

It is also of interest to note that the slope of the rise in the calculated thick-target yield curve is less when the target surface is contaminated than when only pure aluminum is assumed. This effect explains qualitatively the old vs new target data, in which the old target always showed a greater interquartile width than did the new target.

**1317-keV Resonance** - Figure 14 shows the experimental data and two calculated curves for the 1317-keV resonance and a thick aluminum target. Curve I represents a pure aluminum target, and curve II corresponds to a target with a 340-eV-thick  $Al_2O_3$  layer on its surface. The experimental resolution was 0.01 percent, and the intrinsic resonance width  $\Gamma$  was assumed to be 50 eV because the experimental data indicated a narrower width for the 1317-keV resonance than for the 992-keV resonance. The hump is clearly visible in both the experimental data and the calculated curves. The agreement between curve II and the data is excellent. Note that the midpoint of the rise of the calculated curve for the pure target, curve I, is below resonance energy as was the case

and the data are shown in Fig. 13 along with several calculated curves. The solid circles represent the data for which the target was perpendicular to the beam, and the crosses represent data for which the plane of the target was at an angle of  $20^\circ$  with respect to the proton beam. The different curves I to V correspond to assumptions of surface oxidation of the aluminum to different thicknesses as follows: I, 0 eV; II, 260 eV; III, 390 eV; IV, 520 eV; V, 780 eV. Curve VI was calculated with the assumption that a layer of  $C^{12}$ , 100 eV thick, coated the target, but no oxidation existed. The rotation of the target in the experimental arrangement should have caused whatever layer of contaminant that existed on the target to increase a factor of 3 in effective thickness. The oxide layer assumed for curve V was a factor of 3 thicker than that for curve II. A visual inspection indicates that the apparent change in oxide layer thickness for the experimental data was less than this factor of 3, but qualitatively the calculations explain the change in shape for the two different experimental conditions. Note the relative effectiveness of  $C^{12}$  and  $Al_2O_3$  in depressing the hump.

The abscissa scale of Fig. 13 allows one to see the displacement from resonance energy of the midpoint of the rise for the pure target. The amount of this displacement can be seen to be 100 eV for the pure tar-

for the 992-keV resonance. One would expect that the amount of this displacement would be greater for the 1317-keV resonance, other parameters being equal. Actually, the amount is somewhat less for the 1317-keV resonance, and this fact is due to the smaller value for the beam-energy resolution in the latter case.

1843-keV Resonance in the  $Ni^{58}$  ( $p, \gamma$ ) $Cu^{59}$  Reaction - An electroplated target of  $Ni^{58}$  was prepared and was believed to be about 5 keV thick; but when it was used for measurements of the gamma-ray yield from the 1843-keV resonance, the resulting yield curve shape did not have the appearance typical of a thick target, as can be seen in Fig. 15. The target thus appeared to be inferior even though we had believed it to be one of our best. However, the shape of the yield curve can be fully explained by the integration of the yield equation. Curve I was computed under the assumption of a pure  $Ni^{58}$  target 5.3 keV thick, an intrinsic resonance width of 50 eV, and a beam resolution of 0.02 percent. Curve II is the same except for an assumed layer of  $C^{12}$ , 60 eV thick, on the target surface. The agreement between the data and curve II is excellent.

It is interesting to compare the 1843-keV resonance yield curve with that from the 992-keV resonance and a target of about the same thickness, E-3, 4.7 keV, Fig. 10. The experimental height of the hump for the 1843-keV resonance is the highest we have ever observed, being about 28 percent of the height of the plateau. For purposes of comparison the plateau height for a thick  $Ni^{58}$  target is shown by curve III, Fig. 15, calculated for a 10-keV target. By contrast, the experimental height of the hump for target E-3, Fig. 10, is about 5 percent of the plateau height.

The enhanced appearance of the hump for the  $Ni^{58}$  target is at the expense of the appearance of the plateau. That is, the 5.3-keV  $Ni^{58}$  target showed less of a plateau than the 4.7-keV  $Al^{27}$

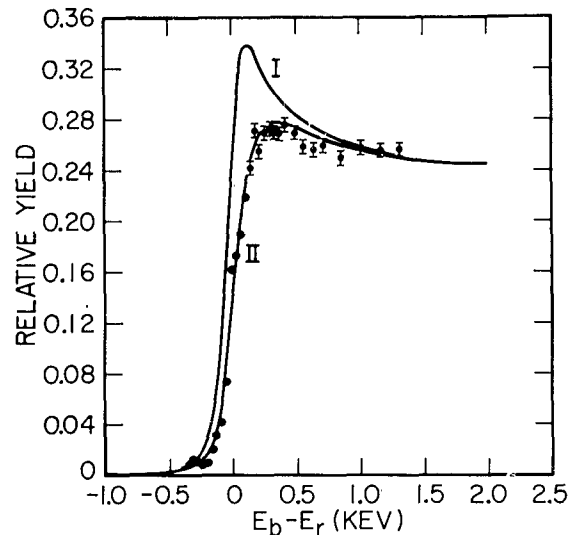


Fig. 14 - Theoretical yield curves and datum points for a thick aluminum target,  $H_1^+$  beam-energy spread 0.01 percent, and 1317-keV resonance. Curve I represents a pure aluminum target, and curve II represents a target with a 340-eV layer of  $Al_2O_3$  on its surface. Note that the midpoint of the rise of I is about 60 eV below resonance energy, but the midpoint of the rise of II, corresponding more closely to experiment, is almost exactly at resonance energy.

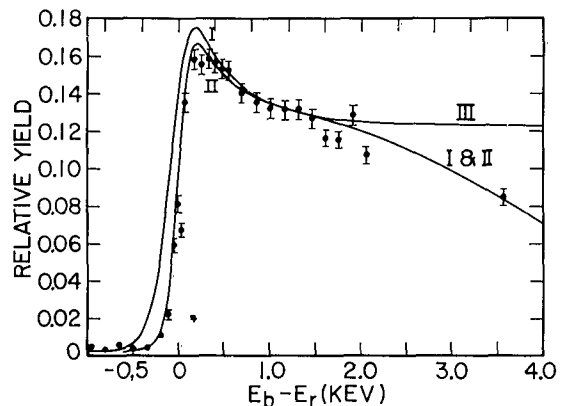


Fig. 15 - Theoretical yield curves and datum points for a 5-keV  $Ni^{58}$  target,  $H_1^+$  beam-energy spread 0.02 percent, and 1843-keV resonance. Curve I represents a pure nickel target. Curve II represents a pure nickel target coated with a 60-eV layer of  $C^{12}$ . Curve III is based on a 10-keV target and is shown to indicate the plateau height of a truly thick target. Note how far the peak is from  $E_r + t/2$ ! Note also how enhanced the hump is compared to the aluminum target humps.

target. Thus the 5.3-keV target, which would ordinarily have been expected to show evidences of being thick, does not do so.

The difference between the relative heights of the experimental humps for the 992-keV and the 1843-keV resonances is due mainly to the lesser contamination of the Ni<sup>58</sup> target because of its lower chemical activity, the apparent smaller width  $\Gamma$  of the Ni<sup>58</sup> resonance, and the higher stopping power of nickel. The theoretical hump height for the 992-keV resonance, based on a beam-energy resolution of 0.02 percent and a  $\Gamma$  value of 100 eV, is 24 percent of the plateau height, while for the Ni<sup>58</sup> resonance, a beam-energy resolution of 0.02 percent, and a  $\Gamma$  value of 50 eV, the theoretical hump height is 41 percent.

#### Further Considerations

Target Nonuniformities - Because of the possibility that target nonuniformities and other target irregularities distorted the shapes of the experimental yield curves, various precautions were taken to make the targets as nearly perfect as possible. Many of these procedures have been described. As a final check, an estimate of the effect of target thickness nonuniformities was made by the use of a special computer program. In this program, the Breit-Wigner expression for the cross section was assumed to be a  $\delta$  function, and the target thickness was treated as a variable in the following manner. The interface between the aluminum target and copper backing was assumed to be diffused such that the transition from aluminum to copper was gradual, the fraction of copper  $f$  being expressed by the integral of a Gaussian distribution as follows:

$$f = \frac{1}{\sqrt{2\pi} \Delta} \int_0^t e^{-(x-t)^2/2\Delta^2} dx,$$

where  $t$  is the nominal, or average, target thickness,  $x$  is the depth in the target mixture, and  $\Delta$  (the standard deviation) is a chosen fraction of  $t$ .

It is reasonable to expect that the largest percentage thickness variations would occur with the thinnest target E-7, for which we estimated  $\Delta$  to be  $0.2t$  at most. Two yield curves were then calculated with the special program; in one,  $\Delta$  was put equal to  $0.2t$ ; and in the other,  $\Delta$  was put equal to zero (corresponding to a sharp boundary), with appropriate program adjustments. The two yield curves were indistinguishable from one another when plotted on standard notebook-size graph paper except in the immediate vicinity of the peak, where the deviation was observable but small. This result, which might at first appear surprising, is due to the fact that the yield-curve asymmetry caused by fluctuations in energy loss obscures any asymmetry caused by target thickness nonuniformities of the order assumed. However, it should be emphasized at this point that much larger target-thickness nonuniformities could have been present if we had not used extreme care in target preparation.

Aluminum Target Oxidation - In order to make satisfactory comparison with the seven E-series targets, it was necessary to assume varying degrees of oxidation of the aluminum, from full oxidation of the thinnest target to relatively small oxidation of the thickest. It is known that not exposing evaporated aluminum to air is no guarantee that the aluminum is not oxidized. A posteriori it is possible to advance arguments as to why varying oxidation would occur in the targets all of which were prepared simultaneously. Of the several arguments that could be used, two are now presented. (1) The thinner targets were farther from the source of evaporating aluminum than the thicker targets. Thus the thinner targets were farther from the liquid-aluminum "oxygen sink"; and the spatial density of the aluminum-vapor oxygen sink was considerably less near the thinner targets. (2) There was more time between deposition of successive layers for

the thinner targets. Thus each layer of the thinner targets was exposed to oxygen in the vacuum system for a longer time than for the thicker targets.

#### APPLICATION TO RESONANCE-ENERGY DETERMINATION WITH THE $H_1^+$ BEAM

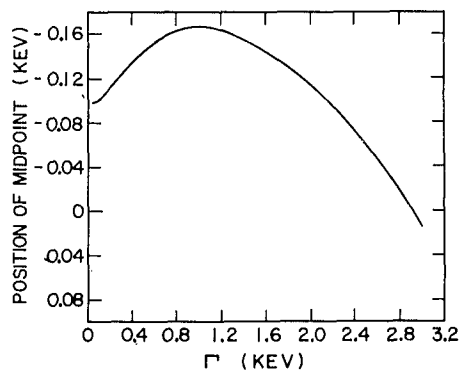
Figure 9 shows one possible source of error in measuring resonance energies with thin targets: that if a correction of half the target thickness is applied to the peak of the yield curve for target E-4 (thickness 2.2 keV) in order to obtain the resonance energy, an error of about 700 eV is introduced into the resonance energy determination because the actual experimental peak is displaced only about 400 eV from resonance energy.

Figure 13 shows a possible source of error in measuring resonance energies with thick targets: that the midpoint of the rise of a pure aluminum thick-target curve for the 992-keV resonance is about 100 eV below the true resonance energy. The amount of this displacement of the midpoint of the rise from  $E_r$  is dependent upon  $\Gamma$ ,  $E_r$ , beam-energy inhomogeneity, target thickness, target stopping power, and target cleanliness and purity. In order to illustrate the way in which this displacement varies with  $\Gamma$ , we have computed the amount of the displacement as a function of  $\Gamma$  with the following conditions: target E-2 (about 9 keV thick and assumed to be pure aluminum), 992-keV resonance, and a beam-energy resolution of 0.02 percent. Figure 16 shows the resulting curve. Observe that there is a particular value of  $\Gamma$  (about 1 keV) leading to a maximum displacement. The drop in the curve at values greater than  $\Gamma = 1.0$  keV is somewhat faster than if a thicker target had been used in the calculation; i.e., a 9-keV-thick target is too thin for a good determination of the thick-target yield-curve shape for resonance widths greater than about 1 keV.

The considerations presented in the preceding two paragraphs indicate that the most accurate method for determining the resonance energy of a very narrow resonance is to use neither of the above procedures but to calculate the yield curve as described herein and to compare this calculated curve with the experimental curve.

For each target of the E series, the calculated curve showing the best agreement with the data, Figs. 6 to 12, was used to determine  $E_r$ . Visual adjustment of the abscissae of the experimental and calculated curves provided the means of choosing a value of  $E_r$  for that particular target. In this way, the maximum degree of judgment was exercised on the conditions of target purity and other factors influencing the experimental data. The arithmetic average of the seven values is  $991.91 \pm 0.30$  keV. The uncertainty given here is the absolute uncertainty in the energy determination and is found by calculating the square root of the sum of the squares of the individual uncertainties of the various parameters related to the separate components of the electrostatic analyzer (6).

Fig. 16 - Displacement ( $E_b$  at midpoint minus  $E_r$ ) of the midpoint of the rise of a thick-target yield curve as a function of  $\Gamma$ . The assumed parameters are a 9-keV pure aluminum target,  $E_r = 992$  keV, and an  $H_1^+$  beam-energy spread of 0.02 percent. Note that the displacement is not a monotonic function of  $\Gamma$ .



The data of target E-1 from the present series of experiments are the same data that were included in a previous communication (22) reporting the  $T^3(p,n)He^3$  threshold-energy measurement. In that paper, the value of the bombarding energy at the midpoint of the rise of the thick-target step was reported to be 992.0 keV. This value was rounded up from 991.95 keV. It should be emphasized that the data reported herein, and illustrated in Fig. 12, are the same data as previously reported and that the bombarding energy at the midpoint of the rise for target E-1 is still reported as 991.95 keV. It so happens that the effect of impurity for target E-1 exactly canceled within the precision of the measurements the effect due to fluctuations in energy loss, and therefore the value of  $E_r$  for target E-1 is the same as the energy at the midpoint of the rise, 991.95 keV. So there is no change in our energy calibration subsequent to the  $T^3(p,n)He^3$  threshold-energy measurement. The calculated curves for targets E-2 through E-7 were not available at the time of submission of the manuscript of the  $T^3(p,n)He^3$  experiment.

We feel justified in assigning equal weight to each of the seven measurements because we have confidence in the method used to compare the data with the calculations. We therefore take the value of  $991.91 \pm 0.30$  keV to be our best value of the intrinsic resonance energy  $E_r$ .

Best values have been obtained in the same manner for the other resonances discussed herein. These other values are based on thick-target data only. See Table 1 for a listing of these best values.

Table 1

Best Values of Absolute Resonance Energies for a Number of Narrow  $(p, \gamma)$  Resonances. These values were obtained by the fitting of theoretical yield curves for each resonance to the experimental data, and therefore include a judicious choice for quantities usually ignored, such as the degree of oxidation of the target and the presence of an inert contaminating layer over the target as well as fluctuations in energy loss. The uncertainties are in the absolute values.

| Reaction                    | Resonance Energy (keV) |
|-----------------------------|------------------------|
| $Al^{27}(p, \gamma)Si^{28}$ | $991.91 \pm 0.30$      |
| $Al^{27}(p, \gamma)Si^{28}$ | $1317.19 \pm 0.40$     |
| $C^{13}(p, \gamma)N^{14}$   | $1747.06 \pm 0.53$     |
| $Ni^{58}(p, \gamma)Cu^{59}$ | $1423.64 \pm 0.43$     |
| $Ni^{58}(p, \gamma)Cu^{59}$ | $1843.45 \pm 0.56$     |

## RESULTS WITH THE $H_2^+$ BEAM

For most of the measurements with the  $H_2^+$  beam and the electrostatic analyzer, the analyzer was set to give a beam-energy spread of 0.02 percent.

### Displacement

As mentioned previously, the series of experiments reported herein was originally initiated by the observation that the midpoint of the rise of the hydrogen-molecular-ion-beam thick-target yield curve occurred at an energy about 0.05 percent lower than anticipated from the electrostatic analyzer readings for the same resonance observed with

the proton beam. An apparent discrepancy of this magnitude was considered to be important because we had measured the absolute calibration parameters of the electrostatic analyzer with great precision. These parameters are the terms appearing in the absolute calibration equation (Ref. 6) which is

$$eV_0 = V_p(e/k)(r_a/2d)(1+\gamma)(1+\epsilon_{int})(1+\epsilon_{ext})(1-nm_e/M_t), \quad (4)$$

where  $eV_0$  is the energy of each proton incident on the target,  $k$  is the number of protons in the analyzed particle,  $V_p$  is the total voltage on the deflecting plates of the analyzer,  $d$  is the plate separation, and  $r_a$  is the arithmetic mean radius of curvature of the plates. The quantity  $(1+\gamma)$  is the relativistic correction factor. The quantities  $(1+\epsilon_{int})$  and  $(1+\epsilon_{ext})$  are correction factors arising from the internal (in the region of the gap) magnetic field and the external (between the input gnatios and collimating gnatios) magnetic field, respectively. The terms  $\epsilon_{int}$  and  $\epsilon_{ext}$  are inversely proportional to  $\sqrt{M_t V_0}$ , where  $M_t$  is the rest mass of the analyzed particle. The quantity  $n$  is the number of electrons in the analyzed particle, and the correction term for the energy carried by these electrons is  $(1 - nm_e/M_t)$ . All of the above correction factors are the same order of magnitude as the apparent discrepancy, several hundredths of a percent; hence each correction factor must be determined carefully.

A re-examination of the parameters in Eq. (4) did not reveal a source of nonlinearity in the electrostatic analyzer; however, there are many other experimental factors or conditions which could conceivably influence the apparent value of the resonance energy. Therefore all of the following possible contributing effects were considered and shown either by calculation or by experiment not to be responsible for the discrepancy.

1. Actual energy shift due to the Doppler broadening arising from the internal vibrational energy of the  $H_2^+$  molecules.
2. Difference in the electric field experienced by the two different protons of the hydrogen molecular ion because of their finite separation in the molecule.
3. Possible breakup of the  $H_2^+$  beam inside the electrostatic analyzer.
4. Backscattered beam passing through the target twice.
5. Beam-current integration abnormalities.
6. Accumulation of electric charges (and potential) on the target.
7. Contaminating film on the surface of the target.
8. Partial or complete oxidation of the target.
9. Angular distribution of the gamma rays.
10. Abnormalities in the gamma-ray detection equipment.
11. Fringing electrostatic fields.
12. Nonuniformities in the electric field between the analyzer deflecting plates.
13. Deformation of the analyzer deflecting plates due to the electrostatic force between them.
14. Malfunctions in the analyzer power supply and voltage measuring equipment, such as nonlinearities in the potentiometer and resistor stack, dirty slide-wire contacts,

temperature changes in the resistor stack and elsewhere, thermoelectric contact potential differences within the measuring circuit, instabilities of the standard cell and working cell, and unbalance between the plus and minus voltages on the two deflecting plates.

15. Accumulation of an insulating layer on the inner wall of the drift tube between the input gnathos and the collimating gnathos of the electrostatic analyzer, and hence an accumulation of polarized electric charge on this wall with consequent beam deflection.

16. Accumulation of electric charges (and potential) on the analyzer deflecting plates because of the presence of insulating layers.

The relative motion of the protons in the hydrogen molecular ion, item 1, causes the effective relative velocity between each incoming proton and target nucleus to be  $\mathbf{v}_e = \mathbf{v}_b + \mathbf{v}'$ , where  $\mathbf{v}_b$  and  $\mathbf{v}'$  are the respective velocities of the  $\text{H}_2^+$  molecule in the laboratory system and the proton in the  $\text{H}_2^+$  molecule center-of-mass system. The limiting cases are, then,  $E$  (effective) =  $Mv_e^2/2 = M(\mathbf{v}_b \pm \mathbf{v}')^2/2 = M(v_b^2 \pm 2v_b v' + v'^2)/2$ . The middle term in the expansion does not affect the average effective energy, because for each positive value, there is an equal negative value. The final term, however, is always positive, and therefore does increase the average value with Doppler broadening above that without Doppler broadening. However, when one inserts realistic values for internal molecular velocities, this increase in average effective bombarding energy is the order of a few eV and therefore cannot account for the observed apparent energy displacement (about 1000 eV) of the midpoint of the thick-target  $\text{H}_2^+$  beam yield curve.

The deformation force, item 13, was not expected to be significant because it was calculated to be very small. However, the effect was tested with the use of a special capacity-measuring circuit. The two analyzer deflecting plates were connected to an oscillator tank circuit in which they served as a capacitor. The frequency was then measured (by zero beating) with the plate high voltage first on and then off the plates. No change in capacity was observed. The sensitivity of the method is estimated to be such that a change of 0.01 percent in plate spacing could have been detected.

The National Bureau of Standards checked the potentiometer and resistor stack for nonlinearity and checked the standard cell, potentiometer, and resistor stack for absolute calibration (item 14).

Item 15 was conceived as the possible result of gas molecules being ionized in the drift-tube space between the input gnathos and collimating gnathos of the electrostatic analyzer and then depositing onto insulating layers on the drift-tube walls. The earth's magnetic field could serve as a charge polarizer, deflecting positive ions to one side and negative ions to the other. To test this possibility, an external magnetic field was superimposed on this drift-tube space such that the net normal magnetic field was reversed. No effect due to the accumulation of charge on the walls of the drift space was observed on the electrostatic analyzer calibration.

Accumulation of electric charges on insulating layers covering the deflecting plates (item 16) could introduce a nonlinearity as well as an absolute error in the energy calibration of the analyzer. The expected polarity of this charge is such that the energy value observed would be higher than that which would be obtained without the spurious charge. If the spurious charge were a constant, independent of applied voltage, then the energy values obtained would have less percentage error as the applied voltage is increased. Thus the energy calibration for the  $\text{H}_2^+$  beam would give a result which would be too low relative to the  $\text{H}_1^+$  beam calibration. Consequently, the possible effects due to the accumulation of electric charges were considered to be very serious both with respect to the absolute calibration of the electrostatic analyzer and with respect to the evaluation of the  $\text{H}_2^+$  beam anomalies. In connection with the measurement of absolute bombarding energies of certain reaction thresholds and resonances, we observed that such an

accumulation of charges did indeed occur. Therefore a detailed program was undertaken to study the nature of the effect.

Definitive evidence for the effect of charge accumulation first appeared during preliminary measurements on the  $T^3(p,n)He^3$  threshold-energy determination (22). (The final results reported in Ref. 22 were not influenced by the charge-accumulation effect.)

The manner in which the effect was manifested is as follows. At any time following a period of several hours during which no beam was passed through the electrostatic analyzer a measurement of the  $T^3(p,n)He^3$  threshold energy would give a result which we shall call  $E_{th}$ . Repeating the measurement continuously would give a series of results each higher than the previous one until, after about 2 hours, there would be no further increase. The measured threshold energy would return to  $E_{th}$  after a waiting period of several hours for the charge to leak off or after the introduction of nitrogen gas at low pressure followed by an ac glow discharge between the deflecting plates. The maximum increase of the measured threshold energy above  $E_{th}$  was 0.04 percent. For the  $T^3(p,n)He^3$  threshold energy this increase requires the equivalent of a uniform charge accumulation on each deflecting plate corresponding to 2 volts. However, under the assumption of a uniform charge accumulation it is not possible to account for the long time constant of the drift. A simple calculation can be made to determine approximately the time constant from the known pressure in the analyzer ( $5 \times 10^{-6}$  torr), the approximate beam current ( $10^{-7}$  amp), and the following assumptions. (1) All ion pairs created by collisions between the incoming beam and residual gas are collected on the surfaces of the deflecting plates exposed to the beam. (2) No secondary electron emission occurs. (3) Ohm's law is applicable to the insulating layers.

The result is that the time constant should have been about 1 second. Under the assumption that the principal contribution to the drift came from highly localized insulating areas, it is possible to account for the long time constant provided that the resistivity of the deposited material is about  $10^{17}$  ohm-cm. Some resins have a resistivity of about this amount. When the analyzer was opened and one of the deflecting plates removed, two areas of a few square centimeters each of a dark deposition were observed. One of these spots was near the input at a point where the beam would strike the outer plate if no voltage were applied to the deflecting plate, and the other spot was near the output of the analyzer. A general light-colored deposition of material was observed covering the remaining portions of the deflecting plates in the vertical region occupied by the beam during normal operation. A fine abrasive was used to remove the hardened deposit, and the analyzer was reassembled and recalibrated. The result for the threshold energy was now within 0.01 percent of  $E_{th}$ , and there was no observable long-term drift. Furthermore, the ac gaseous glow discharge would cause no shift in calibration. Possible conclusions are (a) that the light-colored layer caused an error in calibration of as much as 0.01 percent, and probably this layer had a very short time constant for charge accumulation, and (b) that the larger error, 0.04 percent, and the long time constant were caused by the darker areas on the deflecting plates.

After the conclusion of the above investigation the midpoint of the rise of the  $H_2^+$  beam thick-target (p,  $\gamma$ ) yield curve was still observed to be 0.05 percent lower than that predicted from the  $H_1^+$  beam result.

#### Thin Targets

Even after the aforementioned considerations and checks, it was still not certain that the displacement was not due to some unconsidered aspect of the instrumentation. As a further check the resonance energy was determined with extremely thin targets. It was expected that if we had properly considered all significant aspects of the instrumentation, the peak of the thin-target  $H_2^+$  beam yield curve would occur at the position predicted from the  $H_1^+$  beam result. Indeed this check did result in agreement between the  $H_1^+$  and  $H_2^+$  beam observed thin-target peaks within an uncertainty of about 0.01 percent! Thus the

linearity of the instrument and technique were established beyond question, and the apparent displacement of the midpoint of the rise of the  $H_2^+$  beam thick-target yield curve from resonance energy has therefore been shown to be a real effect in nature.

#### Other Anomalies

The family of curves shown in Fig. 17 was obtained from the E-series family of targets and the  $H_2^+$  beam at the 992-keV resonance. The method of presenting the data here is the same as that used for presenting the data of Fig. 1. Inspection of these curves reveals four additional anomalies. (1) The peaks of the thin-target yield curves are not displaced from each other by an amount as great as might have been previously expected. (2) Even the thick target has a peak, or hump, near resonance energy. (3) The thick-target curve shows a definite asymmetry about the midpoint of its rise. (4) The "thick-target plateau" for target E-1 is not really a plateau but a secondary slow rise.

Some of these anomalies appear to be similar to some of those observed with the  $H_1^+$  beam. However, as will appear evident later, the explanations are quite different.

During the course of the experiments, a number of models were invented in attempts to explain the anomalies of Fig. 17. For each model further experiments were devised

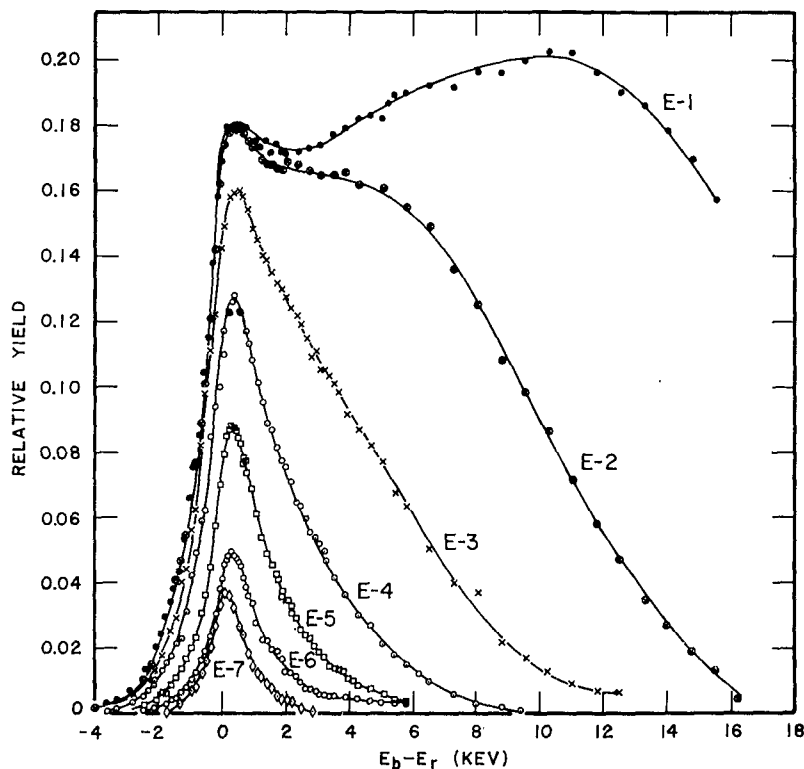


Fig. 17 - Experimental yield curves of the E-series aluminum targets,  $H_2^+$  beam, and 992-keV resonance. The abscissa energies have been converted to the  $H_1^+$  energy scale. Refer to the caption of Fig. 1 for the target thicknesses.

specifically to test the validity of a crucial feature of that particular model. In most cases the model failed to pass the test, but these further experiments led to additional information concerning the behavior of  $H_2^+$  beams.

### Inert Coatings

One series of tests involved the coating of the targets by thin layers of inert material, chosen to be copper. The main purpose of this series of tests was to determine the effective stopping power of the target material for the  $H_2^+$  beam. There were four possible ways in which the beam particles could lose energy in the target: as mass-2 particles with one charge, as mass-2 particles with two charges, as two mass-1 particles, each with one charge, and as one mass-1 particle with one charge and another mass-1 particle with no charge. In addition to the stopping-power determination, results with the coated targets also indicated new discrepancies which contributed to an understanding of the behavior of the  $H_2^+$  beam in targets.

In one set of experiments one particular thick target was first used to obtain the usual  $H_1^+$  and  $H_2^+$  beam yield curves over the region of the 992-keV resonance. Then a thin layer of copper was evaporated over the layer of aluminum, and another pair of  $H_1^+$  and  $H_2^+$  beam yield curves was obtained. Then another thin layer of copper was evaporated onto the same target, and another pair of yield curves was obtained. The differential displacements of the midpoint of the rise due to first one — then both — copper layers, referred to the  $H_1^+$  energy scale, are shown in Table 2. We do not assign any special

Table 2

Results of Experiments with Copper Coatings on Both Thick and Thin Aluminum Targets with Both  $H_1^+$  and  $H_2^+$  Beams. All energies ( $H_1^+$  and  $H_2^+$ ) are given in terms of the  $H_1^+$  energy scale. The displacement for the thick target refers to the displacement of the midpoint of the rise (used for convenience only), and for thin targets it refers to the displacement of the peak. The uncoated targets are used for reference purposes and therefore have zero displacement by definition. The width for the thick target refers to the interquartile interval of the rise (used for convenience only), and for the thin targets it refers to the full width at half height of the resonance peak. The thick target, C-36, was about 20 keV thick. The thin-target thicknesses are indicated by the  $H_1^+$  beam uncoated-target width. Target C-61 was slightly thicker than target C-64. Target F-8 was approximately the same thickness as target F-10. The Consistent Width column gives the expected widths for the  $H_2^+$  beam resonance curves based on the fluctuations in energy loss for the  $H_1^+$  beam and the assumption in the text that all widths involved may be combined as independent Gaussian distributions. Uncertainties are difficult to assign, but are estimated to be in the range of 30 to 50 eV for the lowest numbers and 100 to 150 eV for the highest numbers.

| Targets           | $H_1^+$ Beam               |                     | $H_2^+$ Beam               |                     |                       |
|-------------------|----------------------------|---------------------|----------------------------|---------------------|-----------------------|
|                   | Observed Displacement (eV) | Observed Width (eV) | Observed Displacement (eV) | Observed Width (eV) | Consistent Width (eV) |
| Thick             |                            |                     |                            |                     |                       |
| Uncoated (C-36)   | 0                          | 270                 | 0                          | 1200                | 1200                  |
| First Coat (C-36) | 870                        | 700                 | 900                        | 1950                | 1360                  |
| Both Coats (C-36) | 1710                       | 1160                | 2020                       | 2780                | 1650                  |
| Thin              |                            |                     |                            |                     |                       |
| Uncoated (C-64)   | 0                          | 510                 | 0                          | 1140                | 1140                  |
| Coated (C-61)     | 290                        | 830                 | 320                        | 1650                | 1310                  |
| Uncoated (F-10)   | 0                          | 320                 | 0                          | 920                 | 920                   |
| Coated (F-8)      | 2160                       | 1650                | 2620                       | 3180                | 1860                  |

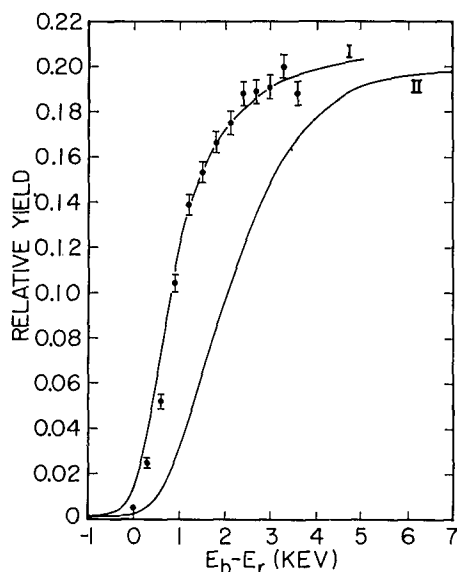


Fig. 18 - Theoretical yield curves and datum points for thick aluminum target (C-36, 20 keV) coated with a layer of copper,  $H_1^+$  beam-energy spread 0.02 percent, and 992-keV resonance. Curve I represents a layer of copper 1100 eV thick, and curve II represents a layer of copper 2200 eV thick.

physical significance to the midpoint of the rise of the  $H_2^+$  beam thick-target yield curve. We use it to measure the displacement only because it is convenient to do so.

Figure 18 shows the  $H_1^+$  beam datum points obtained after the first copper evaporation (target C-36), illustrating the displacement of the midpoint of the experimental rise to be about 870 eV from resonance energy. Using Eq. (1) and introducing an inert surface layer, we computed several theoretical yield curves for different assumed thicknesses of copper on the surface. Curve I of Fig. 18 gave the best fit to the data and represents an assumed layer thickness of 1100 eV (average energy loss). The fact that this assumed thickness, 1100 eV, is significantly greater than the observed  $H_1^+$  beam midpoint displacement due to the inert layer, 870 eV, is reasonable considering the results and discussions presented in the  $H_1^+$  beam sections. Another curve (II) was computed for a layer of copper 2200-eV thick. This curve does not correspond to any of the experimental situations listed here, but is included for illustration only. In this case the amount of the displacement of the midpoint by the inert layer was about the same as the layer thickness, illustrating that for a layer this thick the midpoint displacement is about the same as the average energy loss.

If the two protons in the  $H_2^+$  molecule lose energy in the same way as two independent—and separately spaced—protons, the energy losses, if referred to the same energy scale, would be equal for the two different beams. The  $H_2^+$  beam yield-curve displacement for the first layer, 900 eV, is about the same as that for the  $H_1^+$  beam yield curve, 870 eV, within experimental uncertainties (see Table 2). However, for the combined copper layers, the apparent energy loss suffered by the  $H_2^+$  beam in traversing the layers is significantly greater than for the  $H_1^+$  beam.

It is also interesting to compare the experimental resonance widths for the several different cases. Here the term "width" for the thick targets is used to represent the interquartile interval. (We do not assign any special significance to this interquartile interval. It is, however, a convenient quantity for comparison purposes.) For the  $H_1^+$  beam and the copper coatings discussed above, the widths are 270, 700, and 1160 eV as listed in Table 2. For the  $H_2^+$  beam, they are 1200, 1950, and 2780 eV. In order to compare these two sets of experimental results, we made the following calculations. We assumed that (a) the  $H_1^+$  beam uncoated-target yield curve (width, 270 eV), (b) the  $H_1^+$  beam coated-target yield curve (width, 700 eV), and (c) the increase in  $H_1^+$  beam-energy inhomogeneity caused by the fluctuations in energy loss in penetrating the coating can each be represented by the integral of a Gaussian shape. Then curves (a) and (c) should "add" to give (b), following the rule that the combined effect of two independent Gaussian distributions gives a distribution whose width is the square root of the sum of the squares of the widths of the individual distributions. Conversely, one should be able to find the width of (c) by "subtracting" (a) from (b). This calculation yields a width of 650 eV for the increase in  $H_1^+$  beam-energy inhomogeneity in the coating. Then, if one further assumes that the  $H_2^+$  molecule behaves like two widely separated protons, one should be able to predict the width of the  $H_2^+$  beam coated-target yield curve (referred to the  $H_1^+$

energy scale) by "adding" the  $H_2^+$  beam uncoated-target yield curve width (1200 eV) to the value of 650 eV obtained from the  $H_1^+$  data. The result of this operation, 1360 eV, is defined as the "consistent width" of the  $H_2^+$  beam yield curve, and is listed in Table 2. Clearly the observed width of 1950 eV is much too large to be explained by this model. If one performs the same set of calculations on the data for the combined copper coatings, one finds a consistent width of 1650 eV for the  $H_2^+$  beam yield curve, based on a width of 1160 eV for the  $H_1^+$  beam yield curve. Again, the observed width of 2780 eV is much too large. Thus it appears that the fluctuations in energy loss suffered by the  $H_2^+$  beam in traversing the copper coatings are also much greater than for the  $H_1^+$  beam.

Two different thin targets of the same thickness, C-64 and C-61, were used for a somewhat similar set of experiments, except that a layer of copper was evaporated only onto target C-61. These results are also listed in Table 2. The coated-target energy shift was 290 eV for the  $H_1^+$  beam and 320 eV (referred to the  $H_1^+$  scale) for the  $H_2^+$  beam. As with the first coating over the thick target, C-36, the displacements for the two different beams are about the same within experimental uncertainties. Note, however, that the width (here the term "width" refers to the full width of the thin-target resonance peak at half height) of the  $H_2^+$  beam yield curve for the coated target is greater than expected from the width measurements with the  $H_1^+$  beam, 1650 eV compared with 1310 eV for the consistent width.

Another pair of thin targets, F-10 and F-8 (thinner than the previous ones), was used for a similar set of measurements. This time, a thicker layer of copper was evaporated. The energy displacement of the  $H_2^+$  beam, 2620 eV, is significantly greater than that for the  $H_1^+$  beam, 2160 eV. And again, as in every previous case, the increased width of the resonance peak is much greater for the  $H_2^+$  beam, 3180 eV compared with a consistent width of 1860 eV.

Figure 19 illustrates the calculated  $H_1^+$  beam yield curve for a thin aluminum target with a thin copper coating. The datum points are from a target, C-16, which is a member of another family of targets similar to the E series. This particular set of data was chosen because target C-16 had very nearly the same amount of aluminum as did target E-7, and calculations had already been made for target E-7. Several curves were computed for different assumed thicknesses of copper. The curve shown in Fig. 19 represents a copper coating of 1100 eV. Comparison of the data and the calculated curve was done in a manner identical to that described in the  $H_1^+$  beam sections. Note the similarity of shapes of the yield curves found from the data and from the calculation.

When the above series of measurements was made, the increased broadening, or width, of the  $H_2^+$  beam yield curves was very disturbing, but as will appear evident later, it can be satisfactorily explained. The increased displacement for the  $H_2^+$  beam yield curves can also be explained.

The results of the copper coating experiments may be summarized as follows. (1) The coatings cause a shift in energy of the resonance peaks and midpoints. (2) For the thinner coatings, the  $H_1^+$  and  $H_2^+$  beam yield curves are shifted in energy about equal amounts (both beams referred to the  $H_1^+$  energy scale). (3) For the thicker coatings, the  $H_2^+$  beam yield curves

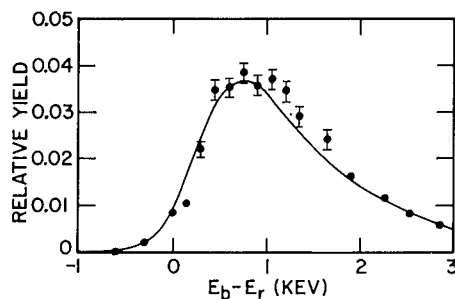


Fig. 19 - Theoretical yield curve and datum points for a thin aluminum target (C-16, about 0.3 keV) coated with a layer of copper,  $H_1^+$  beam-energy spread 0.02 percent, and 992-keV resonance. The computed curve was obtained under the assumption of an 1100-eV layer of copper.

are shifted in energy relatively more than the  $H_1^+$  beam yield curves. (4) The apparent fluctuations in energy losses of the  $H_2^+$  beam in penetrating the inert coating are relatively much greater than those for the  $H_1^+$  beam. This effect applies to both thin and thick coatings, but is more pronounced for thick coatings. (5) The thinner inert coatings cause the  $H_2^+$  beam thick-target yield curve to be less steep during the upper half of the rise (and therefore more nearly symmetric), and the thicker inert coatings cause this effect to be so pronounced that the step rise becomes asymmetric in the opposite way from the original uncoated shape.

#### $H_1^+$ and $H_1^0$ Beams from the $H_2^+$ Beam

Further efforts to gain an understanding of the behavior of  $H_2^+$  beams led to the use of a gas cell for stripping the  $H_2^+$  beam into a neutral  $H_1^0$  component and an  $H_1^+$  component, referred to hereinafter by the symbol  $H_1^+_s$ . Both He and  $N_2$  were used (at different times) as the stripping gas. The cell, 10 cm long, had diaphragms at each end for beam passage. The entrance aperture was 5 mm long with a diameter of 1 mm; the exit aperture was 20 mm long with a diameter of 2 mm. The system was differentially pumped. A typical cell pressure was about  $10^{-2}$  torr.

A magnetron magnet was used to separate the various components of the beam:  $H_1^0$ ,  $H_1^+_s$ , and residual  $H_2^+$ . Conventional current-integrator techniques were used to measure the amount of the  $H_1^+_s$  beam, but a special procedure was required for the  $H_1^0$  beam. The amount of  $H_1^0$  beam was determined as a function of gas-cell pressure by means of a quartz plate on which the  $H_1^0$  beam impinged, and a 3/4-inch-diameter multiplier phototube was used to measure the amount of fluorescence produced by the beam. The phototube current was calibrated in terms of effective "beam current" by a comparison of the phototube readings for the  $H_1^+_s$  beam and the usual current-integrator readings for the same beam.

The amount of  $H_1^0$  beam as a function of gas-cell pressure is shown in Fig. 20 for  $N_2$ . It is seen that the amount of  $H_1^0$  beam increases with cell pressure up to a value of 10 to  $12 \times 10^{-3}$  torr, beyond which the  $H_1^0$  beam intensity diminishes. This decrease at higher pressures is apparently due to the stripping of the  $H_1^0$  atoms by additional interactions with the extra gas.

For the measurement of the effective  $H_1^0$  "beam current" on target during the time data were being recorded, a positive voltage was impressed on the cold tube near the target surface to attract secondary electrons. It was this secondary electron current which was measured and integrated.

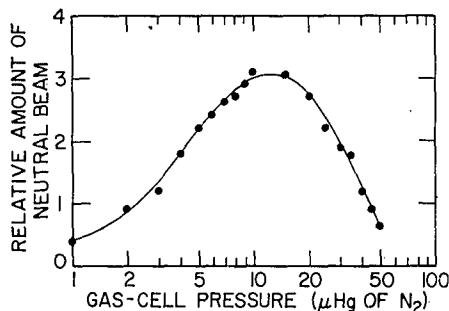


Fig. 20 - Relative amount of  $H_1^0$  (neutral) beam from the gas stripping cell as a function of gas-cell pressure. Note the logarithmic scale on the abscissa.

The  $H_1^0$  and  $H_1^+_s$  beam intensities were more limited than those of the unmodified hydrogen molecular ion beam, and factors such as counting rates and "signal-to-noise" ratios were consequently reduced for the  $H_1^0$  and  $H_1^+_s$  beams. Nevertheless, yield curves (not illustrated) were obtained with the use of the electrostatic analyzer. Because of the lack of statistical accuracy in these curves and because of extreme linearity, beam-energy precision, and resolution were not required for the measurements with the gas cell, additional yield curves, shown in Figs. 21 and 22, were obtained with the use of the magnetic beam-energy analyzer alone. These curves, involving higher beam

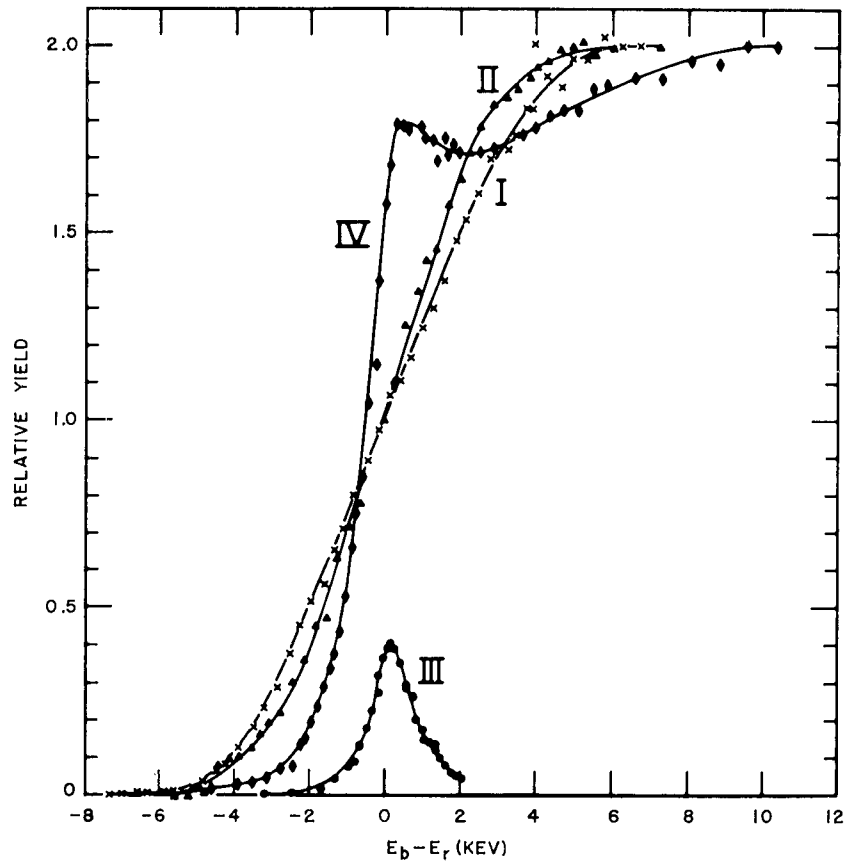


Fig. 21 - Experimental yield curves for thick aluminum targets, 992-keV resonance, and gas-stripped beams. Curve I,  $H_1^+$  beam. Curve II,  $H_1^0$  beam. Curve III,  $H_2^+$  beam, thin target. Curve IV,  $H_2^+$  beam, thick target. Curve III and IV are for comparison purposes. Note the symmetry of the stripped-beam curves and the lack of a displacement of the midpoint of the rise. Also note the fact that curve I is broader than curve II.

intensities, were similar in appearance to those previously obtained with the use of the electrostatic analyzer, but were smoother because of smaller statistical fluctuations and relatively lower background. The data shown in Figs. 21 and 22 were obtained with a larger scintillation crystal, 5 in. diam x 4 in. instead of 3 in. diam x 3 in., to increase further the counting rate.

Figure 21 shows the yield curves for the stripped beams and thick targets, and also shows the  $H_2^+$  beam thin- and thick-target yield curves for comparison and calibration purposes. Figure 22 shows thin-target yield curves for the stripped beams and the  $H_2^+$  beam, the last being used again for comparison and calibration purposes.

There are several features of these curves worth particular note: (1) The midpoints of the rise for the thick-target  $H_1^+$  and  $H_1^0$  yield curves are not displaced from the true resonance energy (more than 0.01 percent). (2) Thick-target stripped-beam yield curves

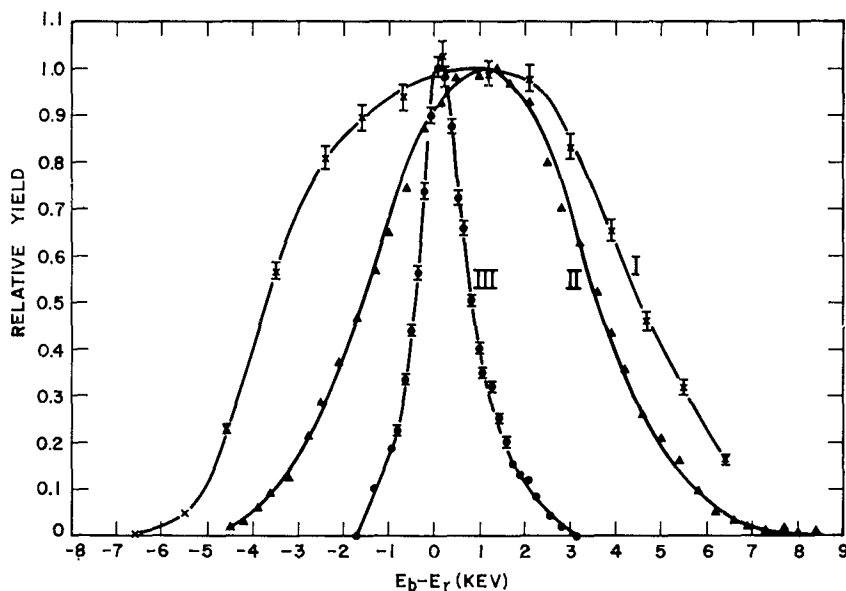


Fig. 22 - Experimental yield curves for thin aluminum targets, 992-keV resonance, and gas-stripped beams. Curve I,  $H_1^+$  beam (0.3-keV target). Curve II,  $H_1^0$  beam (1.4-keV target). Curve III,  $H_2^+$  beam (0.3-keV target). Note the reasonable symmetry of all the curves and that I is broader than II.

are symmetric about the resonance energy. (3) The stripped-beam yield curves have much larger widths than those for the direct  $H_2^+$  beam.

Thus we have apparently eliminated two discrepancies, the midpoint energy displacement and the asymmetry, but we have introduced another discrepancy! The average energy loss of the beam in penetrating the gas cell was only about 17 eV; thus this loss could not (according to previous concepts) possibly have introduced a distribution in energy loss with a full width at half maximum of 4 keV! Furthermore, ordinary energy losses are monotonic in that every bombarding ion either loses energy or remains unchanged in energy. There is no mechanism in energy-loss theory to account for a significant gain in energy by some of the ions. An inspection of Figs. 21 and 22 indicates that some protons gain energy while others lose.

Note that whereas in Fig. 21 (thick target) there was no displacement of the midpoint of the rise from resonance energy, the yield curves in Fig. 22 (thin targets) do show displacements of the peaks from resonance energy. These shifts can be explained as follows. Curve II, Fig. 22, represents the yield for the  $H_1^+$  beam impinging on target E-7 (0.3 keV if pure aluminum). Its peak is apparently displaced about 0.3 keV. If target E-7 is fully oxidized, as implied by Fig. 7, then its thickness is actually about 0.6 keV. Thus the peak of curve II appears to be displaced by about half the target thickness. We expect that either of the following conditions would lead to the peak of a yield curve being displaced by about half the target thickness: (a) broad resonance or (b) broad beam-energy distribution. Apparently, the beam-energy spread of the  $H_1^+$  beam (curve II) is sufficiently large to produce condition (b).

Curve I, Fig. 22, represents the yield for the  $H_1^0$  beam impinging on target F-5 (1.4 keV if pure aluminum). A thicker target was used for the  $H_1^0$  beam yield curve than for

the  $H_1^+$  beam yield curve because of the substantially lower intensity of the former beam. The peak of curve I is apparently displaced about 1 keV from resonance energy. If target F-5 were oxidized so as to have a total thickness of about 2 keV, then we would expect a shift of about 1 keV in the yield curve peak position based on condition (b) above.

The results with the stripped beams may be summarized as follows. (1) The mid-points of the rise of thick-target yield curves for both  $H_1^0$  and  $H_1^+$  beams occur precisely (within 0.01 percent) at resonance energy. (2) The thick-target yield curves for both the  $H_1^0$  and  $H_1^+$  beams are symmetric about resonance energy, and the thin-target yield curves for both these beams are approximately symmetric about the peak of the yield curve. (3) Both stripped beams,  $H_1^0$  and  $H_1^+$ , give much broader thick-target yield curves and wider thin-target yield curves than the unstripped  $H_2^+$  beam. (4) The  $H_1^+$  beam gives a somewhat wider resonance yield curve than the  $H_1^0$  beam.

The question naturally arises: Why is there a difference in beam-energy spread when the  $H_2^+$  beam penetrates the gas and when it penetrates a solid coating of comparable thickness? The answer to this question gives the key to the  $H_2^+$  beam anomalies and is found in the next section on the semiquantitative treatment of interactions involving the  $H_2^+$  molecule.

#### INTERPRETATION OF ANOMALIES WITH THE $H_2^+$ BEAM

A series of anomalies was observed for  $H_2^+$  beams somewhat similar to those observed with  $H_1^+$  beams, but some of them are peculiar to the hydrogen molecular ion (results with  $H_1^0$  and  $H_1^+$  beams and some of the results with coated targets). Because of the broadening of the effective beam-energy distribution by the internal motion of the protons, the discussion related to Fig. 17 leads one not to expect the explanations used for the  $H_1^+$  anomalies to apply equally well to  $H_2^+$  beams. Indeed the explanations derived below for the  $H_2^+$  beam anomalies are primarily of a quite different nature from those used for the  $H_1^+$  beam observations.

There were no displacement or asymmetry discrepancies when either thin targets or stripped beams were used. Thus these discrepancies are associated with the combination of the  $H_2^+$  beam and thick targets. The most important clue to the nature of the discrepancy was thus the time factor. When the  $H_2^+$  beam was stripped by the gas, the hydrogen molecular ion had approximately  $10^{-7}$  second to dissociate before the dissociation particles struck the target. However, inside the target, the  $H_2^+$  molecule had less than  $10^{-14}$  second before it (or the dissociation components) had lost enough energy to be of no interest in the yield at bombarding energies near the resonance energy. (A 1-MeV proton in aluminum loses energy at the rate of about  $600 \text{ eV}/10^{-15}$  second.) Therefore a basic re-examination of the fundamental processes involved in the breakup of the  $H_2^+$  molecule was undertaken and led to a satisfactory explanation as outlined below.

#### Nature of the $H_2^+$ Molecule

The  $H_2^+$  molecule is the simplest of the molecular structures and therefore has received extensive study. Teller (23), in 1930, derived the wave functions of the various electronic state configurations of the  $H_2^+$  molecule and calculated the potential-energy curves of these various states. Refinements of Teller's work were carried out by Bates et al. (24). Figure 23 shows potential-energy curves for a few of the electronic configurations of the  $H_2^+$  molecule. The  $1s\sigma_g$  state is the normal bound state (well depth = 2.8 eV) of the  $H_2^+$  molecule. Vibrational levels belonging to this ground electronic state have been calculated by Cohen et al. (25). Some of these vibrational eigenvalues for the  $J = 0$  (parahydrogen) state are illustrated in Fig. 23.

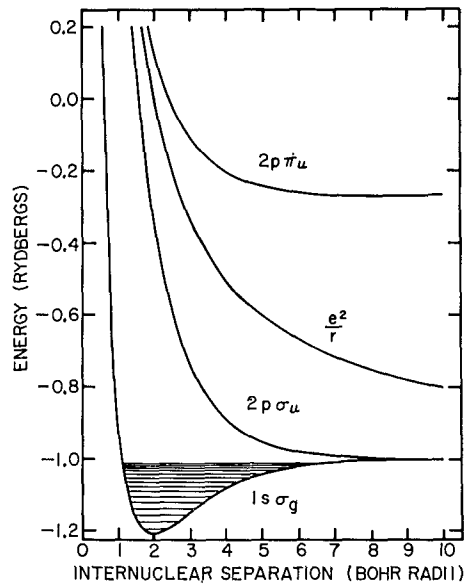


Fig. 23 - Potential-energy curves for various electronic configurations of the  $H_2^+$  molecule. The  $e^2/r$  curve, displaced one Rydberg, is for comparison purposes. Vibrational levels are illustrated for a parahydrogen molecule ion in the ground electronic configuration.

Now let us consider the mechanism of dissociation of the hydrogen molecular ion. Salpeter (26) has made approximate calculations for the dissociation of  $H_2^+$  molecules of a few MeV in collision with gas molecules. These estimates by Salpeter show that only about 1 percent of the dissociations of these  $H_2^+$  molecules in collision with hydrogen gas occur by excitation of the nuclear vibrations. (Dissociation by excitation of nuclear vibrations requires an energy transfer of about 2.8 eV.) The mechanism for dissociation of the other 99 percent of the  $H_2^+$  molecules is by excitation from the ground electronic state to one of the higher electronic state configurations of  $H_2^+$ . If we assume that the  $H_2^+$  molecule is in the lowest vibrational level of the ground electronic state, and if we also assume that in a collision the Franck-Condon principle will apply (i.e., the internuclear separation distance does not change during the collision and excitation to one of the higher electronic states), it can be seen from the potential-energy diagram that excitation to the lowest repulsive state ( $2p\sigma_u$  state) requires an energy transfer of about 11.8 eV. The  $H_2^+$  molecule thus excited will then dissociate into a free proton and a neutral hydrogen atom, following the potential "hill," with a total final separation kinetic energy of about 9.0 eV in the c.m. system. The next lowest state is the  $2p\pi_u$  state, and about 18.2 eV are required for excitation to this state. (This state is weakly bound

if excitation occurs at certain large internuclear distances, but for present purposes it may be regarded as a repulsive state.) For excitation to this state and all higher electronic states Salpeter points out that dissociation results in a free proton, a neutral hydrogen atom in an excited state, and some kinetic energy. An energy transfer of 30 eV (or more) is required for excitation to continuum states, which then result in two free protons and a free electron.

Calculations of the cross sections for the dissociation of  $H_2^+$  and  $D_2^+$  by a vacuum carbon arc have been made by Alsmiller (27), who shows that the principal modes of dissociation in the arc are by excitation from the ground state to the  $2p\sigma_u$  and the  $2p\pi_u$  states. Excitation to other states is essentially negligible. Other authors have investigated some aspects of the dissociation cross sections and angular distributions for the dissociation process.

The above discussion indicates the principal modes of dissociation of  $H_2^+$  molecules under circumstances different from those prevailing in the present experiments. Thus it is not known precisely what happens when the  $H_2^+$  molecules enter the target lattice; i.e., it is unknown what fraction of the  $H_2^+$  molecules are excited to each state or to the continuum.

If the electron is essentially removed instantaneously, each proton experiences an  $e/r^2$  Coulomb field from the presence of the other proton. The two protons would then separate as they go down an  $e^2/r$  potential "hill." This potential-energy curve is also shown in Fig. 23 for comparison purposes.

As will be seen subsequently, it is of interest to estimate the time required for dissociation. For excitation to the  $2p\sigma_u$  state, a semiclassical calculation shows that for 90 percent of the potential energy to be converted to kinetic energy a time of  $3.7 \times 10^{-15}$  second is required. If it is assumed that dissociation takes place by prompt removal of the electron so that the potential-energy function becomes  $E = e^2/r$ , then the time required for 90 percent of the potential energy to be converted to kinetic energy is  $17 \times 10^{-15}$  second.

Since the time required for 90-percent energy conversion for the proton and neutral hydrogen atom following excitation of the  $H_2^+$  molecule to the  $2p\sigma_u$  state is about the same as the time required for a proton to lose about 2.5 keV in the aluminum target, the time-factor clue mentioned above acquires added significance. Therefore a detailed examination of the effect of dissociation-component separation velocity on the effective energy distribution of the bombarding beam is warranted and is outlined below.

#### The Effect of Separation Velocity on the Energy Distribution

In the stripped-beam experiments with the gas cell, the dissociation components had more than adequate time to complete the dissociation process before striking the target ( $10^{-7}$  second compared with about  $10^{-14}$  second). Therefore each component had reached its final velocity  $v'$  (and energy  $E'$ ) in the c.m. system before it struck the target. If we assume for the moment that all other effects contributing to the widths of the  $H_1^+$  and the  $H_1^0$  beam yield curves are small compared with the relative dissociation velocity, a simple semiclassical picture of the broadening mechanism can be constructed.

Let the bombarding velocity of the  $H_2^+$  molecule in the laboratory system be  $v_b$ , and let the energy of each proton corresponding to this velocity be  $E_b$ . If  $\theta$  represents the angle between the directions of  $v_b$  and  $v'$ , the effective incident energy  $E_e$  may be written  $E_e = E_b + Mv_b v' \cos \theta + E'$ . Since  $v' \ll v_b$ ,  $E' \ll Mv_b v' \cos \theta$  in general. Therefore the deviation from nominal bombarding energy,  $\Delta E = E_e - E_b$ , is given essentially by the term  $Mv_b v' \cos \theta$ . Converting from velocity terms to energy terms, we obtain

$$\Delta E = 2\sqrt{E_b E'} \cos \theta. \quad (5)$$

If all spatial orientations of the internuclear axis are equally probable, then it can be shown that the probability for a deviation from nominal bombarding energy to be between  $\Delta E$  and  $\Delta E + d\Delta E$  is constant over the range  $-2\sqrt{E_b E'} \leq \Delta E \leq 2\sqrt{E_b E'}$  and is given by

$$P(\Delta E) d\Delta E = d\Delta E / 4\sqrt{E_b E'}. \quad (6)$$

This equation states that the effective energy distribution of the stripped beam striking the target is a simple rectangle as opposed to the approximate triangular output shape of the beam-energy analyzer. If the internal energy  $E'$  is 1 eV and if the bombarding energy  $E_b$  is 1 MeV, then the width of the rectangular distribution is 4 keV. A nominal value for the width of the triangular distribution is 0.2 keV for a bombarding energy of 1 MeV.

The equation given above for  $P(\Delta E)$  is strictly applicable only to those cases where all  $H_2^+$  molecules dissociate with the same amount of energy available to the separating components. This situation would exist only if (a) there were no initial vibrational or rotational energy in the molecule, (b) the initial internuclear separation distance were the same for all  $H_2^+$  molecules, and (c) the excitation of all the  $H_2^+$  molecules were to the same electronic configuration, e.g., the  $2p\sigma_u$  state. Despite these three limitations on the validity of Eq. (6), and also the limitation made by the assumption of the final (constant) separation velocity, Eq. (6) is a useful relationship for beginning the explanation of the gas-cell results. The second limitation is essentially removed in the subsequent calculation by the inclusion of the distribution of separation distances for a particular

vibrational level. And, of course, the assumption of final separation velocities for the gas-cell stripped-beam components is completely valid.

#### Interpretation of the Gas-Cell Results

An indication of the vibrational level (or levels) occupied by the  $H_2^+$  molecules in the bombarding beam can be found from the  $H_1^0$  thick-target yield curve. The reasons for this belief are as follows. The  $H_1^0$  beam is a "cleaner" beam than the  $H_1^+$  beam because the processes leading to the  $H_1^0$  beam are fewer in number and are more predictable than those leading to the  $H_1^+$  beam. That is, interactions between the  $H_2^+$  molecules and the target atoms leading to instantaneous three-body breakup or to the continuum cannot share in the production of the  $H_1^0$  beam as they do for the  $H_1^+$  beam. The  $H_1^0$  beam comes from only those interactions leading to the  $2p\sigma_u$  and higher electronic configurations, whose potential-energy curves are well known. The results of Salpeter and Alsmiller, cited above, lead one to expect that a large majority of the  $H_1^0$  atoms come from interactions in which the  $H_2^+$  molecules were excited to the  $2p\sigma_u$  state. We thus expect that the  $H_1^0$  atoms have for the most part a fairly simple history, and this history is reasonably uniform for most of the particles in the  $H_1^0$  beam. The reasons for choosing the thick-target yield curve instead of the thin-target yield curve are as follows. (1) The "thin target" used for the  $H_1^0$  beam (1.4 keV on the  $H_1^+$  energy scale) is not really thin for many purposes including the present one. (2) The thick-target yield curve involves better counting statistics than the thin-target curve. (3) The thick target has a smaller percentage of oxidation and other impurities than the thin target.

We now indicate a line of reasoning connecting the width of the  $H_1^0$  beam thick-target yield curve with the vibrational levels occupied by the original  $H_2^+$  molecules. The width of the  $H_1^0$  beam thick-target yield curve is dependent upon the  $H_1^0$  beam-energy spread, which is dependent upon the potential-energy-curve points to which the  $H_2^+$  molecules are excited. The populations of these points on the potential-energy curve are dependent upon the distribution of internuclear separation distances at the times of excitation, and the internuclear-separation-distance probability distribution is in turn dependent upon the vibrational levels occupied by the  $H_2^+$  molecules. It would be very difficult to work backward beginning with the known width of the  $H_1^0$  beam thick-target yield curve and proceeding to the unknown vibrational levels of the  $H_2^+$  molecules in the order just described. But it is fairly simple to proceed in the forward direction by (a) assuming a vibrational level for the  $H_2^+$  molecules, (b) calculating the probability distribution of the internuclear separation distances for this vibrational level, (c) calculating the probability distribution of potential-energy transfers from this separation-distance distribution using Fig. 23, (d) converting this distribution of potential energies to a distribution of final velocities in the c.m. system (using classical mechanics), (e) converting this distribution of c.m. velocities to energy spread in the laboratory system using Eq. (5), and finally (f) computing a thick-target yield curve from this incoming beam-energy spread.

The calculation of the c.m. velocity distribution of the  $H_1^0$  atoms as they emerge from the gas cell is based on the considerations given in the preceding section and the following assumptions. (1) The assumed vibrational level of the  $1s\sigma_g$  state is occupied by all the  $H_2^+$  molecules as they enter the gas cell. (2) The probability for a given distance between protons in the  $H_2^+$  molecule at impact is determined semiclassically by the shape of the  $1s\sigma_g$  well and the particular vibrational level from Fig. 23. (3) All excitations are to the  $2p\sigma_u$  state. (4) The Franck-Condon principle applies. (5) All spatial orientations of the internuclear axis are equally probable during excitation. (6) Neither the beam-energy spread due to the analyzer resolution nor the initial vibrational energy affects the broadening of the thick-target yield curve; the only broadening comes from the separation kinetic energy. (7) The molecular rotational motion does not influence the results.

Kerner (28) predicts that for electrons impinging on  $H_2^+$  molecules causing excitation to the  $2p\sigma_u$  state, the angular distribution of the resulting protons agrees very nearly with a  $\cos^2\theta$  curve, where  $\theta$  is the angle between the dissociating proton direction and the incoming electron-beam direction. In order to avoid the embarrassment of introducing a  $\cos^2\theta$  distribution into the analysis, we assume that the motion of the electrons in the gas atoms causes the dissociating proton directions to become isotropic relative to the incident  $H_2^+$  beam. (However, see the subsection " $H_2^+$  Beam Experimental" under "Discussion.")

The energy distribution for each particular internuclear separation distance is a rectangle corresponding to Eq. (6). Thus for a series of internuclear separation distances corresponding to a particular vibrational level there will be a series of rectangular energy distributions, each distribution having a weight proportional to the time the protons spend at that particular separation distance. The resulting effective energy distribution for any particular vibrational level will then be the sum of this set of rectangular distributions.

The above procedure was followed for three arbitrarily chosen  $J = 0$  (parahydrogen) vibrational levels,  $v = 0$ ,  $v = 3$ , and  $v = 7$ , eigenvalues for which are given by Cohen et al. (25) and are illustrated in Fig. 23. Assuming that the  $H_1^0$  atoms lose energy at the same rate as the average rate of loss for protons, and neglecting any fluctuations in energy loss, we have computed  $H_1^0$  beam thick-target yield curves for each of the three assumed values of  $v$ . Yield curves computed with the  $v = 0$  vibrational level showed more broadening than that observed experimentally, with the  $v = 3$  vibrational level showed about the right amount of broadening, and with the  $v = 7$  vibrational level showed too little broadening. Since some of the ignored effects would tend to broaden the observed yield curve (except for fluctuations in energy loss), the conclusion drawn from the  $H_1^0$  beam thick-target result is that the bombarding beam consisted of  $H_2^+$  molecules occupying vibrational levels higher on the average than  $v = 3$ .

The  $H_1^+$ <sub>s</sub> beam thick-target yield curve (Fig. 21) shows more broadening than the corresponding  $H_1^0$  beam yield curve, indicating more complicated modes of separation contributing to the  $H_1^+$ <sub>s</sub> beam than the modes responsible for the  $H_1^0$  beam; e.g., instantaneous three-body breakup or excitation of the  $H_2^+$  molecules to the continuum.

The thin-target gas-cell results (Fig. 22) confirm the thick-target results that the  $H_1^+$ <sub>s</sub> beam yield curve shows greater broadening than the  $H_1^0$  beam yield curve. The shape of the  $H_1^+$ <sub>s</sub> beam yield curve is qualitatively like that which is obtained from the distribution analysis given above; however, the  $H_1^0$  beam thin-target yield curve does not agree well with this interpretation. This failure of the analysis may be due to the fact that a target of greater thickness was used for the  $H_1^0$  beam thin-target yield curve (1.4 keV) than was used for the  $H_1^+$ <sub>s</sub> beam thin-target yield curve (0.3 keV).

#### Interpretation of the Yield Curves from the E-Series Targets

Calculating the yield curves for the E-series targets and the  $H_2^+$  beam is much more complicated than for the  $H_1^+$  beam for the following reasons. (1) The protons in the incident  $H_2^+$  molecules have initial internal kinetic energies the values of which depend on the populations of the vibrational levels and the instantaneous internuclear separation distances. (2) Interactions between the  $H_2^+$  molecules and the target electrons change the electronic configurations of the  $H_2^+$  molecules, resulting in the transfer of some laboratory-system kinetic energy to c.m.-system potential energy, the amounts depending on the relative populations of the repulsive states. (3) The positions of the  $H_2^+$  molecules on each particular potential-energy curve depend on the initial internuclear separations, which in turn depend on the vibrational level populations. (4) This potential energy is converted into internal kinetic energy which increases as a function of depth in the target. For an

$H_2^+$  molecule excited to the  $2p\sigma_u$  state from an initial internuclear separation of 2 Bohr radii, the average time required to convert 90 percent of the potential energy to kinetic energy is about  $3.7 \times 10^{-15}$  second. In this time a 1-MeV proton in an aluminum target will travel a distance equivalent to about 2.5 keV. (5) The rate at which this internal kinetic energy increases depends on which repulsive state is involved, the shape of the potential-energy curve, and the initial internuclear separation. (6) The contributions of these internal kinetic energies to the effective bombarding-energy distribution depend on the orientations of the internuclear axes with respect to the bombarding-beam direction. (7) The potential-energy curves of Fig. 23 are strictly valid only for a vacuum. The presence of the electric fields of the target electrons (and to some extent the target nuclei) modifies these potential-energy curves in some way.

In addition to these complications, the  $H_2^+$  beam calculations include all the complications involved with the  $H_1^+$  beam, including fluctuations in energy loss, beam-analyzer resolution, intrinsic resonance width, and Doppler broadening due to the thermal motion of the target nuclei. Because it is not clear a priori which of the above factors make significant contributions to the shape of the calculated yield curve, two separate sets of simplifying assumptions were made, and yield curves were computed for each set of assumptions. In the first case the fluctuations due to energy loss were considered to be the most important factor, and two discrete beam-energy distributions were considered: a narrow component arising from the initial incident internal velocities of the protons in the  $H_2^+$  molecules and a broad component arising from the internal proton velocities after all of the potential energy from the repulsive state has been converted into kinetic energy. In the second case the internal velocity distribution was allowed to become broader as a function of depth of penetration of the beam into the target according to the shape of the  $2p\sigma_u$  repulsive-state potential-energy curve.

Case One, Discrete Change in Internal Kinetic Energy - Equation (1) with a slight modification can be used for computing the  $H_2^+$  beam yield curve if the following simplifying assumptions are made. (1) The initial distribution in proton energies is due only to the vibrational motion of the  $H_2^+$  molecules and may be expressed as a Gaussian function with a relatively small standard deviation (narrow component). (2) The  $H_2^+$  molecules suffer random collisions in the target, these collisions resulting in discrete increases in the internal kinetic energy of the molecules. The amount of this increase depends on the potential energy of the electronic configuration involved. (3) The resulting distribution in proton energies is represented by another Gaussian function with a relatively greater standard deviation (broad component). (4) The relative number of protons included in the initial narrow component is represented by an exponential factor,  $\exp(-\alpha x)$ . This factor could be interpreted as being related to the cross section for dissociation of the  $H_2^+$  molecules or to the lifetime of the dissociation process. The relative number of protons in the broad component is represented by  $1 - \exp(-\alpha x)$ . (5) Symon's theory of fluctuations in energy loss is applicable.

Equation (1), thus modified, becomes

$$y(E_b, t) = n \int_{x=0}^t \int_{E_i=0}^{\infty} \int_{E=0}^{\infty} \sigma(E) g(\Delta_1, E_b, E_i) w(E, E_i, x) e^{-\alpha x} dE dE_i dx \\ + n \int_{x=0}^t \int_{E_i=0}^{\infty} \int_{E=0}^{\infty} \sigma(E) g(\Delta_2, E_b, E_i) w(E, E_i, x) (1 - e^{-\alpha x}) dE dE_i dx, \quad (7)$$

where  $g(\Delta_m, E_b, E_i) = (1/\sqrt{2\pi} \Delta_m) \exp[-(E_b - E_i)^2 / 2\Delta_m^2]$  and  $w(E, E_i, x)$  is the probability for a given energy loss  $\Delta T$ . The quantities  $\Delta_1$  and  $\Delta_2$  are the standard deviations of the energy spread before and after dissociation, respectively. The value for  $\Delta_1$  was derived

from the  $H_2^+$  beam target E-7 yield curve, and the value for  $\Delta_2$  was derived from the gas-cell yield curves.

Except for the factors  $\exp(-\alpha x)$  and  $1 - \exp(-\alpha x)$ , evaluation of Eq. (7) is the same as evaluations of Eq. (1) for two values of  $\Delta_m$ . A simple computer program modification of Eq. (1) is all that was necessary to evaluate Eq. (7). The results of this calculation are shown in Fig. 24 for the E-series targets. Some of the datum points are also shown for each yield curve. For the thinner targets (E-4 through E-7), the assumed mechanism yields results which are in reasonable agreement with experiment. The values used for  $\Delta_1$  and  $\Delta_2$  are 0.524 keV and 1.98 keV, respectively. If we rewrite Eq. (5) so that the  $\cos \theta$  term appears with the energy  $E'$ , then we can redefine  $E'$  as an energy which arises from the component of velocity in the direction of the beam. By substituting the assigned values of  $\Delta_1$  and  $\Delta_2$  for  $\Delta E$  in Eq. (5), we can find values for  $E'$  which are related to some average of the forward component of internal velocity. Ideally from these values of  $E'$ , one could determine the internal kinetic energy of the  $H_2^+$  molecules, but the assumptions made appear to be too crude for an accurate analysis. However, it is of interest to compare the numbers obtained from this simple calculation with those obtained from the potential-energy curves of Fig. 23.

The value of  $E'$  found from  $\Delta_1$  is 0.069 eV and may be compared with the initial internal kinetic energy of the  $H_2^+$  molecule (or the average vibrational level). The maximum kinetic energy available to each of the protons in the  $H_2^+$  molecule in the  $v = 0$  level is 0.073 eV. Since both the orientation factor and the kinetic-potential energy oscillator factor tend to make the observed effective internal kinetic energy less than this value of 0.073 eV, the value of 0.069 eV obtained from  $\Delta_1$ , which was itself determined from the experimental data, indicates an average population above the  $v = 0$  vibrational level. This result, which was obtained from the  $H_2^+$  beam thin-target yield curve, is consistent with the above result obtained from the gas-cell experiments indicating an average population above the  $v = 3$  level.

The value of  $E'$  found from  $\Delta_2$  is 0.99 eV and may be related to the kinetic energy gained by the protons (or proton and atom) during the dissociation process. The maximum instantaneous kinetic energy available to each proton in the bound state (highest vibrational level) is about 1.4 eV. Since again the orientation factor and the oscillator factor tend to make the observed effective internal kinetic energy much less than this maximum value of 1.4 eV, and since we are sure that not all the  $H_2^+$  molecules are in this highest level, the value of 0.99 eV obtained above indicates that one or more of the repulsive states of the  $H_2^+$  molecule participate.

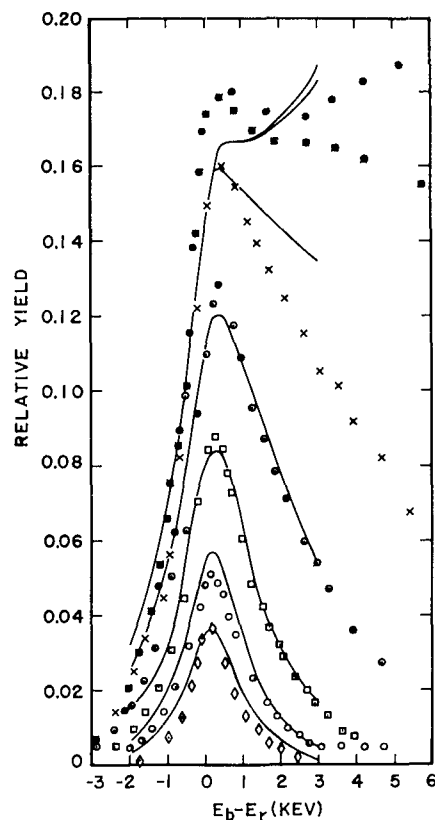


Fig. 24 - Theoretical yield curves and datum points for the E-series aluminum targets,  $H_2^+$  beam, and 992-keV resonance. The abscissa values have been converted to the  $H_1^+$  energy scale. The energy scale has been adjusted visually for each pair of experimental and calculated yield curves for the purpose of obtaining true resonance energy. Not all datum points are shown.

Preliminary evaluations of Eq. (7) were made for several different values of the quantity  $\alpha$ . The value of  $\alpha$  which gave the best agreement between the calculated curves and the experimental data was 10 (in units of  $10^5 \text{ cm}^{-1}$ ), and the curves of Fig. 24 were computed with this value. If this exponential factor is related to the cross section for dissociation, then this cross section for aluminum (or  $\text{Al}_2\text{O}_3$ ) as found from  $\alpha$  is about  $0.85 \times 10^{-17} \text{ cm}^2/\text{atom}$ . This result is anomalously low since cross sections for the dissociation of  $\text{H}_2^+$  molecules in elements the order of  $Z = 13$  are about  $10^{-16} \text{ cm}^2/\text{atom}$ .

Because of the possibility (remote) that in nature a thin foil might present an anomalously low cross section for the dissociation of  $\text{H}_2^+$  molecules, thin aluminum oxide foils were made according to the method described by Hauser and Kerler (29). A commercial household aluminum foil was found to be satisfactory for the starting material. A citric acid bath was used for anodizing the aluminum. The foil coated with aluminum oxide thus obtained was clamped between stainless steel rings. The aluminum oxide was removed from one side of the foil with sodium hydroxide; and a weak hydrochloric acid solution, with a small amount of  $\text{CuCl}_2$  added as an inhibitor, was used to remove the aluminum. The thinnest foil which survived the process of installation into the vacuum system was about 70 Å thick. The foil could be rotated into and out of the path of a beam of 2-MeV  $\text{H}_2^+$  molecules. A small magnet separated the residual beam components, and the  $\text{H}_2^+$  beam component was measured with and without the foil in the beam path. The dissociation cross section thus obtained is  $0.63 \times 10^{-16} \text{ cm}^2/\text{atom}$  with some unknown uncertainty.

Because this measured value is not anomalously low, it appears more reasonable to interpret the exponential factor  $\alpha$  in terms of a mean lifetime of the initial distribution represented by  $\Delta_1$  instead of in terms of a cross section for dissociation. This mean lifetime is easily calculated to be  $0.7 \times 10^{-15}$  second, corresponding to a depth of penetration of 1-MeV protons into the target of about  $0.1 \times 10^{-5} \text{ cm}$ , which for pure aluminum is a target about 500 eV thick (3). (Target E-6 was 600 eV thick if assumed to be pure aluminum.) Note that this lifetime determined from the yield curves is less than the "lifetime" calculated for the  $2p\sigma_u$  state ( $3.7 \times 10^{-15}$  second), thus implying that a large fraction of the dissociations occur via excitation to the  $2p\sigma_u$  state rather than to higher states all of which have substantially longer lifetimes.

Case Two, Continuous Change in Internal Kinetic Energy - The agreement between the calculated curves and the experimental data for the four thinnest targets of the E series lends significance to the interpretation of the parameters  $\Delta_1$ ,  $\Delta_2$ , and  $\alpha$ . However, the lack of agreement between the thick-target calculated curves and the data perhaps indicates one or both of the following. (1) The discrete change in internal kinetic energy represented by a jump from  $\Delta_1$  to  $\Delta_2$  is not a good approximation for the thicker targets. (2) The assumed exponential shape of the decrease in the initial component is not a good approximation.

The second set of calculations was made without either of these two assumptions. However, the assumptions listed on page 44 were used except that the internal kinetic energy was allowed to vary continuously as a function of depth in the target. This changing kinetic-energy function was based on the shapes of certain repulsive-state potential-energy curves and the time in the target. The following additional assumptions were made. (1) The effect of the presence of the target electrons on the shape of the potential-energy curve is negligible. (The validity of this assumption is highly questionable.) (2) The probability for a transition from the  $1s\sigma_g$  state to a repulsive state is given by the measured total cross section for dissociation, about  $10^{-16} \text{ cm}^2/\text{atom}$ . (3) The targets consist of pure aluminum.

Yield curves were computed based on the preceding set of assumptions, and as in case one there was agreement for the thinnest targets; but for the thicker targets the agreement was not quite so good, although the agreement was better than for case one. The general character of the experimental thick-target yield curve was present in the

calculated curve; i.e., the calculated yield curve was steeper beyond the midpoint, and the curve showed a slight hump. These calculated curves are not shown because they are not sufficiently different from those of Fig. 24 to warrant another figure. Different initial vibrational levels were assumed ( $v = 0, 3, \text{ and } 7$ ). Also yield curves were computed both with and without fluctuations in energy loss. For the curves computed with fluctuations in energy loss, only those fluctuations occurring in the region of validity of the Landau distribution ( $< 0.5 \text{ keV}$  average energy loss) were applied to the calculation. Beyond this region, and for the curves computed without fluctuations in energy loss, a uniform rate of energy loss was assumed. The best agreement between calculated curves and experimental data was obtained for the combination  $v = 3$  and the use of Landau fluctuations in energy loss.

#### Qualitative Explanation of the Anomalies

The series of anomalies observed with the  $\text{H}_2^+$  beam on targets of different thicknesses is experimentally rather similar to that observed with the  $\text{H}_1^+$  beam. However, the explanation of these  $\text{H}_2^+$  beam anomalies is quite different from that used for the  $\text{H}_1^+$  beam. An immediately apparent difference is that the internal vibrational energy of the  $\text{H}_2^+$  molecules leads to a Doppler broadening of the yield curve, but this factor alone would lead to symmetric yield curves. The asymmetric features of the  $\text{H}_2^+$  beam yield curves are mainly the result of further broadening introduced by the dissociation of the  $\text{H}_2^+$  molecules after they are excited to repulsive electronic states by interactions with the target atoms.

In the case of the gas-cell experiments, enough time was available to the dissociating molecules that all of the potential energy available to the dissociation process was transformed into kinetic energy before the particles reached the target. For each proton which received an increase in energy, there was a corresponding proton which received an equal decrease in energy; and thus the resulting distribution of energies in the bombarding beam was symmetric about  $E_b$ . Because the energy spread which results from the dissociation process is due to the addition of velocity vectors, the amount of the extra energy spread would be the order of several keV even if there is available only 1 eV to the dissociation process. This relatively large energy spread is sufficient to mask the effects due to fluctuations in energy loss, and the yield curves obtained with the  $\text{H}_1^0$  and  $\text{H}_1^+$  beams are reasonably symmetric about resonance energy, and the midpoint of the rise in the thick-target yield curve is located very near resonance energy. However, when a solid target is bombarded by the  $\text{H}_2^+$  beam, the resulting dissociation takes place inside the target, thus leading to an energy distribution whose width increases as a function of depth of penetration of the beam into the target. The result is an overall asymmetric yield curve for thick targets.

In the front layers of the target a significant portion of the beam is gaining energy from the dissociation process faster than it is losing energy through ordinary energy-loss interactions. This effect is especially important when  $E_b \leq E_r$ , for it causes some protons to remain near resonance energy for abnormally long times and some to pass through resonance energy twice. Furthermore, even for values of  $E_b$  sufficiently below  $E_r$  that essentially none of the protons in the incident beam have energies great enough to contribute significant gamma-ray yield, some protons will gain enough net energy inside the target to reach resonance energy and thus contribute significant gamma-ray yield. It is this latter result that gives the long slow rise beginning more than 5 keV below resonance energy (Curve IV, Fig. 21).

A similar line of reasoning explains the observed result that the position of the midpoint of the rise is significantly below resonance energy.

As  $E_b$  becomes greater than  $E_r$ , e.g., 2 keV greater, the yield decreases for the following reason. When the bombarding energy is greater than the resonance energy, the

yield no longer comes predominantly from the front layers of the target. Most of the incident protons have too much energy while they are in the front layers to contribute to the gamma-ray yield. So their contribution to the yield occurs in the deeper layers of the target after they have lost some energy, about 1 or 2 keV average loss. For these higher bombarding energies there is no "extra" yield from those protons which have an initial rate of energy gain or zero energy change. But there is a yield "loss" from those protons which lose energy because of the dissociation process and hence pass through resonance much more quickly than they would from the ordinary energy-loss process alone. Even if the target is several keV thick, the yield will decrease as the bombarding energy is increased above resonance, leading to the presence of the hump. In a thin target, it is this same effect which causes the peak of the yield curve not to shift by half the target thickness.

As the bombarding energy is increased still further, more and more of the "losing" protons still have energies above resonance even after the dissociation process is essentially complete. Therefore they pass through resonance at the normal rate of energy loss, thus making a greater contribution to the yield. The result is a rising yield, as a function of bombarding energy, until all of the "losing" protons pass through resonance energy at the normal rate. This second rise in yield is shown clearly in Figs. 17 and 21. For a sufficiently thick target, a plateau would eventually be reached, but none of the E-series targets is thick enough to exhibit one.

The results with the copper-coated targets can be visualized qualitatively with the dissociation mechanism. The enhanced broadening effect of the copper coating on the  $H_2^+$  beam thin- and thick-target yield curves as compared with the  $H_1^+$  beam yield curves is due to the fact that part of the dissociation of the  $H_2^+$  molecules occurs in the inert copper coatings, thus eliminating the yield which would otherwise have been obtained from the front of the target, where the beam-energy spread is the smallest.

For thick targets of aluminum with the thicker copper layers, it was observed that the shift of the  $H_2^+$  beam yield curve midpoint due to the coating was also greater than for the  $H_1^+$  beam. As shown in the preceding discussion, the anomaly of the low midpoint for thick targets and the  $H_2^+$  beams depends upon the dissociation acceleration occurring in the aluminum target. If the dissociation acceleration occurs before the protons reach the aluminum target, there is no anomalously low midpoint, as seen from the gas-cell results. If a copper layer is sufficiently thick, the dissociation acceleration will be complete before the protons reach the aluminum. Thus the shift of the midpoint of the  $H_2^+$  beam yield curve for a copper-coated target includes two factors: the normal shift due to energy losses plus the shift due to the obviation of the anomalously low midpoint related to the dissociation process. On the other hand, the  $H_1^+$  beam midpoint shift depends only on the energy losses.

The fundamental idea explaining the anomalies with  $H_1^+$  beams, fluctuations in energy loss, is applicable to  $H_2^+$  beams also, but it is of less importance than the separation acceleration due to the repulsive state to which the  $H_2^+$  molecule is excited.

#### APPLICATION TO RESONANCE-ENERGY DETERMINATION WITH THE $H_2^+$ BEAM

The  $H_2^+$  beam can be used for accurate calibration of bombarding-beam energy analyzers provided that either extremely thin targets are used (thinner than about 500 eV) or the effects of dissociation and fluctuations in energy loss are taken into account with intermediate or thick targets.

### Thin Targets

If extremely thin targets are used and if the  $H_1^+$  and  $H_2^+$  beam yield curve peaks are compared on the same energy scale, the positions of the peaks will agree within 0.01 percent. From the experimental data for target E-7 and from the absolute calibration parameters of the electrostatic analyzer, the positions of the peaks for the  $H_1^+$  and  $H_2^+$  beams occur at 992.10 and 992.17 keV, respectively, thus differing by only 0.007 percent. These values include no correction, theoretical or otherwise, for any shift of the peak from true resonance energy. If a correction is applied, based on calculations like those made herein, the agreement between the  $H_1^+$  and  $H_2^+$  results improves. According to the calculated yield curves (Fig. 7) the peak for the  $H_1^+$  beam on target E-7 (assumed to be pure aluminum) occurs about 50 eV higher than the true resonance energy, while for the  $H_2^+$  beam (Fig. 24) the corresponding peak is 150 eV higher than the true resonance energy. If one subtracts these values from the peak energies, the corrected resonance energies become 992.05 and 992.02 keV, respectively, differing by only 0.003 percent.

Figure 7 also shows that if target E-7 is completely oxidized (thus being about 0.6 keV thick instead of 0.3 keV), the peak of the calculated  $H_1^+$  beam yield curve is about 150 eV higher than true resonance energy. While calculated  $H_2^+$  beam yield curves were made only for pure aluminum targets, the curve for target E-7 (Fig. 24) would not have been very much different if target E-7 had been assumed to be completely oxidized, as can be seen by comparison of the curves E-7 and E-6 (Fig. 24). Thus again the positions of the peaks for the two beams would agree within about 0.01 percent. The above discussion, based on narrow resonances and highly resolved beams, indicates that for target materials which oxidize readily and also for those which do not the positions of the thin-target peaks for the  $H_1^+$  and  $H_2^+$  beams (when plotted on the same energy scale) agree with each other within about 0.01 percent.

The energy of the 992-keV resonance has been determined from the  $H_2^+$  beam yield curves for targets E-3 through E-7 under the following assumptions. (1) The absolute values of the electrostatic analyzer parameters are known. (2) The analyzer is linear. (3) The theory leading to the calculated curves of Fig. 24 is applicable. The arithmetic unweighted average of the resonance energy for the five targets is 992.05 keV, which is 0.014 percent higher than the best value obtained from the  $H_1^+$  beam results with all seven E-series targets.

### Thick Targets

If thick targets are used, it is reasonably safe to assume that the midpoint of the experimental rise of an  $H_2^+$  beam yield curve will occur for all narrow resonances ( $\Gamma < 100$  eV) and high beam-energy resolutions (better than about 0.05 percent) about 0.05 percent below true resonance energy as in Fig. 17 for target E-1. When this correction is applied to the experimental data, the midpoints of the rise for the yield curves with the two different beams should agree with each other within about 0.02 percent. This judgment is based on experience with several narrow resonances at bombarding energies from 0.5 to 2 MeV in different target materials. It does not appear feasible at the present time to calculate theoretically the precise amount of this displacement for an arbitrary target material, resonance width, beam-energy inhomogeneity, and ion source condition. However, the difficulty of this calculation does not preclude the use of  $H_2^+$  beams for calibration and linearity checks because the apparent constancy of the experimental value of this percentage displacement makes it sufficiently accurate for most beam-energy analyzer calibrations.

## DISCUSSION

## Recapitulation

A number of anomalies in  $(p, \gamma)$  yield curves have been observed with  $H_1^+$  beams on targets of different thicknesses. The most striking of these anomalies is the fact that the peaks of moderately thin targets do not shift from true resonance energy by an energy that is even comparable with half the target thickness. Most of the other anomalies observed with  $H_1^+$  beams are simply different manifestations of this anomaly. These and all other anomalies observed with  $H_1^+$  beams have been explained by the application of the theory of fluctuations in energy loss, including target contamination effects. The most important feature of this theory is that the most probable energy loss for thin layers is usually much less than the average energy loss, resulting in an asymmetric energy-loss distribution with its peak near zero. Using this theory we have succeeded in calculating yield curves which are in excellent agreement with the experimental data for all target thicknesses.

A number of somewhat similar anomalies have been observed with  $H_2^+$  beams. For these beams, the most important factor in determining the shape of the yield curves is the separation acceleration resulting from the repulsive electronic states to which the  $H_2^+$  molecules are excited by collision with the target atoms. Fluctuations in energy loss are of secondary importance.

This entire series of experiments was initiated by observations made in the course of a program of preparing a new absolute precision energy scale for nuclear-reaction accelerators. At one time it appeared that the instrumental precision significantly exceeded the precision of interpretation of the results, primarily because of the lack of a detailed understanding of the interactions in the atomic, rather than the nuclear, domain. The success of the theoretical interpretations herein implies that these interactions are now sufficiently well understood that one can take full advantage of all available instrumental precision for both  $H_1^+$  and  $H_2^+$  beams.

## Related Work

A preliminary account of part of the present paper (the energy displacement of the  $H_2^+$  beam thick-target yield curve and the asymmetry of the same curve) has been published in abstract form (3). In the intervening period, work closely related to the present series of experiments has been performed at two other laboratories. The University of Oslo group has observed some of the anomalous features of the  $H_2^+$  beam thick-target excitation curves and published their results (30). The University of Wisconsin group has observed some of the anomalous features with both  $H_1^+$  and  $H_2^+$  beams, and they have published their results in many different places (31-41).

Since there is some overlap between our work reported herein and that reported elsewhere, the question arose as to whether we should revise the present manuscript to delete material which has already been published by others. There are several reasons why we chose not to do so. (1) It is extremely desirable that the entire series of experiments be presented as one coherent whole rather than fragmented among several articles by different authors. (2) The experimental procedures used by the other groups were different from ours. (3) Their explanations of the anomalies are different in detail (although not in general). (4) To the best of our knowledge the work reported herein is the only instance in which entire  $(p, \gamma)$  yield curves have been satisfied by calculation for a wide range of target thicknesses. (5) There are several points of disagreement in results and interpretation between our work and the Wisconsin work.

There is general agreement between the Wisconsin experiments (34,38) confirming the existence of the hump first reported by del Callar (9) and those reported herein, although there are differences in detail. The explanation of the hump for  $H_1^+$  beams on thick-target yield curves as given by Lewis (35) is in qualitative agreement with the theory presented herein.

Walters et al. (Ref. 38, page 2014) found that targets having the same interquartile interval were sufficiently different that one showed the  $H_1^+$  beam thick-target hump and the other did not. This observation is in disagreement with our results with aged targets and rotated targets. We found that the interquartile interval value is as sensitive to impurities and contaminants as the hump. So if one target shows a hump and another does not, then the interquartile intervals will be significantly different.

Of the anomalies observed with the  $H_2^+$  beams, the most important was the "energy shift" of the midpoint of the rise in the thick-target yield curve. In order to confirm the "shift" as a real effect in nature we undertook a detailed program of examining all the parameters of the electrostatic analyzer for linearity and compensating effects as a function of voltage applied to the deflecting plates (and thus particle energy). These checks and procedures, as described, are a necessary and primary means of proving an analyzer sufficiently linear to establish the observed "energy shift" with  $H_2^+$  beams as a real effect. The internal and external magnetic field corrections in Eq. (4), for example, are about the same magnitude as the apparent midpoint displacement.

After the primary checks mentioned above, the secondary check is to measure the resonance energy with the  $H_2^+$  beam on an extremely thin target and to compare the resonance energy thus obtained with that predicted from the measurement with the  $H_1^+$  beam and the absolute calibration parameters. As described herein we made this check and obtained agreement within 0.01 percent between the two measurements.

The Wisconsin group has given no indication (32,38) that they have investigated the factors mentioned above, nor do they substantiate their claim (32) that they had established the "energy shift" with  $H_2^+$  beams to be a real effect in nature.

Andersen et al. (30) of Oslo, also observed the asymmetry of the  $H_2^+$  beam thick-target yield curve and measured the displacement of the energy of the midpoint of the rise to be 0.05 percent. On the basis of the same evidence that was subsequently obtained by the Wisconsin group, the Oslo group correctly did not draw a definite conclusion as to whether the displacement was real or was the result of nonlinearities in their analyzer.

Our conclusions concerning the use of  $H_2^+$  beams for precise energy calibration are different from those of the Wisconsin group (38) in that our results indicate that one can use the  $H_2^+$  beam for precise (order of 0.01 percent) calibration of beam-energy analyzers.

The Wisconsin results (34,38) show that poorer instrument resolution (e.g., 0.1 percent) affects the detailed shape of the  $H_2^+$  beam yield curves. We do not disagree with this statement, but within the range of the resolution of our electrostatic analyzer (0.01 percent to 0.05 percent) we are unable to see any significant difference in the detailed shapes of the yield curves taken with  $H_2^+$  beams.

Since precise quantitative interpretations of  $(p, \gamma)$  resonance yield curves have been successfully completed, it is desirable that a corresponding analysis be made for  $(p, n)$  thresholds. Relatively simple modifications to our computer program for the evaluation of Eq. (1) allow us to calculate the shape of  $(p, n)$  yield curves near threshold. Thus we can take into account fluctuations in energy loss as well as all the usual factors affecting the shapes of  $(p, n)$  yield curves. Such calculations have been performed (42).

## Suggested Future Work

The present series of experiments began more than five years ago as a modest program to seek the cause of the energy-displacement discrepancy for  $H_2^+$  beam thick-target measurements. As disclosed herein, efforts to understand the one discrepancy led to a host of others and to a very extensive series of experiments. The experimental measurements phase of the program ended about three years ago. During the analysis phase of the program, a number of additional possible experiments were conceived, but due to the pressure of other experimental commitments, it has not been feasible to renew the experimental measurements. Therefore the following ideas for additional experiments are offered to anyone who wishes to undertake them. It is perhaps worthwhile at this point to remind the reader that some of the most interesting experiments reported herein (e.g., the final series of stripped-beam measurements with the gas cell and neutral-beam resonance curves) were performed without the electrostatic analyzer, but with only a fairly conventional magnetic analyzer. Thus experiments of this nature are not confined to those laboratories possessing unusually high-resolution beam-energy analyzers. But it should be emphasized that for high-quality results the targets should be made extremely clean and kept clean, free of vacuum-system carbon deposits. Our experience indicates that the best way of accomplishing this latter goal is to enclose the target with a tube kept at liquid-nitrogen temperature.

Some of the suggested work is of a theoretical nature and therefore requires no accelerator.

$H_1^+$  Beam Theoretical - In the course of the work reported herein it became apparent that further theoretical work is needed on the mechanism of fluctuations of energy losses suffered by charged particles in penetrating matter. Symon's theory appears to be reasonably adequate for the target atomic numbers and bombarding energies used in the present work, but these applications are outside the limits specified by Symon, and therefore the range of applicability is not accurately known. We believe that the theory would not be applicable for some combinations of high atomic numbers and low bombarding energies. What is needed to extend the range of applicability to higher atomic numbers and lower energies is an effective inclusion of K and L shell corrections.

Another desirable extension of Symon's theory is toward the region including extremely thin targets. Both Landau and Symon ignored energy fluctuations due to distant interactions, i.e., interactions in which the atomic electrons may not be treated as free. This procedure is justified only if the target is not too thin. But for extremely thin targets distant interactions should be taken into account.

$H_1^+$  Beam Experimental - Most of the work suggested in this section requires a high-resolution beam-energy analyzer.

It would be worthwhile for someone to make a series of measurements and calculations for other  $(p,\gamma)$  resonances. For these measurements we would suggest the choice of a target material which is relatively inert chemically in order to decrease the uncertainties due to oxidation. The chosen resonances should be relatively isolated.

For a given set of conditions, the slope of the rise of the yield curve calculated with Eq. (1) will be greater than when calculated with an equation in which the energy loss of the protons is assumed to be equal to  $kx$ , where  $k$  is the average energy loss rate  $dE/dx$ . Thus if the latter assumption is made for the computation of yield curves as a function of  $\Gamma$ , comparison of the experimental data with the slope alone will lead to an anomalously low value for  $\Gamma$  if extremely pure surface conditions exist on the target. For values of  $\Gamma$  greater than several hundred eV there is no serious problem of determining  $\Gamma$  with reasonable precision, e.g., 20 percent. However, for values of  $\Gamma$  equal to or less than 100 eV the effects of surface contamination on the slope of the rise can introduce

uncertainties of 50 percent or more in the determination of  $\Gamma$ . Thus because of the contamination problem no effort has been made in the present work to assign precise values of  $\Gamma$  to the various resonances. It is suggested that further work be done to eliminate or understand more quantitatively this contamination effect.

Further investigation of the phenomenon of target "aging" appears desirable. We have attributed the increased thick-target interquartile interval for old targets to the growth of an extremely thin ( $\leq 100$  eV thick) film on the face of the target during the storage period. A study of the nature and rate of growth of this film might prove interesting. If the film is carbonaceous, an independent measure of its thickness can be made by the use of the  $C^{12}(He^3, p\gamma)N^{14}$  reaction, because this reaction is a prolific source of gamma rays from the first excited state of  $N^{14}$  (2.3 MeV).

It appears possible that the experimental height of the hump could be used as a measure of the width of a resonance for targets whose purities are known; that is, the narrower the resonance, the greater the height of the hump. In order to illustrate this idea quantitatively, we have computed the height of the hump for several assumed values of  $\Gamma$  from 25 eV to 500 eV for the following conditions: a pure  $Ni^{58}$  target,  $E_r = 1843$  keV, and a beam-energy resolution of 0.01 percent. These values result in the curve of Fig. 25. The left ordinate (curve I) is the percentage rise of the hump above the plateau of the thick-target yield curve. The right ordinate (curve II) is the displacement of the peak of the hump from resonance energy. Curves of similar shape result if  $\Gamma$  is assumed constant and the height of the hump is determined as a function of beam-energy resolution. Conversely, if the resonance width is known, or if there exists an uncontaminated target, the height of the hump can be used as a measure of the depth of oxidation or degree of contamination.

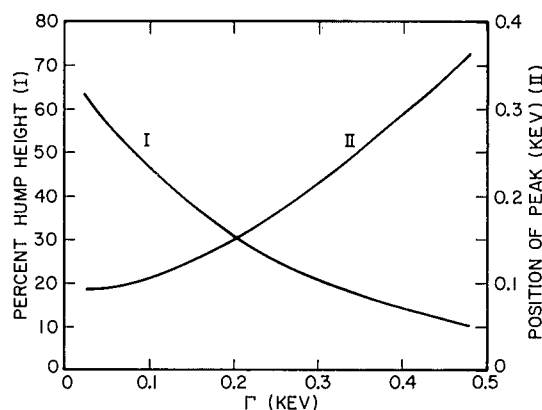


Fig. 25 - Curve I (left ordinate) is the theoretical hump height (as a percentage of the plateau height) as a function of  $\Gamma$ . Curve II (right ordinate) is the displacement of the peak of the hump from  $E_r$  as a function of  $\Gamma$ . The assumed parameters are a thick pure nickel target,  $E_r = 1843$  keV, and an  $H_1^+$  beam-energy spread of 0.01 percent.

The theoretical hump height has been computed for resonances in other materials. For the  $C^{13}(p, \gamma)$  resonance at 1747 keV, an assumed  $\Gamma$  of 80 eV, and a beam-energy resolution of 0.01 percent the theoretical hump height is 17 percent. The observed hump height was 7 percent. The stopping power  $dE/dx$  for protons of 1747 keV on  $C^{13}-C^{12}$  is about 330 MeV/cm, and for protons of 1843 keV on  $Ni^{58}$  the stopping power is about 810 MeV/cm. For the  $Ni^{58}$  case the theoretical hump height is 56 percent and the observed hump height is 28 percent. Thus we see a correlation between stopping power and theoretical hump height, the higher stopping power leading to a higher hump.

$H_2^+$  Beam Theoretical - It appears unjustified at the present time to devote further effort toward improving the agreement between the calculated and experimental curves for  $H_2^+$  beams on thick targets because (a) it is quite clear from the degree of fit obtained that the essential features of all the anomalies observed with  $H_2^+$  beams can be explained on the basis of the mechanism of dissociation of the  $H_2^+$  molecule and fluctuations in energy loss and (b) the amount of time required is large enough to warrant a separate undertaking.

It would be desirable in any further work to include the Symon theory of fluctuations in energy loss and the effect of target electrons on the potential governing the separation of the dissociation components of the  $H_2^+$  molecule. Another aspect that should be included is to determine quantum mechanically the internuclear separation probability for the various vibrational levels.

$H_2^+$  Beam Experimental - Most of the work suggested in this section and the next section does not require a beam-energy analyzer with unusually high resolving power.

It would be interesting to perform the  $H_2^+$  beam experiments with different ion sources and different power levels for each ion source. Such different types of ion sources and modes of operation could conceivably give  $H_2^+$  beams having different distributions of vibrational levels with consequently different resonance curve shapes. For example, the Oslo group (43) used the  $H_2^+$  beam from their accelerator to measure the relative energies of two closely spaced resonances in the  $Al^{27}(p,\gamma)$  reaction near  $E_b = 505$  keV (proton energy scale). They were able to obtain sufficient separation of the thick-target yield-curve steps to make positive identification of the two resonances. We attempted to reproduce the experiment, and even though the electrostatic analyzer was used at a high resolution (1 part in 5000), we observed a greater broadening and hence did not clearly resolve the two resonances.

It appears not to be difficult to design an experiment to measure the probabilities of  $H_2^+$  breakup in a gas via the various repulsive states and three-body breakup. The branching ratio for  $H_2^+$  breakup into  $H_1^+$  and  $H_1^0$  in the gas cell can easily be measured. If this branching ratio were measured for certain gas-cell parameters, these values could be compared with the theoretical predictions, and the amount of three-body breakup could be determined.

Other types of gases could be used to strip the  $H_2^+$  beam with possible different cross sections and branching ratios. The angular dispersion of the stripped beam could be measured and compared with theoretically expected values. In the present experiments, the physical size of the  $H_2^+$  beam on a quartz plate about one meter from the gas cell was about 1 mm in diameter with "zero" pressure in the cell. With a pressure of about  $5 \times 10^{-2}$  torr of  $N_2$ , the physical size of the stripped-beam components was about 3 mm in diameter. It is not known whether the exit aperture of the gas cell influenced this size.

In one of our earliest excitation curves with the  $H_1^+$  beam, a thick target, and the 992-keV resonance the rise of the yield curve flattened off in a narrow region at resonance energy. This curve was symmetric about resonance energy. When this curve was differentiated to obtain the equivalent thin-target yield, two peaks were present, one on each side of the resonance energy. Possible interpretations of these results are that either there were two resonances or there were two  $H_1^+$  energy groups. The first possible interpretation is known to be incorrect. The second interpretation suggests that there is a preferential internuclear-axis direction for  $H_2^+$  molecule breakup (28). A second measurement of the excitation curve immediately after the first confirmed the shape first obtained. Several weeks later we attempted to reconfirm this "double-valued" shape of the  $H_1^+$  thick-target yield curve, but were unable to do so. It is conceivable that the "double-valued" shape was obtained under a particular combination of experimental parameters which we did not reproduce.

Another possible effect is that the stripping cross section is dependent upon the vibrational levels of the  $H_2^+$  molecules. If this is the case, interesting results might be obtained if one measured the excitation curves of thin and thick targets with the residual  $H_2^+$  beam emerging from the gas cell. That is, if the gas-cell pressure is in the region of 1 to  $5 \times 10^{-2}$  torr and one uses a magnetic beam separator and accepts only the residual  $H_2^+$  component, it is conceivable that the excitation curve might be wider or narrower than with the total  $H_2^+$  beam, implying some preferential type of stripping.

General - We had intended to perform a series of experiments with the  $H_3^+$  beam analogous to the experiments with the  $H_2^+$  beam, but the greatly extended length of the  $H_2^+$  beam experiments (compared with what we originally anticipated) and the pressure of other experimental commitments precluded the  $H_3^+$  beam experiments. It appears quite likely that such experiments would be very interesting indeed, but probably not simple. It is easy to speculate on the probable results of such experiments, but it appears wiser to wait until the experiments are performed before "explaining the results."

Only a very limited amount of experimental effort went into the target-coating experiments (in which copper was evaporated onto the aluminum targets). It appears worthwhile for a more exhaustive set of experiments to be performed, i.e., more detailed measurements of the displacement of thin-target yield-curve peaks and thick-target yield-curve midpoints with the  $H_1^+$  and  $H_2^+$  beams as a function of coating thickness. In addition to copper, other coating materials should also be tried, and other narrow resonances in other target materials should be used.

The problem of errors in absolute measurements with electrostatic analyzers has long plagued experimenters, and in particular the problem of electric charge accumulation on insulating layers on the deflecting plates has been unresolved. The tests reported herein have shed much light on this problem, but more work is needed before the problem will be completely understood.

Finally, the use of an  $H_2^+$  beam (or perhaps  $H_3^+$  beam) and a gas-cell stripper offer the possibility of an intensive study of neutral-beam ( $H_1^0$ , and perhaps also  $H_2^0$ ) interactions, such as excitation curves and mode of breakup of the  $H_1^0$  atom and the possibility of producing a postacceleration polarized proton beam.

#### ACKNOWLEDGMENTS

For their valuable contributions, we are grateful to the following persons: Mr. C. A. Kennedy and Mr. A. del Callar for help during the experimental phase of the problem; Miss M. E. Toms and Mr. E. Cutler for assistance in programming the LGP-30 computer for some of the preliminary calculations; Mr. H. Hancock, Miss Sarah Hill, and the staff of the Research Computation Center of NRL for the NAREC program for evaluating Eqs. (1) and (7); Dr. W. Börsch-Supan and Miss Ruth Zucker of the Computation Laboratory of the National Bureau of Standards for the evaluation of the Landau function; Mr. K. L. Dunning and Dr. R. G. Glasser for many valuable suggestions and discussions; and Miss E. E. Dowling for many helpful criticisms and suggestions during the preparation of this manuscript. Finally we would like to thank those of our colleagues (whose numbers are legion) who patiently listened to our discussions of the anomalies and, especially in the early phases of the experiments, offered their encouragement.

## REFERENCES

1. W.A. Fowler, C.C. Lauritsen, and T. Lauritsen, *Revs. Modern Phys.* 20, 236 (1948)
2. H.E. Gove, "Resonance Reactions, Experimental," Chap. VI, *Nuclear Reactions*, Vol. I, Ed. by P.M. Endt and M. Demeur, North-Holland Publishing Company-Amsterdam, Interscience, New York, 1959
3. R.O. Bondelid, J.W. Butler, and C.A. Kennedy, *Bull. Am. Phys. Soc.* 2, 381 (1957)
4. D.F. Herring, R.A. Douglas, E.A. Silverstein, and R. Chiba, *Phys. Rev.* 100, 1239(A) (1955)
5. K.L. Dunning, R.O. Bondelid, L.W. Fagg, C.A. Kennedy, and E.A. Wolicki, "Development and Performance of NRL's Large Electrostatic Accelerator," Report of NRL Progress, May 1955, p. 8
6. R.O. Bondelid and C.A. Kennedy, *Phys. Rev.* 115, 1601 (1959); also NRL Report 5083, May 19, 1958
7. W.A. Higinbotham and S. Rankowitz, *Rev. Sci. Instr.* 22, 688 (1951)
8. K.L. Dunning, J.W. Butler, and R.O. Bondelid, *Phys. Rev.* 110, 1076 (1958)
9. A. del Callar, "An Absolute Determination of an  $\text{Al}(p, \gamma)\text{Si}$  Resonance Using the Naval Research Laboratory 2-Meter Electrostatic Analyzer," Master of Science Thesis, Catholic University of America, 1959
10. N. Bohr, *Phil. Mag.* 25, 10 (1913); *Phil. Mag.* 30, 581 (1915)
11. B. Rossi and K. Greisen, *Revs. Modern Phys.* 13, 240 (1941)
12. E.J. Williams, *Proc. Roy. Soc. (London)* 125, 420 (1929); 130, 310 (1931); 130, 328 (1931)
13. H. Bethe, *Ann. Physik* 5, 325 (1930); *Z. Physik* 76, 293 (1932)
14. B. Rossi, "High-Energy Particles," Chap. 2, Prentice-Hall, New York, 1952
15. L. Landau, *J. Phys. (U.S.S.R.)* 8, 201 (1944)
16. K.R. Symon, "Fluctuations in Energy Lost by High Energy Charged Particles in Passing Through Matter," Ph.D. Thesis, Harvard University, 1948. Symon's thesis is discussed briefly by B. Rossi, Ref. 14.
17. J.M. Kennedy and B.J. Jones, private communication to H.E. Gove, Ref. 2
18. W. Börsch-Supan, *J. Research Natl. Bur. Standards* 65B, 245 (1961)
19. H. Bichsel and E.A. Uehling, *Phys. Rev.* 119, 1670 (1960)
20. K.J. Broström, T. Huus, and R. Tangen, *Phys. Rev.* 71, 661 (1947)

21. S.K. Allison and S.D. Warshaw, *Revs. Modern Phys.* 25, 779 (1953)
22. R.O. Bondelid, J.W. Butler, C.A. Kennedy, and A. del Callar, *Phys. Rev.* 120, 887 (1960)
23. E. Teller, *Z. Physik* 61, 458 (1930)
24. D.R. Bates, K. Ledsham, and A.L. Stewart, *Phil. Trans. Roy. Soc., London* 246A, 215 (1953)
25. S. Cohen, J.R. Hiskes, and R.J. Riddell, Jr., *Phys. Rev.* 119, 1025 (1960)
26. E.E. Salpeter, *Proc. Phys. Soc. (London)* 63A, 1295 (1950)
27. R.G. Alsmiller, Jr., Oak Ridge National Laboratory Document 2766, Oct. 23, 1959
28. E.H. Kerner, *Phys. Rev.* 92, 1441 (1953)
29. U. Hauser and W. Kerler, *Rev. Sci. Instr.* 29, 380 (1958)
30. S.L. Andersen, K. Gjötterud, T. Holtebekk, and O. Lönsjö, *Nuclear Phys.* 7, 384 (1958)
31. P.F. Dahl, D.G. Costello, and W.L. Walters, *Bull. Am. Phys. Soc.* 5, 406 (1960)
32. P.F. Dahl; D.G. Costello, and W.L. Walters, *Nuclear Phys.* 21, 106 (1960)
33. D.G. Costello, W.L. Walters, and R.G. Herb, *Bull. Am. Phys. Soc.* 6, 250 (1961)
34. W.L. Walters, D.G. Costello, J.G. Skofronick, D.W. Palmer, W.E. Kane, and R.G. Herb, *Phys. Rev. Letters* 7, 284 (1961)
35. H.W. Lewis, *Phys. Rev.* 125, 937 (1962)
36. D.G. Costello, W.L. Walters, J.G. Skofronick, D.W. Palmer, W.E. Kane, and R.G. Herb, *Bull. Am. Phys. Soc.* 6, 430 (1961)
37. W.L. Walters, D.G. Costello, J.G. Skofronick, D.W. Palmer, W.E. Kane, and R.G. Herb, *Bull. Am. Phys. Soc.* 6, 431 (1961)
38. W.L. Walters, D.G. Costello, J.G. Skofronick, D.W. Palmer, W.E. Kane, and R.G. Herb, *Phys. Rev.* 125, 2012 (1962)
39. D.W. Palmer, J.G. Skofronick, D.G. Costello, W.E. Kane, and R.G. Herb, *Bull. Am. Phys. Soc.* 7, 301 (1962)
40. J.G. Skofronick, D.W. Palmer, D.G. Costello, A.L. Morsell, W.E. Kane, and R.G. Herb, *Bull. Am. Phys. Soc.* 7, 301 (1962)
41. D.G. Costello, W.E. Kane, A.L. Morsell, D.W. Palmer, J.G. Skofronick, and R.G. Herb, *Bull. Am. Phys. Soc.* 7, 301 (1962)
42. R.O. Bondelid and E.E. Dowling (to be published)
43. S.L. Andersen, T. Holtebekk, C. Lönsjö, and R. Tangen, *Nuclear Phys.* 4, 39 (1957)

\* \* \*

## UNCLASSIFIED

Naval Research Laboratory. Report 5897.  
AN INVESTIGATION OF THE PHENOMENOLOGICAL  
CHARACTERISTICS OF (p,  $\gamma$ ) RESONANCES BY  
R. O. Bondelid and J. W. Butler. 59 pp. & figs.,  
May 7, 1963.

The observation of some "anomalies" in the behavior of gamma-ray resonances induced by hydrogen molecular ion beams has led to an exhaustive investigation of these and other new anomalies, including some involving proton beams. Most of the observations have been made with respect to the 992-keV resonance in the  $Al^{27}(p, \gamma)Si^{28}$  reaction, but the following have also been used: the 1317-keV resonance in the same reaction, the 1747-keV resonance in the  $C^{13}(p, \gamma)N^{14}$  reaction, the 1424-keV resonance in the  $Ni^{58}(p, \gamma)Cu^{59}$  reaction, and the 1843-keV resonance in the same reaction. The anomalies for  $H^+$  beams are all satisfactorily explained on the basis of fluctuations in energy loss of the bombarding protons as they penetrate the target. Detailed

(Over)

- I. Gamma rays - Resonance
- II. Hydrogen bombardment

- I. Bondelid, R. O.
- II. Butler, J. W.

## UNCLASSIFIED

Naval Research Laboratory. Report 5897.  
AN INVESTIGATION OF THE PHENOMENOLOGICAL  
CHARACTERISTICS OF (p,  $\gamma$ ) RESONANCES BY  
R. O. Bondelid and J. W. Butler. 59 pp. & figs.,  
May 7, 1963.

The observation of some "anomalies" in the behavior of gamma-ray resonances induced by hydrogen molecular ion beams has led to an exhaustive investigation of these and other new anomalies, including some involving proton beams. Most of the observations have been made with respect to the 992-keV resonance in the  $Al^{27}(p, \gamma)Si^{28}$  reaction, but the following have also been used: the 1317-keV resonance in the same reaction, the 1747-keV resonance in the  $C^{13}(p, \gamma)N^{14}$  reaction, the 1424-keV resonance in the  $Ni^{58}(p, \gamma)Cu^{59}$  reaction, and the 1843-keV resonance in the same reaction. The anomalies for  $H^+$  beams are all satisfactorily explained on the basis of fluctuations in energy loss of the bombarding protons as they penetrate the target. Detailed

(Over)

- I. Gamma rays - Resonance
- II. Hydrogen bombardment

- I. Bondelid, R. O.
- II. Butler, J. W.

## UNCLASSIFIED

Naval Research Laboratory. Report 5897.  
AN INVESTIGATION OF THE PHENOMENOLOGICAL  
CHARACTERISTICS OF (p,  $\gamma$ ) RESONANCES BY  
R. O. Bondelid and J. W. Butler. 59 pp. & figs.,  
May 7, 1963.

The observation of some "anomalies" in the behavior of gamma-ray resonances induced by hydrogen molecular ion beams has led to an exhaustive investigation of these and other new anomalies, including some involving proton beams. Most of the observations have been made with respect to the 992-keV resonance in the  $Al^{27}(p, \gamma)Si^{28}$  reaction, but the following have also been used: the 1317-keV resonance in the same reaction, the 1747-keV resonance in the  $C^{13}(p, \gamma)N^{14}$  reaction, the 1424-keV resonance in the  $Ni^{58}(p, \gamma)Cu^{59}$  reaction, and the 1843-keV resonance in the same reaction. The anomalies for  $H^+$  beams are all satisfactorily explained on the basis of fluctuations in energy loss of the bombarding protons as they penetrate the target. Detailed

(Over)

- I. Gamma rays - Resonance
- II. Hydrogen bombardment

- I. Bondelid, R. O.
- II. Butler, J. W.

## UNCLASSIFIED

Naval Research Laboratory. Report 5897.  
AN INVESTIGATION OF THE PHENOMENOLOGICAL  
CHARACTERISTICS OF (p,  $\gamma$ ) RESONANCES BY  
R. O. Bondelid and J. W. Butler. 59 pp. & figs.,  
May 7, 1963.

The observation of some "anomalies" in the behavior of gamma-ray resonances induced by hydrogen molecular ion beams has led to an exhaustive investigation of these and other new anomalies, including some involving proton beams. Most of the observations have been made with respect to the 992-keV resonance in the  $Al^{27}(p, \gamma)Si^{28}$  reaction, but the following have also been used: the 1317-keV resonance in the same reaction, the 1747-keV resonance in the  $C^{13}(p, \gamma)N^{14}$  reaction, the 1424-keV resonance in the  $Ni^{58}(p, \gamma)Cu^{59}$  reaction, and the 1843-keV resonance in the same reaction. The anomalies for  $H^+$  beams are all satisfactorily explained on the basis of fluctuations in energy loss of the bombarding protons as they penetrate the target. Detailed

(Over)

- I. Gamma rays - Resonance
- II. Hydrogen bombardment

- I. Bondelid, R. O.
- II. Butler, J. W.

## UNCLASSIFIED

numerical integrations of the formal yield equation have been made, and in most cases very good fits have been made with the experimental data. The energy-loss theory used to compute the energy-loss fluctuations has been mainly the theory developed by Symon. For the anomalies observed with the use of  $H_1^+$  beams, the theory is more complicated because of the larger number of parameters involved. Precise best values are given for the following narrow  $(p, \gamma)$  resonances:  $Al^{27}(p, \gamma)Si^{28}$  reaction,  $991.91 \pm 0.30$  and  $1317.19 \pm 0.40$  keV;  $C^{13}(p, \gamma)N^{14}$  reaction,  $1747.06 \pm 0.53$  keV  $Ni^{58}(p, \gamma)Cu^{59}$  reaction,  $1423.64 \pm 0.43$  and  $1843.45 \pm 0.56$  keV. The displacement of the midpoint of the rise of a thick-target  $H_1^+$  yield curve from the resonance energy  $E_r$  as a function of the resonance width  $\Gamma$  is discussed, and a typical curve of this relationship is shown. The overshoot or hump height for thick targets with  $H_1^+$  beams as a function of  $\Gamma$  is also discussed, and a curve is shown. Methods for making extremely uniform and clean thin targets have been developed and are discussed. A number of new questions were suggested by the results of these experiments, and experiments to answer these new questions are proposed to the reader for his consideration.

## UNCLASSIFIED

## UNCLASSIFIED

numerical integrations of the formal yield equation have been made, and in most cases very good fits have been made with the experimental data. The energy-loss theory used to compute the energy-loss fluctuations has been mainly the theory developed by Symon. For the anomalies observed with the use of  $H_1^+$  beams, the theory is more complicated because of the larger number of parameters involved. Precise best values are given for the following narrow  $(p, \gamma)$  resonances:  $Al^{27}(p, \gamma)Si^{28}$  reaction,  $991.91 \pm 0.30$  and  $1317.19 \pm 0.40$  keV;  $C^{13}(p, \gamma)N^{14}$  reaction,  $1747.06 \pm 0.53$  keV  $Ni^{58}(p, \gamma)Cu^{59}$  reaction,  $1423.64 \pm 0.43$  and  $1843.45 \pm 0.56$  keV. The displacement of the midpoint of the rise of a thick-target  $H_1^+$  yield curve from the resonance energy  $E_r$  as a function of the resonance width  $\Gamma$  is discussed, and a typical curve of this relationship is shown. The overshoot or hump height for thick targets with  $H_1^+$  beams as a function of  $\Gamma$  is also discussed, and a curve is shown. Methods for making extremely uniform and clean thin targets have been developed and are discussed. A number of new questions were suggested by the results of these experiments, and experiments to answer these new questions are proposed to the reader for his consideration.

## UNCLASSIFIED

## UNCLASSIFIED

numerical integrations of the formal yield equation have been made, and in most cases very good fits have been made with the experimental data. The energy-loss theory used to compute the energy-loss fluctuations has been mainly the theory developed by Symon. For the anomalies observed with the use of  $H_1^+$  beams, the theory is more complicated because of the larger number of parameters involved. Precise best values are given for the following narrow  $(p, \gamma)$  resonances:  $Al^{27}(p, \gamma)Si^{28}$  reaction,  $991.91 \pm 0.30$  and  $1317.19 \pm 0.40$  keV;  $C^{13}(p, \gamma)N^{14}$  reaction,  $1747.06 \pm 0.53$  keV  $Ni^{58}(p, \gamma)Cu^{59}$  reaction,  $1423.64 \pm 0.43$  and  $1843.45 \pm 0.56$  keV. The displacement of the midpoint of the rise of a thick-target  $H_1^+$  yield curve from the resonance energy  $E_r$  as a function of the resonance width  $\Gamma$  is discussed, and a typical curve of this relationship is shown. The overshoot or hump height for thick targets with  $H_1^+$  beams as a function of  $\Gamma$  is also discussed, and a curve is shown. Methods for making extremely uniform and clean thin targets have been developed and are discussed. A number of new questions were suggested by the results of these experiments, and experiments to answer these new questions are proposed to the reader for his consideration.

## UNCLASSIFIED

## UNCLASSIFIED

numerical integrations of the formal yield equation have been made, and in most cases very good fits have been made with the experimental data. The energy-loss theory used to compute the energy-loss fluctuations has been mainly the theory developed by Symon. For the anomalies observed with the use of  $H_1^+$  beams, the theory is more complicated because of the larger number of parameters involved. Precise best values are given for the following narrow  $(p, \gamma)$  resonances:  $Al^{27}(p, \gamma)Si^{28}$  reaction,  $991.91 \pm 0.30$  and  $1317.19 \pm 0.40$  keV;  $C^{13}(p, \gamma)N^{14}$  reaction,  $1747.06 \pm 0.53$  keV  $Ni^{58}(p, \gamma)Cu^{59}$  reaction,  $1423.64 \pm 0.43$  and  $1843.45 \pm 0.56$  keV. The displacement of the midpoint of the rise of a thick-target  $H_1^+$  yield curve from the resonance energy  $E_r$  as a function of the resonance width  $\Gamma$  is discussed, and a typical curve of this relationship is shown. The overshoot or hump height for thick targets with  $H_1^+$  beams as a function of  $\Gamma$  is also discussed, and a curve is shown. Methods for making extremely uniform and clean thin targets have been developed and are discussed. A number of new questions were suggested by the results of these experiments, and experiments to answer these new questions are proposed to the reader for his consideration.

## UNCLASSIFIED